Growth, structure and lattice dynamics of iron silicide nanostructures

Zur Erlangung des akademischen Grades eines
DOKTORS DER NATURWISSENSCHAFTEN (Dr. rer. nat.)

von der KIT-Fakultät für Physik des
Karlsruher Instituts für Technologie (KIT)
angenommene

DISSERTATION

von

M. Sc. Jochen Kalt

Tag der Mündlichen Prüfung: 05.02.2021

Referent:	Prof. Dr. Tilo Baumbach
Korreferent:	Prof. Dr. Matthieu Le Tacon
Zusätzlicher Referent:	Dr. Svetoslav Stankov

Abstract

In the present thesis, the lattice dynamics of nanostructures of the iron-silicide compounds Fe_3Si, α-$FeSi_2$, and β-$FeSi_2$ is investigated. A comprehensive understanding of the effect of spatial confinement to the nanometer scale on the lattice dynamics is a prerequisite for the application of these materials as nanoscale device components, as well as for the envisaged specific manipulation of the vibrational properties of nanostructures.

Single-crystalline nanostructures of the investigated materials are grown via molecular-beam epitaxy and their structural properties are comprehensively characterized with complementary methods. The Fe-partial phonon density of states (PDOS) of the nanostructures is obtained by nuclear inelastic scattering, a technique uniquely suitable for the measurement of the inherently small scattering volume available in nanostructures. Knowledge of the PDOS enables the determination of fundamental thermodynamic and elastic properties, inter alia the mean force constant, the mean square displacement, the lattice heat capacity, and the velocity of sound. The comparison of the experimental results with *ab initio* calculations allows to establish a correlation between the structural properties of the nanostructures and the observed deviations of their lattice dynamics from the corresponding bulk crystals.

With this approach, the lattice dynamics of the Fe_3Si/GaAs heterostructure, α-$FeSi_2$ nanoislands and nanowires, and β-$FeSi_2$ nanorods is investigated. Two general trends are identified. First, the increase of the interface/surface-to-volume ratio results in a significant impact of interface- and surface-specific vibrational modes on the overall PDOS. Second, the crystalline disorder present at interfaces and surfaces leads to an enhanced defect scattering of phonons and a broadening of the PDOS features. As a result, the thermodynamic and elastic properties show a softening of the lattice as the crystal size is reduced, which is evidenced by an increased mean square displacement and a reduced velocity of sound.

Furthermore, the study of the Fe_3Si/GaAs heterostructure reveals the emergence of an interface-specific vibrational density of states at epitaxial, strain-free interfaces. In α-$FeSi_2$ nanostructures an anomalously strong damping of acoustic phonons is observed upon reduction of the crystal size below 10 nm. Nanowires of the same compound exhibit an anisotropic damping of lattice vibrations along and across the nanowires. The investigation of β-$FeSi_2$ nanorods reveals the emergence of a new vibrational mode at low energies, which is attributed to the formation of an interstitial Fe-rich layer.

Zusammenfassung

In der vorliegenden Arbeit wird die Gitterdynamik von Nanostrukturen der Eisen-Silizium-Verbindungen Fe_3Si, α-$FeSi_2$, und β-$FeSi_2$ untersucht. Ein umfassendes Verständnis des Einflusses einer räumlichen Beschränkung auf die Nanometerskala auf die Gitterdynamik ist Voraussetzung für die Nutzung dieser Materialien in nanoskaligen elektronischen Bauteilen sowie für die angestrebte gezielte Manipulation der Schwingungseigenschaften von Nanostrukturen.

Monokristalline Nanostrukturen der untersuchten Materialien werden mittels Molekularstrahlepitaxie hergestellt und mit komplementären Methoden umfassend auf ihre strukturellen Eigenschaften charakterisiert. Die partielle Fe Phononenzustandsdichte (PDOS) der Nanostrukturen wird mittels unelastischer Kernstreuung erhalten, einer Technik, die in einzigartiger Weise für die Messung des inhärent kleinen Streuvolumens von Nanostrukturen geeignet ist. Die Kenntnis der PDOS ermöglicht die Bestimmung fundamentaler thermodynamischer und elastischer Eigenschaften, unter anderem der mittleren Kraftkonstante, der mittleren quadratischen Auslenkung, der Wärmekapazität des Gitters und der Schallgeschwindigkeit. Der Vergleich der experimentellen Ergebnisse mit *ab initio* Berechnungen erlaubt es eine Korrelation zwischen den strukturellen Eigenschaften der Nanostrukturen und den beobachteten Abweichungen ihrer Gitterdynamik von den dazugehörigen Volumenkristallen herzustellen.

Mit diesem Ansatz werden die Gitterdynamik der Fe_3Si/GaAs Heterostruktur, von α-$FeSi_2$ Nanoinseln und Nanodrähten sowie von β-$FeSi_2$ Nanostäben untersucht. Dabei werden zwei allgemeine Phänomene identifiziert: Erstens resultiert die Erhöhung des Grenzflächen-/Oberflächen-zu-Volumen-Verhältnisses in einem signifikanten Einfluss von Grenzflächen- und Oberflächen-spezifischen Schwingungsmoden auf die gesamte PDOS. Zweitens führt die kristalline Unordnung an Grenzflächen und Oberflächen zu einer verstärkten Streuung von Phononen an Defekten und einer Dämpfung der PDOS. Als Resultat zeigen die thermodynamischen und elastischen Eigenschaften eine "Aufweichung" des Gitters als Funktion der Kristallgröße, was durch eine erhöhte mittlere quadratischen Auslenkung und eine reduzierte Schallgeschwindigkeit belegt wird.

Darüber hinaus offenbart die Untersuchung der Fe_3Si/GaAs Heterostruktur das Auftreten von Grenzflächen-spezifischen Schwingungsmoden an epitaktischen, verspannungsfreien Grenzflächen. In α-$FeSi_2$ Nanostrukturen wird nach der Reduktion der charakteristischen Kristallgröße unter 10 nm eine anormal starke Dämpfung akustischer Phononen beobachtet. Nanodrähte desselben Materials weisen eine anisotrope Dämpfung von Gitterschwingungen entlang und quer zu den Nanodrähten auf. Die Untersuchung von β-$FeSi_2$ Nanostäben offenbart das Auftreten einer neuen Schwingungsmode bei niedrigen Energien, die der Bildung einer Fe-reichen Zwischenlage zugeschrieben wird.

Contents

1. Introduction **1**

2. Theoretical background and experimental techniques **5**
2.1. Lattice dynamics 5
2.1.1. Phonon dispersion relations and density of states 6
2.1.2. Thermodynamic and elastic properties 8
2.1.3. Damped harmonic oscillator function 9
2.2. Experimental methods 10
2.2.1. Molecular-beam epitaxy 10
2.2.2. Structural characterization methods 12
2.2.3. Nuclear resonant scattering 16
2.2.4. *Ab initio* lattice dynamics 24

3. Properties of iron silicides **27**
3.1. Structural properties of iron silicides 27
3.2. Growth of iron silicide nanostructures 29
3.3. *Ab initio* lattice dynamics calculations of Fe_3Si, β-$FeSi_2$ and α-$FeSi_2$. 31

4. Lattice dynamics of the epitaxial, strain-free Fe_3Si/GaAs heterostructure **35**
4.1. Sample preparation and characterization 35
4.2. Lattice dynamics 42
4.3. Thermodynamic and elastic properties 47
4.4. Conclusions 49

5. Lattice dynamics of metastable α-phase $FeSi_2$ nanostructures **51**
5.1. Sample preparation and characterization 51
5.2. Lattice dynamics 60
5.3. Thermodynamic and elastic properties 66
5.4. Conclusions 68

6. Lattice dynamics of α-phase $FeSi_2$ nanowires **71**
6.1. Sample preparation and characterization 72
6.2. Lattice dynamics 80
6.3. Thermodynamic and elastic properties 85
6.4. Conclusions 86

7. Lattice dynamics of β-phase $FeSi_2$ nanorods **89**
7.1. Sample preparation and characterization 89
7.2. Lattice dynamics 96

7.3. Thermodynamic and elastic properties 99
7.4. Conclusions 99

8. Summary and conclusions **101**

Bibliography **103**

List of Figures **115**

List of Tables **117**

A. Publications **119**
A.1. Publications related to the thesis 119
A.2. Other publications 119
A.3. Conference contributions 120

B. Python script **121**

Acknowledgement **125**

1. Introduction

The collective vibrations of atoms bound in a crystal give rise to waves propagating through the solid. The energy quantum of such a wave is associated with an elementary excitation called *phonon*. The name originates from the Greek word for sound, since long-wavelength phonons are responsible for its propagation through a solid. These collective atomic vibrations are fully described by the material-specific *phonon dispersion relations* and *phonon density of states*, which determine the fundamental thermodynamic and elastic properties of a crystal. Furthermore, phonons couple to other particles and quasi-particles, such as electrons, magnons, and other phonons. Via these interactions, phonons are of central importance for basic characteristics of crystals, e.g. thermal conductivity in semiconductors and insulators, optical properties, electric conductivity at room temperature, and play a crucial role in physical phenomena like phase transitions, superconductivity, and thermoelectricity.

Reduction of the crystal dimensions to the nanometer scale and the correlated increase of the interface/surface-to-volume ratio lead to pronounced changes in the vibrational properties [1]. The phonon mean free path at room temperature spans from tens of nanometers to several micrometers. A confinement of the crystal size to this range results in an enhanced boundary scattering of phonons. As a consequence, the propagation of long-wavelength phonons, which are the main heat carriers in semiconductors and insulators, is significantly impeded. In combination with an additionally enhanced electron-phonon scattering, the reduced thermal conductivity leads to a self-heating of electronic devices. This constitutes a fundamental obstacle for the further miniaturization of device components and for the increase of the clock rate [2–4]. On the other hand, the manipulation of the thermal conductivity by nanoscaling is a promising ansatz for increasing the efficiency of thermoelectric devices, since it offers the possibility to impede the propagation of heat, while the electric conductivity remains unaffected [5–7]. A further reduction of the crystal size to the wavelength of acoustic phonons, which is in the range of a few nanometers and below, results in considerable modifications of the phonon dispersion relations. This can lead to the emergence of phononic band gaps [8, 9], and consequently a discretization of the phonon density of states [10, 11]. These quantum effects modify the coupling strength of phonons to other excitations, with substantial consequences e.g. for optoelectronics, superconductivity, magnetoresistance, and catalysis [12–18]. Once being comprehensively understood, the anomalous phonon behavior can be used to tailor the vibrational properties of nanostructures, an approach referred to as *phonon engineering* [19, 20], with the ultimate goal of designing a novel type of devices that operate with lattice excitations as carriers of information [9, 21–26]. The ability to control the propagation of phonons to the extent possible today for electrons and photons has the potential to spark the next technological revolution.

These promising perspectives demand for a comprehensive investigation of the lattice dynamics of nanoscale crystals. However, the determination of the phonon dispersion relations or phonon density of states in such systems remains a grand challenge in modern solid-state physics. Inelastic neutron and x-ray scattering, which are commonly applied for the determination of the phonon dispersion relations in bulk and micrometer-sized crystals, do not provide the required sensitivity for the measurement of the inherently small scattering volume of nanostructures. Helium atom scattering and electron energy-loss spectroscopy exhibit an extremely low penetration depth and are only applicable for the investigation of the phonon dispersions of surfaces. Methods based on the inelastic scattering of visible light, such as Brillouin and Raman scattering, are restricted to small momentum transfers and low-energy phonon modes, which constitute a minor fraction of the vibrational spectrum. *Nuclear inelastic scattering* [27, 28], on the other hand, has proven to be uniquely suitable for the determination of the lattice dynamics of nanostructures. The technique is based on the Mössbauer effect, whose resonant nature implies a large absorption cross section and provides an outstanding sensitivity to submonolayers of material [29]. It offers direct access to the partial phonon density of states of Mössbauer-active isotopes and allows for the determination of the fundamental thermodynamic and elastic properties of solids [30]. The high penetration depth of the x rays enables the measurement of bulk materials and, in conjunction with the element and isotope selectivity of the Mössbauer effect, ultra-thin buried layers [31].

Transition-metal silicides constitute fundamental building blocks of current microelectronics and are promising candidates for applications in future nanoscale electronic devices [32–35]. Iron-silicide is a particularly interesting member of this class of materials, since it is the only transition-metal silicide that forms both metallic and semiconducting phases [36]. The Fe-Si phase diagram exhibits a broad variety of stable and metastable compounds, with Fe_3Si and $FeSi_2$ being the technologically most relevant. The iron-rich metal Fe_3Si has been proposed for applications in high-density magnetic storage [37] and is a well established model system for the study of metal/semiconductor heterostructures for spintronic applications [38–40]. $FeSi_2$ can be synthesized in metallic and semiconducting phases in thin films and self-assembled nanostructures, and its utilization has been proposed inter alia for optoelectronics [41], fiber-optic communication [42, 43], photovoltaics [44, 45], thermoelectrics [35, 46, 47], and nanoelectronics [48]. The variety of foreseen applications, in conjunction with the phonon confinement effects discussed above, calls for a comprehensive study of the vibrational properties of nanoscale Fe-Si compounds. The Mössbauer active isotope ^{57}Fe offers the possibility to systematically investigate phonon confinement effects by nuclear inelastic scattering in different types of nanostructures, which is a prerequisite for further progress in the emerging field of phonon engineering.

The aim of this thesis is the comprehensive investigation of the lattice dynamics of iron-silicide nanostructures, with focus on Fe_3Si, α-$FeSi_2$, and β-$FeSi_2$. For this purpose, single-crystalline nanostructures are prepared via molecular-beam epitaxy. The correlation between the structural properties and the lattice dynamics of the nanostructures demands for an extensive structural characterization with several complementary methods. The Fe-partial phonon density of states of the nanos-

tructures is determined by nuclear inelastic scattering experiments. A thorough understanding of the experimental results is achieved by comparison and modeling with first-principles calculations, which are performed by a collaboration partner.

The thesis is structured as follows: Chapter 2 gives an introduction to the underlying theoretical concepts and the applied experimental methods. Chapter 3 is devoted to the properties of the investigated iron-silicide compounds and the results of the first-principles calculations. The investigation of the lattice dynamics of the Fe_3Si/GaAs heterostructure is presented in Chapter 4. The lattice dynamics of metastable α-$FeSi_2$ nanostructures are discussed in Chapter 5, Chapter 6 deals with the results obtained for α-$FeSi_2$ nanowires. In Chapter 7 the results obtained for bulk-like films and nanorods of β-$FeSi_2$ are given. Chapter 4 to 7 start with a detailed description of the sample preparation and characterization. Subsequently, the experimental results on the lattice dynamics are compared with first-principles calculations and the effects of the spatial confinement are discussed. Furthermore, the thermodynamic and elastic properties are presented. In Chapter 8 the results obtained in the preceding chapters are summarized and concluded.

2. Theoretical background and experimental techniques

The purpose of this chapter is to introduce the basic concepts of lattice dynamics and to provide an overview of the applied experimental methods. The chapter starts with the introduction of the phonon dispersion relations and the phonon density of states. The calculation of basic thermodynamic and elastic properties from the vibrational spectrum is presented and the damped harmonic oscillator function is discussed. Subsequently, the experimental methods used for the preparation and the structural characterization of the investigated samples are described. A brief introduction to the basic principles of the Mössbauer effect is given, followed by a detailed discussion of the nuclear inelastic scattering of x rays. The chapter concludes with a brief introduction to the *ab initio* method.

2.1. Lattice dynamics

The vibrational properties of atoms bound in a lattice are one of the fundamental topics in solid state physics. The lattice dynamics determine basic characteristics of a solid, such as the propagation of heat and sound, the thermodynamic and elastic properties, and play a crucial role in phase transitions. Via coupling of lattice excitations with other particles, such as electrons, plasmons and magnons, the lattice dynamics has a substantial influence on the overall physical properties of materials. Lattice dynamics is a many body problem describing the motion of bound atoms around their equilibrium positions. The Schrödinger equation of such a system is decisively simplified by the adiabatic approximation, i.e. by the assumption that the 10^3 fold heavier nuclei are at rest in the electronic reference system. The equation of motion of the nuclei is obtained under harmonic approximation of the effective interatomic potential the atoms are localized in. These approximations are known as the Born-von Karman boundary conditions. The result for the N atoms contained in the system is decoupled by transformation of the Cartesian coordinates into *normal modes*, treating the many body problem with $3N$ decoupled equations of motion. A normal mode describes the collective vibration of atoms. In the harmonic approximation a normal mode does not transfer energy to other modes and exhibits an infinite lifetime. A detailed mathematical description of this brief overview can be found in the comprehensive literature on lattice dynamics (e.g. [49–51]).

2.1.1. Phonon dispersion relations and density of states

In the description of the lattice dynamics by normal modes, the collective vibrations are treated as independent harmonic oscillators, having a quantized energy of:

$$E = \hbar\omega\left(n + \frac{1}{2}\right), \text{ with } n = 0, 1, 2, ... \tag{2.1}$$

where $\hbar$ is the reduced Planck constant and ω denotes the frequency of the vibration. The lattice excitations can have wavelengths that largely exceed the interatomic distances and are described by non-localized quasi-particles named phonons. Since phonons describe the relative motion of the atoms, rather than the motion of their center of mass, they have a *quasi*-momentum equal to $\hbar\mathbf{k}$, with $\mathbf{k}$ being the phonon wave vector. An increase of temperature T also increases the amplitude of the lattice vibrations and the number of phonons. Since phonons are bosons, the average phonon number $\langle n(\mathbf{k}_j)\rangle$ in a mode j at thermal equilibrium is given by the Bose-Einstein statistics:

$$\langle n(\mathbf{k}_j)\rangle = \frac{1}{exp\,(\hbar\omega_j\beta) - 1}, \tag{2.2}$$

where $\beta = 1/k_BT$, with k_B the Boltzmann constant. The average phonon energy for a mode $\mathbf{k}_j$ at temperature T is given by:

$$\langle E(\omega_j(\mathbf{k}), T)\rangle = \hbar\omega_j(\mathbf{k})\left(\langle n(\mathbf{k}_j)\rangle + \frac{1}{2}\right). \tag{2.3}$$

The total energy can be calculated by summation over all vibrational modes:

$$\langle E(T)\rangle = \sum_{\mathbf{k},j}\langle E(\omega_j(\mathbf{k}), T) = \sum_{\mathbf{k},j}\hbar\omega_j(\mathbf{k})\langle n(\mathbf{k}_j)\rangle + \frac{1}{2}\sum_{\mathbf{k},j}\hbar\omega_j(\mathbf{k}). \tag{2.4}$$

The second term is temperature independent and describes the ground state energy at $T = 0\,K$.

The relationship between the phonon frequency ω and the wave vector $\mathbf{k}$ is described by the phonon dispersion relations (PDR). In Figure 2.1(a) the PDR of silicon is shown along the high symmetry directions Γ-X ([100]), Γ-K ([110]) and Γ-L ([111]) in the first Brillouin zone of the fcc lattice. For unit cells containing $s \geq 2$ atoms, the phonon band structure consists of 3 acoustic and $3s - 3$ optical branches. The acoustic branches describe the motion of the unit cell, whereas the optical branches describe the relative motion of the atoms contained in the unit cell. Consequently, only acoustic branches exist for a unit cell with $s = 1$. The respective phonon branches can be divided into transverse modes, where the particle displacement is perpendicular to the direction of wave propagation, and longitudinal modes, where the particle displacement is parallel to the direction of wave propagation. As observed in Figure 2.1(a), the PDR of fcc lattices exhibits transverse modes that are degenerated along Γ-X and Γ-L, while along Γ-K all branches can be identified separately [49]. The group velocity of a phonon mode can be calculated as $v_G = \partial\omega_j(k)/\partial k$. Acoustic phonons exhibit an approximately linear dispersion, which is described by $v_S = \omega_j(k)/k$, where v_S is the velocity of sound.

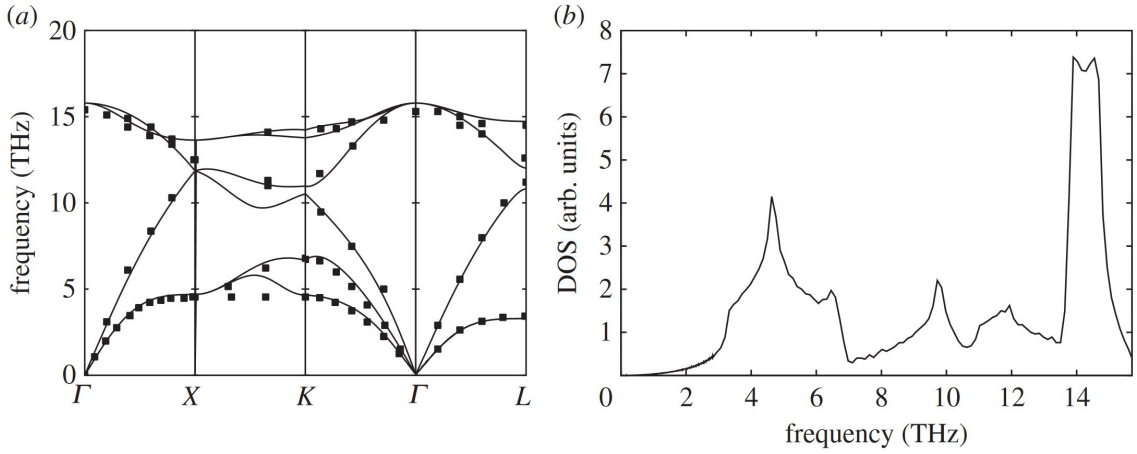

Figure 2.1: (a) Phonon dispersion relations of silicon. The solid lines denote theoretical results, the symbols represent data from neutron scattering experiments. (b) Corresponding phonon density of states. Adapted from [52].

The temperature-dependent component of Equation (2.4) can be rewritten as:

$$\langle E(T)\rangle = 3N \int_0^{\omega_m} \frac{\hbar\omega}{exp\,(\hbar\omega\beta) - 1} g(\omega) d\omega, \tag{2.5}$$

where ω_m denotes the maximum frequency and $g(\omega)$ is the normalized frequency distribution, also referred to as the phonon density of states (PDOS). The PDOS describes the frequency distribution of the normal modes and gives a measure for the probability of lattice waves in the frequency interval $\omega + d\omega$. When the dispersion relations are known for all $\mathbf{k}$ values in the first Brillouin zone, the PDOS can be calculated as:

$$g(\omega) = \frac{1}{3N} \sum_{j}^{3} \sum_{\mathbf{k}}^{N} \delta(\omega - \omega_j(\mathbf{k})). \tag{2.6}$$

In Figure 2.1(b) the PDOS of silicon, calculated from the corresponding dispersion relations in Figure 2.1(a), is displayed. The summation over $\mathbf{k}$ in regions where $\partial\omega(\mathbf{k})/\partial\omega \to 0$ leads to maxima in the PDOS, referred to as van-Howe singularities. If the unit cell of a material contains different types of atoms, or non-equal atomic sites, the total PDOS is the sum over all the respective partial PDOS $g_d(\omega)$ [53]:

$$g(\omega) = \sum_d g_d(\omega). \tag{2.7}$$

This is especially important in the context of nuclear inelastic scattering, from which solely the isotope-specific partial PDOS of the Mössbauer-active nuclei is obtained. The relative weight of each partial PDOS is given by the atomic fraction per unit cell.

Furthermore, the PDOS can be approximated by the simplified models proposed by Einstein [54] and Debye [55], which aimed at a theoretical prediction of the lattice heat capacity . While Einstein's postulation of atoms independently vibrating with one single frequency could only qualitatively describe the lattice heat capacity as a function of temperature, Debye's assumption of an isotropic continuum leads to a

good agreement between theory and experiment in the low-energy region of the vibrational spectrum. The continuum model uses the long-wavelength approximation and is therefore restricted to the description of acoustic phonon branches. Following the Debye model, the PDOS can be described up to a cut-off frequency ω_D (Debye frequency) by the dependence $g(\omega) = \alpha\, E^n$, where $n = 2$ for a three dimensional system and $n = 1$ in two dimensions.

2.1.2. Thermodynamic and elastic properties

In statistical physics, the partition function is a vital tool for the deduction of the macroscopic thermodynamic quantities of a system from its microscopic properties. It defines the occupation probability of an energetic state available in the system. The partition function of a single harmonic oscillator with frequency $\omega_i = E_i/\hbar$ is given by [53]:

$$Z_i = \sum_n^{\infty} e^{-\beta(n+1/2)E_i} = \frac{e^{-\beta E_i/2}}{1 - e^{-\beta E_i}}. \tag{2.8}$$

The partition function of a lattice consisting of N atoms and $3N$ independent harmonic oscillators is the product of the partition functions of the individual oscillators:

$$Z_N = \prod_i^{3N} \frac{e^{-\beta E_i/2}}{1 - e^{-\beta E_i}}. \tag{2.9}$$

In case of a three-dimensional lattice, $3Ng(E)dE$ phonon modes are available in an energy interval dE and the partition function can be written as:

$$ln(Z_N) = -3N \int_0^{\infty} ln\left(\frac{e^{\beta E} - 1}{e^{\beta E/2}}\right) g(E)dE \tag{2.10}$$

The knowledge of the PDOS $g(E)$ gives access to several important thermodynamic properties of the atomic lattice [30]. The contribution of lattice vibrations to the internal energy per atom is given by:

$$U = -\frac{\partial ln(Z_N)}{\partial \beta} = \frac{3}{2}\int_0^{\infty} g(E)E\frac{e^{\beta E} + 1}{e^{\beta E} - 1}dE. \tag{2.11}$$

Neglecting the temperature dependence of the PDOS, the lattice heat capacity per atom at constant volume can be calculated by:

$$C_V = \frac{dU}{dT} = \left(\frac{\partial U}{\partial T}\right)_V = \int_0^{\infty} g(E)\frac{(\beta E)^2 e^{\beta E}}{(e^{\beta E} - 1)^2}dE. \tag{2.12}$$

The vibrational entropy per atom can be determined by:

$$S_V = 3k_B \int_0^{\infty} g(E)\left(\frac{\beta E}{2}\frac{e^{\beta E} + 1}{e^{\beta E} - 1} - \ln(e^{\beta E/2} - e^{-\beta E/2})\right)dE. \tag{2.13}$$

Furthermore, the mean force constant can also be determined from the PDOS as [56]:

$$F = \frac{1}{4}\int_0^{\infty} g(E)E\frac{e^{\beta E} + 1}{e^{\beta E} - 1}dE. \tag{2.14}$$

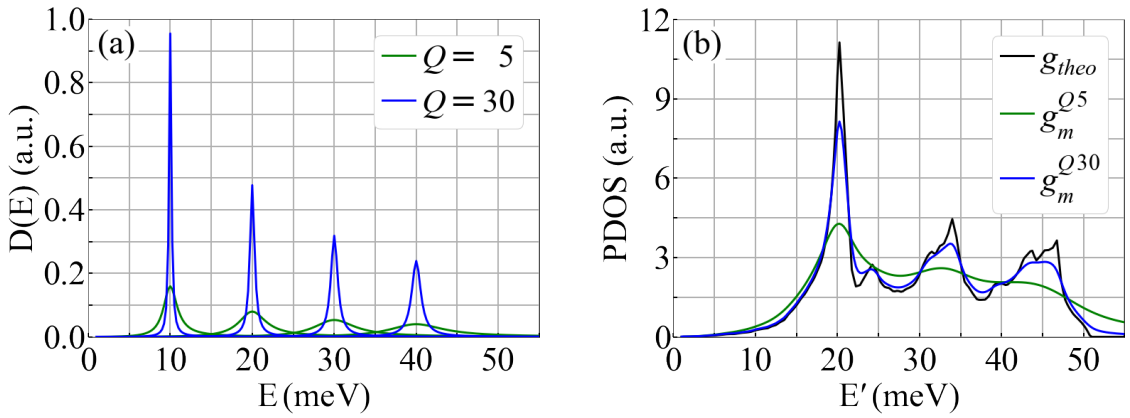

Figure 2.2: (a) DHO functions located at E'=10, 20, 30 and 40 meV with $Q = 5$ and $Q = 30$. (b) *Ab initio* PDOS of α-$FeSi_2$ as calculated (g_{theo}) and convoluted with $D(E', E)$ with $Q = 5$ and $Q = 30$.

2.1.3. Damped harmonic oscillator function

The harmonic approximation used for the description of the lattice dynamics and the first-principles calculations implies an infinite phonon lifetime τ. However, in a real crystal τ is finite, due to scattering at crystallographic imperfections, broken translational symmetry, phonon-phonon interactions and other perturbations. Consequently, the linewidth of each phonon mode Γ is increased ($\Gamma \sim 1/\tau$) and a damping of the overall PDOS features is induced. For the comparison between theory and experiment, this is considered by convolution of the PDOS calculated from first-principles with the damped harmonic oscillator (DHO) function. The equation of motion of a classical damped harmonic oscillator is given by:

$$m\frac{d^2x}{dt^2} + \frac{\sqrt{F\,m}}{Q}\frac{dx}{dt} + kx = 0, \tag{2.15}$$

where m is the mass, F is the force constant and Q is the dimensionless quality factor, which is inversely proportional to the strength of the damping [53]. For a phonon with energy E' the damping can be described by the DHO function [53, 57, 58]:

$$D(E) = \frac{1}{\pi Q\,E'}\frac{1}{\left(\frac{E'}{E} - \frac{E}{E'}\right) + \frac{1}{Q^2}}. \tag{2.16}$$

For large Q values, $D(E)$ resembles a Loretzian function centered at E' having a FWHM $= \omega_0/2Q$, with $\omega_0 = \sqrt{F/m}$ being the frequency of a harmonic oscillator. In Figure 2.2(a) the line shape of $D(E)$ is displayed for different E' and Q values. For a comparison of first-principles calculations and experimental results, the calculated PDOS g_{theo} is convoluted with $D(E', E)$ as:

$$g_m(E') = \int_0^\infty D(E', E)\, g_{theo}(E)\, dE. \tag{2.17}$$

In Figure 2.2(b) the theoretical PDOS of α-$FeSi_2$ is shown as calculated (g_{theo}) and after convolution with $D(E', E)$ using $Q = 5$ (g_m^{Q5}) and $Q = 30$ (g_m^{Q30}). The

convolution introduces an energy dependent broadening of the PDOS features and leads to an increasing number of states at low energies as well as above the cutoff energy. The energy dependence of the damping introduced by the DHO function accounts for the inverse dependence of the phonon lifetime on its frequency [49]. It is essential for the description of phonon damping and cannot be reproduced by other profiles like Loretzian or Gaussian. The convolution of theoretical results with the DHO function has successfully been applied in various publications (e.g. [29, 53, 59, 60]) and is used for the modeling of experimental results with first-principles calculations throughout this thesis.

2.2. Experimental methods

2.2.1. Molecular-beam epitaxy

In molecular-beam epitaxy (MBE), an atomic or molecular beam is used for the growth of micro- and nanostructures with a well-defined orientation with respect to the crystalline substrate. The very low material flux at the substrate position (Å/min) and the ability to instantaneously interrupt the beam of particles with shutters, MBE allows control of the amount of deposited material with the precision of a single atomic layer and below. MBE is conducted in ultrahigh vacuum (UHV) chambers. The UHV is required to ensure that the mean free path of the particles is larger than the distance between source and substrate, and to achieve a crystal growth rate of $\sim 10^5$ times the growth rate from adsorption of surrounding gas par-

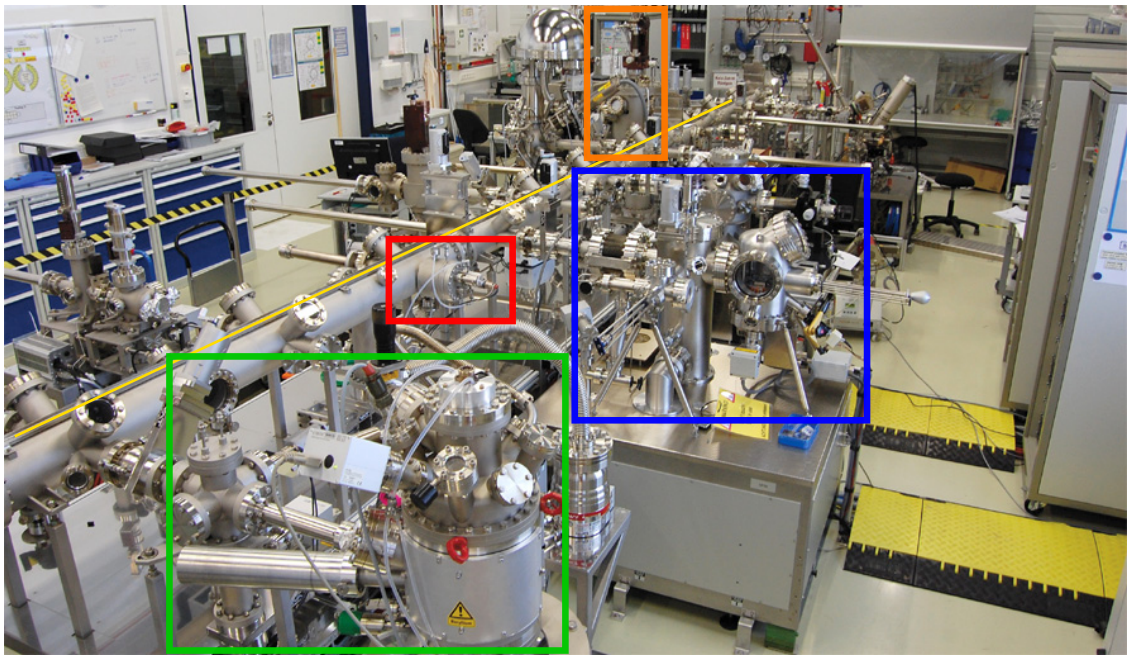

Figure 2.3: UHV-Cluster at the UHV Analysis lab at the KIT. The following chambers are highlighted: MBE growth chamber (orange), scanning probe microscope (blue), heating chamber (red), and sputter chamber (green). All chambers are connected via a UHV transfer line, which is indicated by the yellow line.

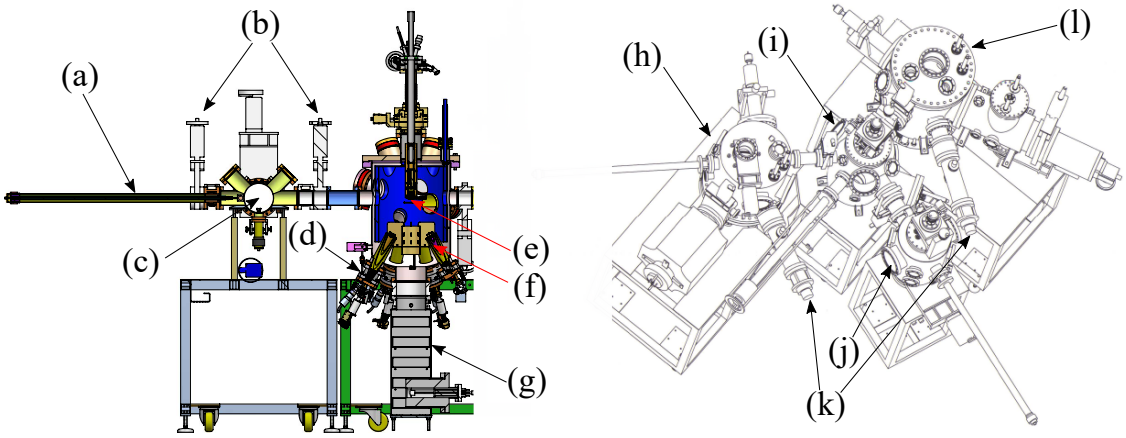

Figure 2.4: left, (a-g): sketch of the UHV-chamber at the UHV Analysis lab at KIT with (a) transfer rod, (b) gate valves, (c) UHV transfer line, (d) EBE, (e) sample stage, (f) effusion cell and (g) ion pump. Right (h-l): sketch of the UHV-chamber at the Paul-Drude-Institut with (h) metal growth chamber, (i) transfer chamber, (j) loading chamber, (k) RHEED, (l) semiconductor (III-V) growth chamber.

ticles [61]. The sublimation of the material either takes place in an effusion cell or an electron beam evaporator (EBE). An effusion cell consists of thermocouples, an inert crucible that contains the material, and a resistive heater that typically reaches temperatures up to about 1500°C. The material flux is determined by the temperature of the crucible. In an EBE, a filament cathode provides electrons by thermionic emission, which are accelerated towards the source anode by a high voltage. The impinging electrons heat the source material and sublimation occurs. Here the material flux is controlled by the emission current of the filament and the acceleration voltage. The UHV is typically reached by a combination of vacuum pumps. Scroll pumps reduce the pressure from ambient pressure to about 10^{-2} mbar. With the use of turbomolecular pumps it can further be reduced to $\sim 10^{-8}$ mbar. The degassing is supported by subjecting the complete UHV-system to a *bakeout* process, i.e. it is heated to 150 °C for 90 hours, while the scroll and turbomolecular pumps are running. After the bakeout, cryogenic or ionic pumps, which trap gas particles by condensing them on their surfaces, further reduce the pressure down to $\sim 10^{-11}$ - 10^{-12} mbar.

The samples discussed in Chapter 5, 6, and 7 were grown in the UHV-Cluster of the UHV Analysis lab at KIT (Fig. 2.3) using the MBE chamber depicted on the left of Figure 2.4. The UHV-Cluster connects several UHV-chambers, dedicated to the growth and characterization of micro- and nanostructures, via a transfer line, which is indicated by a yellow line in Figure 2.3. After loading the substrates through a load lock, they are cleaned by degassing in a heating chamber (red frame in Fig. 2.3). The sample growth is conducted in the MBE chamber (orange frame), equipped with a reflection high-energy electron diffraction (RHEED) instrument. After growth, the samples are transferred in UHV to an Omicron Large Sample scanning probe microscope (blue frame). Several samples were covered with a protective Si capping layer in the sputter chamber visible in the green frame in Figure 2.3 [62].

The samples discussed in Chapter 4 were grown in a MBE system located at the Paul-Drude-Institut in Berlin. A sketch of the system is shown in Figure 2.4 on the right. It consists of a loading chamber and two separate chambers, dedicated to the growth of III-V compounds and metallic structures. Both growth chambers are equipped with RHEED devices for the *in situ* investigation of the growth process.

2.2.2. Structural characterization methods

Reflection high-energy electron diffraction

Reflection high-energy electron diffraction (RHEED) is a powerful technique for investigation of the crystal structure of surfaces and is widely applied in surface science. The instruments can be installed directly at the MBE growth chamber and enable an *in situ* characterization. By thermionic emission an electron beam is created and directed towards the investigated surface by an acceleration voltage, which is typically in the range 10 - 100 keV [63]. The tuning and focusing of the beam is done with electromagnetic deflectors. Due to the large wave vector of the electrons compared to the lattice units in the reciprocal space of the crystal, the Ewald sphere expands over many lattice units. The small incident angle ($1\,^\circ \leq \theta \leq 4^\circ$) and the low penetration depth (few nm) of the electrons make RHEED a highly surface sensitive technique. For example, it is commonly used for the detection of surface reconstructions that are formed by a single atomic layer (e.g. [64]). The intersection of the Ewald sphere and the reciprocal space of the investigated surface are projected onto a fluorescence screen aligned opposite to the electron source. The diffraction pattern is determined by the crystal structure and topology of the surface. In the following paragraph the origin of the RHEED patterns observed for the structures investigated in this thesis are discussed, namely 2D films, 3D islands and 1D nanowires, as summarized in Figure 2.5.

The reciprocal space of a perfectly flat and crystalline surface is formed by crystal truncation rods. The corresponding diffraction pattern is given by the intersection of the Ewald sphere with the truncation rods and consists of spots arranged on the so-called Laue circle [Fig. 2.5(a)] [63]. These conditions are given when the distance between surface steps is larger than the distance over which the electrons interfere coherently. Real surfaces often exhibit a long-range order parallel to the surface plane that is smaller than the electron coherence length, which leads to a broadening of the diffraction spots and the corresponding diffraction pattern consists of parallel streaks [Fig. 2.5(b)] [63]. In case of 3D islands, the electrons are diffracted in a Laue-geometry, and separated diffraction spots are observed [Fig. 2.5(c)]. For uniaxially aligned 1D atomic chains (1D nanowires), the reciprocal space consists of continuous two-dimensional reciprocal space planes (RSPs), which are perpendicular to the chain orientation and exhibit a fixed inter-planar distance of $2\pi/a$, where a is the real space lattice parameter along the chains [65]. When the RHEED pattern is measured with the wave vector of the electron beam being perpendicular to the chain orientation, the intersection of the RSPs and the Ewald sphere projected onto the fluorescence screen consists of straight lines [Fig. 2.5(d)] [64, 66].

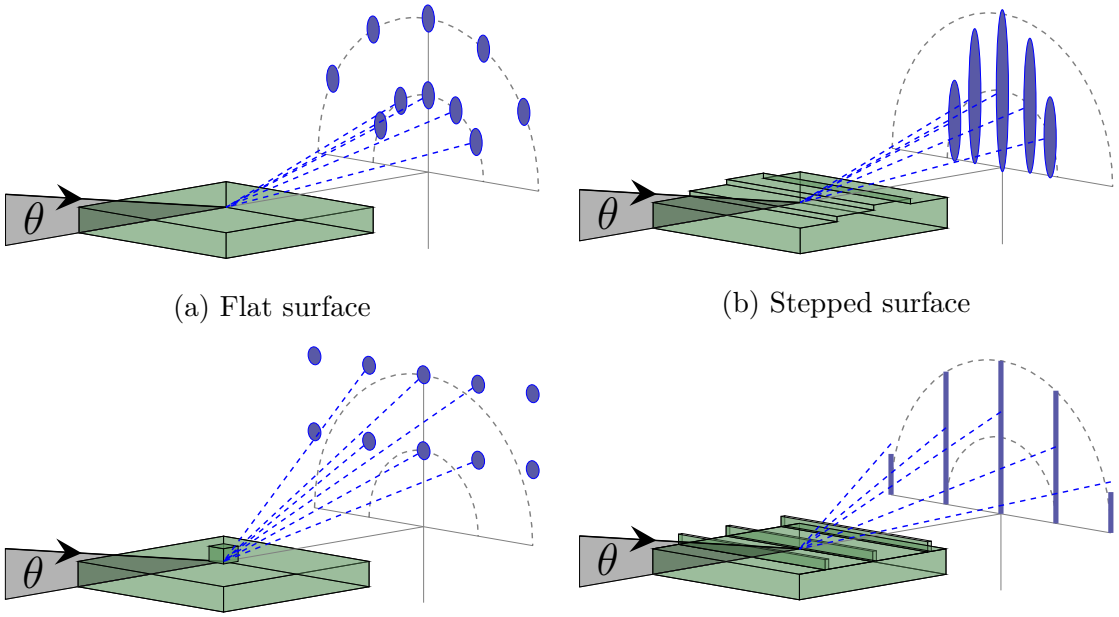

(a) Flat surface

(b) Stepped surface

(c) 3D island

(d) 1D nanowires

Figure 2.5: Experimental geometry of RHEED and patterns observed for different surface topographies. The incidence angle is $1\,^{\circ} \leq \theta \leq 4^{\circ}$. The dashed semicircles indicate the upper part of the Laue circle.

Atomic force microscopy

By atomic force microscopy (AFM) the topography of surfaces can be determined with sub-nanometer resolution. The instrument consist of a sharp tip mounted on a cantilever, a laser/detector unit and an electronic feedback loop. It is mounted on an air-bearing table for decoupling from the surrounding vibrations. The tip-surface interaction is described by the force-distance curve, which is divided into attractive, zero-force and repulsive regions. At relatively large distances between tip and surface, an attractive Van-der-Waals force acts on the tip, and the cantilever is bent towards the surface. After passing through the zero-force region, a repulsive force bends the cantilever away from the surface. The surface is scanned with the tip by piezoelectric motors while the force acting between tip and surface is kept constant. This can be done in contact or non-contact mode. In both cases the measurement is done in the repulsive regime. In contact mode the tip is directly following the surface structure, while in non-contact mode the tip is excited to small amplitudes at its resonant frequency that is kept constant during the scan of the surface. The tapping or intermittent contact mode is a mixture of the above modes and is often applied for samples measured on air. In this mode the amplitude of the oscillation is large enough for the tip to pass from the repulsive region to the attractive region in each oscillation. This enables the measurement of the surface through the contamination layer, which is present as a consequence of condensation of air humidity on the surface. In all three cases, the height of the tip is monitored by a laser, reflected at the top of the cantilever, and a four-segment photodiode. The

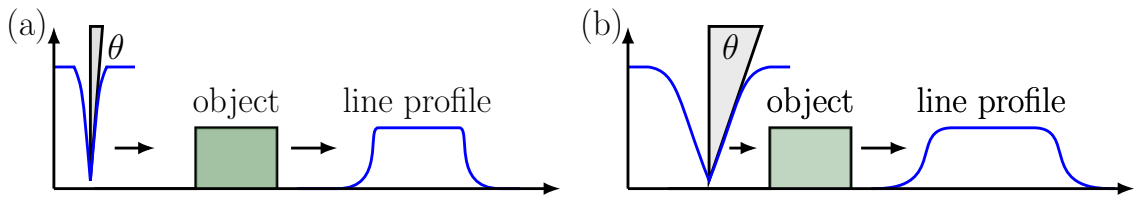

Figure 2.6: Schematic AFM line profile measured with a sharp tip with small opening angle θ (a) and measured with a dull tip with larger θ (b). The tip is moving over the green object with constant distance to the surface, and the blue line profile is measured.

electronic feedback loop ensures a constant force between the tip and the surface. For each point of the scanning sequence a height value is measured and eventually the full three-dimensional information on the surface topography is obtained. The root-mean-square roughness (R_{rms}) gives a measure for the surface roughness by comparison of the height of each individual point Z_i with the average height Z_{ave} of all N measurement points:

$$R_{rms} = \sqrt{\frac{\sum_{i=0}^{N}(Z_i - Z_{ave})^2}{N}} \tag{2.18}$$

The AFM image of a surface is always a convolution of the actual surface topography and the shape of the tip used for the measurement [67]. This becomes especially important when the width of the tip is similar to the size of the measured structure. In Figure 2.6 the effect of an increased tip width on an AFM line profile is depicted in a simplified picture. When the structure is scanned with a sharp tip [Fig. 2.6(a)], the influence of the tip-shape on the measured line profile is minor, whereas the measurement with a dull tip [Fig. 2.6(b)] leads to significant increase in the measured width and a distorted shape of the object. The measured height, however, is not affected by the tip shape.

The AFM measurements discussed in Chapter 5, 6, and 7 where conducted in UHV in the Omicron Large Sample scanning probe microscope shown in Figure 2.3, operated in a non-contact AFM mode with super sharp silicon tips (sss-nch NanoWorld). The radius of the tips is 2 nm at the apex and the half cone angle is <10° at 200 nm from the apex. The measurements described in Chapter 4 were done *ex situ* in a Bruker Dimension 3100 atomic force microscope operated in tapping mode AFM mode.

X-ray absorption fine structure spectroscopy

X-ray absorption fine structure (XAFS) spectroscopy gives access to the local environment of an atom bound in a material [68, 69]. The measured quantity in XAFS is the x-ray absorption coefficient $\mu(E)$ as a function of x-ray energy at and above the absorption edge E_0 of a selected element. Generally, $\mu(E)$ decreases with increasing energy, following approximately an $1/\mathrm{E}^3$ dependence. When the energy is equal to the binding energy of a core-level electron, $\mu(E)$ sharply increases due to photoelectric absorption. Depending on the experimental setup, $\mu(E)$ can be determined

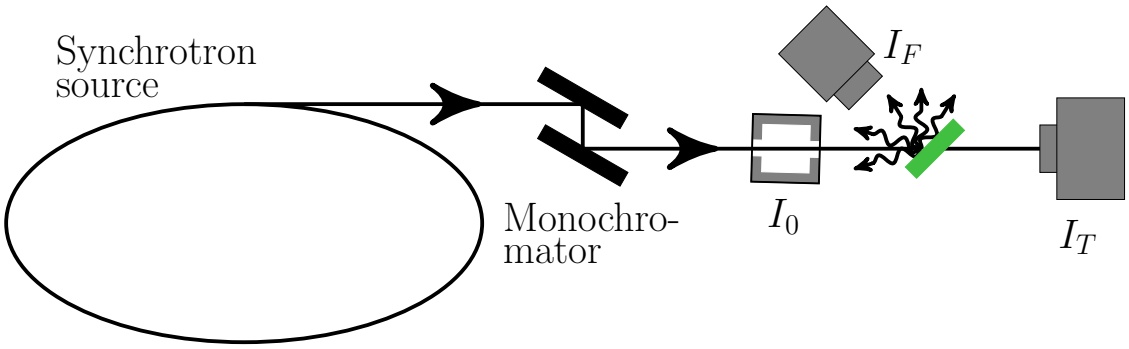

Figure 2.7: Schematic layout of a synchrotron based XAFS spectroscopy station. The energy of the incoming x-ray beam is monochromatized and tuned around the respective absorption edge by a double-crystal monochromator. The incoming flux I_0 can be set to relation either with the detected signal transmitted through the sample I_T or with the fluorescence signal I_F.

by the relation between the intensity of the incoming x-ray beam I_0 and either the intensity of the transmitted photons I_T or the intensity of the fluorescence signal I_F (Fig. 2.7), which occurs when the core hole is filled by a higher level core electron:

$$\mu(E)_T = -\frac{1}{t} ln \left(\frac{I_T}{I_0}\right) \tag{2.19}$$

$$\mu(E)_F \sim \frac{I_F}{I_0} \tag{2.20}$$

where t is the thickness of the sample. Above the absorption edge, the wave vector $\mathbf{k}$ of the emitted core-level photoelectron and its wavelength λ are changing as the difference between E and E_0 increases. The interference of the photoelectron with the surrounding atoms and the incoming x-ray beam gives rise to a sinusoidal variation of $\mu(E)$, i.e. an energy-dependent variation of the x-ray absorption probability. The investigation of the XAFS signal can be separated in two energetic regimes: X-ray Absorption Near-Edge Structure (XANES), which studies the signal in the vicinity of the absorption edge, and Extended X-ray Absorption Fine-Structure (EXAFS), which is focused on the region at 50 - 1000 eV above the absorption edge. Both spectra are analyzed with different methods and contain different information. While XANES gives access to the local site symmetry, charge state and orbital occupancy, the evaluation of EXAFS enables the determination of the local crystal structure around the absorbing atom, namely the interatomic distances as well as the number and type of neighboring atoms.

An EXAFS spectrum of α-$FeSi_2$ nanoislands measured at the Fe K-edge at 7112 eV is shown in Figure 2.8(a). The pre- and post-edge background is subtracted and the spectrum is normalized. In Figure 2.8(b) the EXAFS signal is shown in its k-space representation. The frequency of the signal depends on the interatomic distances, while the amplitude is determined by the type and number of neighboring atoms. By fitting the experimental data [red line in Fig. 2.8(b)] under assumption of a certain crystallographic structure, these parameters and therefore the local crystal structure of the absorbing atom can be determined. To amplify the oscillations at

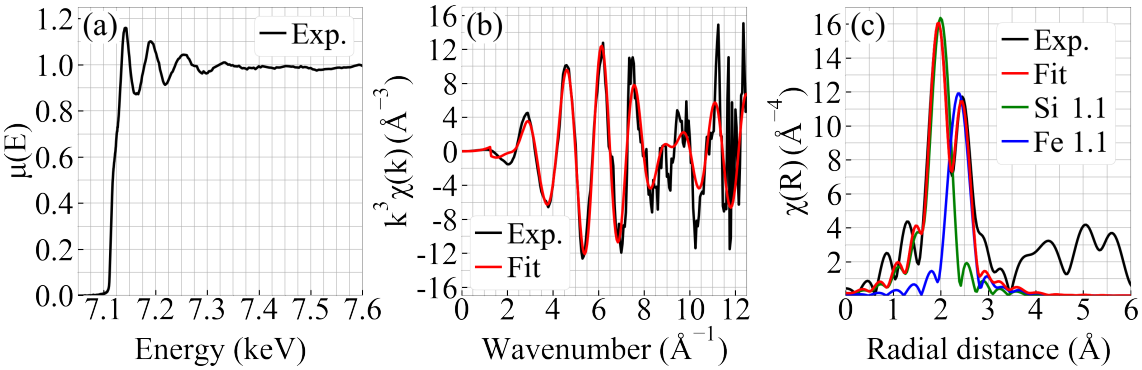

Figure 2.8: (a) Fe K-edge (7112 eV) XAFS signal measured for α-$FeSi_2$ nanoislands after subtraction of the background $\mu_0(E)$ and normalization. (b) Fe K-edge EXAFS spectra obtained from (a) (black line) and the respective best fit results (red line). (c) Fourier transform of the EXAFS spectra shown in (b), together with the respective fit and element-resolved contributions.

higher k values, EXAFS spectra are often weighted by k^1, k^2, or k^3. The interatomic distances can also be represented by the Fourier transform of the EXAFS spectra as shown in Figure 2.8(c). In the presented case the nearest neighbor Si1.1 atoms are located at a distance of 2 Å, while the nearest neighbor Fe1.1 atoms are located at a distance of 2.4 Å.

The EXAFS experiments described in the following chapters were done at the SUL-X beamline of the synchrotron radiation source KARA at KIT. The calibration to the Fe K-edge at 7112 eV was done with an α-Fe metal foil. Subsequently, the fluorescence emission of the nanostructures was recorded up to k=14 $Å^{-1}$. A beam-to-sample-to-detector geometry of 45°/45° was applied, using a collimated x-ray beam of about 0.8 mm × 0.8 mm, or focused x-ray beam with 0.35 mm × 0.15 mm (h × v, FWHM) at the sample position. The obtained extended x-ray absorption fine structure (EXAFS) spectra were processed with the ATHENA and ARTEMIS programs included in the IFEFFIT package [70]. The spectra were weighted by k^1, k^2, k^3 within a k-range of 3.8 – 13.2 $Å^{-1}$. The fitting of the EXAFS spectra presented in the following chapters was done by Dr. Vitova (Institute for Nuclear Waste Disposal, KIT). The data was modeled in the real space with Hanning windows and $dk = 2$ within a range of 1.0 - 2.7 Å using a shell-by-shell approach. Multiple scattering paths did not contribute in the modeled R region. The single scattering paths were calculated with FEFF6 for the crystal structure of α-$FeSi_2$.

2.2.3. Nuclear resonant scattering

The lattice dynamics of the nanostructures investigated in the framework of this thesis was determined by nuclear inelastic scattering of x rays. This method is based on the nuclear resonant absorption/emission of γ-rays, also known as the Mössbauer effect. The basic principles of the latter are briefly described below, followed by a detailed discussion of the nuclear inelastic scattering technique.

The Mössbauer effect

The excited state of a free nucleus exhibits a certain mean lifetime τ and an excitation energy equal to the difference between excited state and ground state $E_0 = E_e$ - E_g. Via the Heisenberg uncertainty principle, the spectral full width at half maximum of the excited state is given by $\Gamma = \hbar/\tau$. The conservation of energy and momentum predicts that the emission or absorption of a photon with energy E_γ is accompanied by the transmission of a recoil to the nucleus. The recoil energy E_R is given by:

$$E_R = E_\gamma^2/2mc^2, \tag{2.21}$$

where m is the mass of the nucleus and c is the speed of light. If the nucleus is not at rest, additionally a Doppler shift energy E_D has to be considered. The de-excitation of the nucleus is accompanied by the emission of a photon with energy:

$$E_\gamma = E_0 - E_R + E_D. \tag{2.22}$$

If $E_D = 0$, the energy difference between the photon emitted by one nucleus and the photon absorbed by another is equal to $2\,E_R$. Precondition for nuclear resonant emission/absorption is a significant overlap in the emission and absorption spectra, which can be formulated by [51]:

$$\Gamma/2E_R > 1. \tag{2.23}$$

In case of ^{57}Fe, Γ=4.65×10^{-9} eV, E_R=1.95×10^{-3}eV and consequently this ratio amounts to 1.2×10^{-6}. Therefore, the combination of the extremely narrow linewidth of the nuclear excited states and large E_R values impedes the observation of nuclear resonant emission/absorption of γ-rays. In principle, the overlap of the spectra can be increased by compensation of E_R by introduction of $E_D \neq 0$, either by fast rotation of the emitter or by heating the emitter and absorber. But both approaches are accompanied by considerable limitations and a practicable implementation in experimental setups for investigation of nuclear excitations has not been achieved.

In 1957 Rudolf Mößbauer demonstrated in his groundbreaking experiments that in case of a nucleus bound in a lattice the recoil is absorbed by the entire crystal. The mass of the nucleus m used in Equation (2.21) is replaced by the mass of the crystal M and E_R approaches negligibly small values [71–73]. Hence, the energy of the emitted photon is equal to the energy of the nuclear transition and the spectra of emission and absorption coincide. This results in an extremely sharp resonant absorption curve with a linewidth of 2×Γ. According to the Einstein model, the vibrations of atoms bound in a crystal around their equilibrium positions are described by phonons with a single vibrational frequency ω and energies equal to integer multiples of $\hbar\omega$. If $E_R \leq \hbar\omega$ a transfer of the recoil to the lattice is not possible and recoilless resonant emission/absorption is observed. The relative strength of the recoilless fraction is described by the Lamb-Mössbauer factor f_{LM} [71, 74]. It can be derived from the wave vector k of the resonant photon and the mean square displacement $\langle x^2\rangle = \frac{1}{2}\Sigma_m x_m^2$ as [75]:

$$f_{LM} = exp(-k^2\langle x^2\rangle). \tag{2.24}$$

To yield a reasonable fraction of recoilless resonant emission/absorption both components of the exponent may not exceed certain values. For instance, the measurement of gases or liquids is significantly complicated by the large $\langle x^2 \rangle$ values. Also, the maximum energy of the nuclear transition is limited to about 150 keV [75] and therefore only nuclear transitions with relatively low energies are observable.

Nuclear inelastic scattering

After discovery of the Mössbauer effect it was soon realized that in principle it could be used as a method for probing the lattice dynamics [76]. However, in a conventional Mössbauer setup the measurement of phonons, who exhibit energies up to about 100 meV, requires very high source velocities to generate the Doppler shift necessary for probing the entire spectral range. Therefore, experiments investigating lattice dynamics by the means of conventional Mössbauer spectroscopy remained scarce (e.g. [77]). These limitations where overcome by the excitation of nuclear energy levels with synchrotron radiation (SR), which was first proposed by Ruby [78] and later experimentally realized by the pioneering works of Cohen et al. [79] and Gerdau et al. [80]. The 3^{rd} generation synchrotron sources sparked the development of a new field, called nuclear resonant scattering (NRS), which can be seen as an advancement of conventional Mössbauer spectroscopy. Nowadays, NRS is the hypernym for several methods based on the nuclear excitation with SR. They can be classified by elastic/inelastic as well as coherent/incoherent scattering processes [81]. It was shown by Seto et al. [27] and Sturhahn et al. [28] that the inelastic and incoherent scattering of x rays, named *nuclear inelastic scattering* (NIS), can be used for the determination of the PDOS and the thermodynamic and elastic properties of Mössbauer-active isotopes. In the following paragraph the basic principles of this method are explained.

The lifetime of a nuclear excited state ($\tau \sim 10^{-9}$ s) is by orders of magnitude larger than the lifetime of an electronic excitation ($\tau \sim 10^{-12}$ s). Therefore, the use of pulsed SR radiation allows for a temporal separation of the two scattering signals, and enables a measurement of the delayed nuclear signal without any background of the quasi prompt electronic signal. The deexcitation of a nucleus occurs via two channels: radiative decay or internal conversion. Radiative decay denotes the resonant emission of γ-ray fluorescence radiation with the same energy as the nuclear excitation. The relative probability of this channel is given by $1/(1+\alpha)$, where α is the internal conversion coefficient. In case of internal conversion, the energy of the excited nucleus is transmitted to the electron shell. A conversion electron is emitted from the K-shell of the atom and the hole created is filled with an electron from a higher shell under the emission of x-ray fluorescence radiation or an Auger electron. The relative probability of this channel is $\alpha/(1+\alpha)$. For most Mössbauer-active isotopes $\alpha \gg 1$ and internal conversion is the dominant process. Furthermore, the typically used detectors are more sensitive to the lower energy K-fluorescence compared to the resonant γ-ray fluorescence. A strong trapping of the γ-ray fluorescence and Auger electrons is present in the sample, which further reduces the yield of this signal. Hence, in NIS experiments typically the signal of the K-fluorescence is detected. For ^{57}Fe the respective energy is equal to 6.4 keV

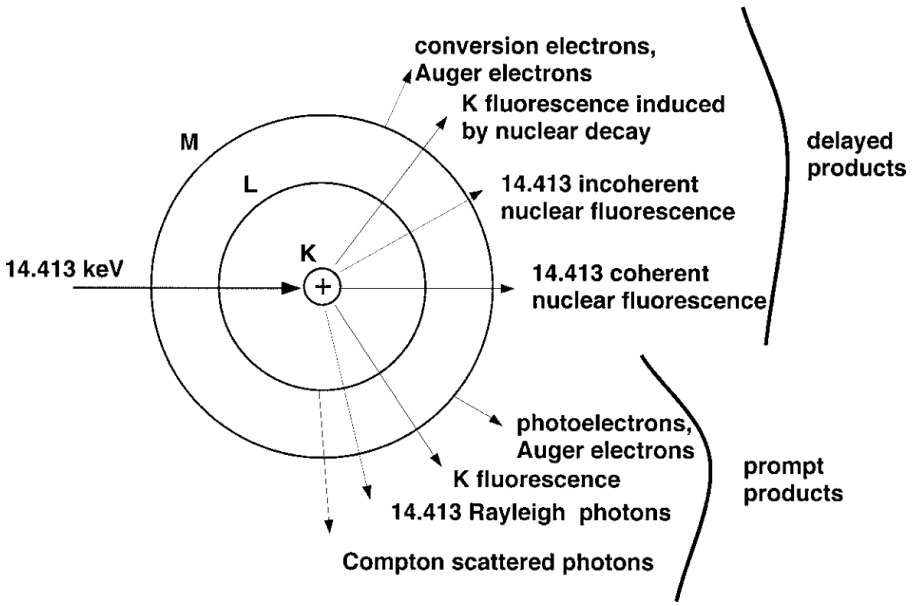

Figure 2.9: Simplified scheme of the deexcitation channels of the ^{57}Fe nuclear resonance at 14.413 keV [82]. Typically, the delayed K_α- and K_β-fluorescence at 6.4 and 7.05 keV, respectively, are detected as a function of the incident photon energy.

for K_α and 7.05 keV for K_β. In Figure 2.9 an overview of the various deexcitation processes is given.[i]

Figure 2.10(a) shows an exemplary result of a normalized NIS spectrum measured at room temperature on the ^{57}Fe resonance of an α-$^{57}FeSi_2$ crystal. The intensity of the K-fluorescence is obtained as a function of the energy of the incoming x-ray beam (E'), which is tuned around the ^{57}Fe resonant transition (E_0) at 14.413 keV, and normalized as described below. Since E' only matches E_0 of ^{57}Fe, the NIS spectrum does not contain any contribution of the Si atoms or other Fe isotopes and therefore enables an element and isotope selective measurement. The energy scale is given as $E = E' - E_0$. For $E = 0$ the intense peak of the elastic nuclear resonance is observed, denoted with S_0 in Figure 2.10(a). If $E \neq 0$ energy is transferred between the incoming photon and the crystal lattice and an inelastic, phonon-assisted excitation of the nucleus occurs. For ($E < 0$) the annihilation and for ($E > 0$) the creation of a single phonon [S_1 in Fig. 2.10(a)] or multiple phonons [S_n in Fig. 2.10(a)] compensates the energy difference between E' and E_0. All phonons which are allowed by the dispersion relations for a particular energy transfer contribute to the measured signal, independent of their respective momentum. Therefore, NIS is a phonon "momentum-integrated" technique for the measurement of lattice dynamics [30].

[i] In literature, *nuclear inelastic scattering* (NIS) is also refereed to as *nuclear resonance vibrational spectroscopy* (NRVS) and *nuclear resonant inelastic x-ray scattering* (NRIXS) . The term *nuclear inelastic scattering* correctly describes the process of radiative decay. On the other hand, in case of internal conversion *nuclear inelastic absorption* would be the appropriate term. Although this channel is typically used in experiments, *nuclear inelastic scattering* is still used for a better distinction from the widely known techniques of *inelastic neutron or x-ray scattering*.

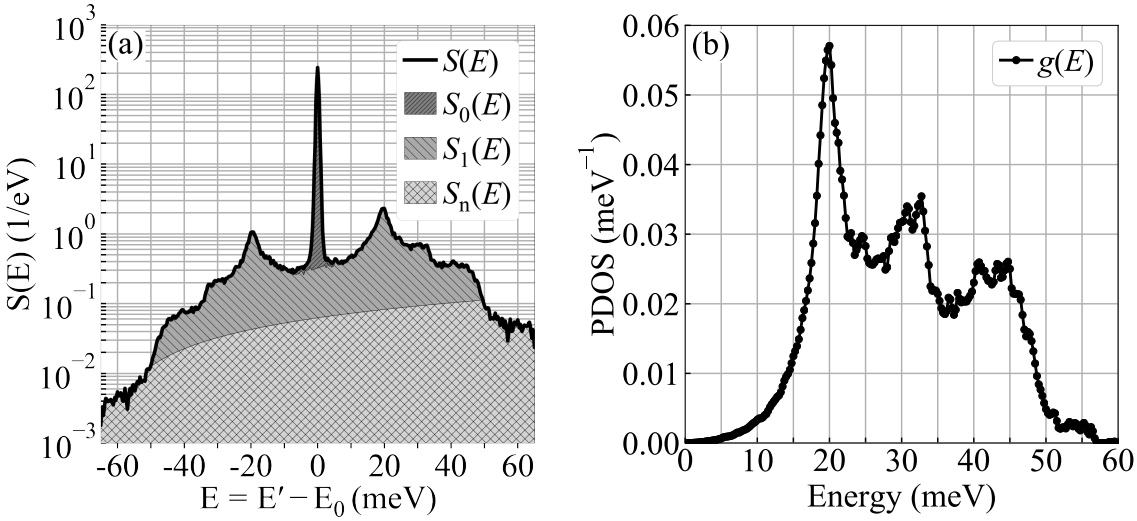

Figure 2.10: (a) Normalized probability of nuclear inelastic absorption $S(E)$ measured relative to the ^{57}Fe resonance E_0 at 14.413 keV on α-$FeSi_2$ nanoislands. The spectrum is divided into its elastic ($S_0(E)$) and inelastic ($S_1(E)$, $S_n(E)$) components. (b) Normalized phonon density of states $g(E)$ calculated from $S_1(E)$.

The dependence of the measured intensity of the K-fluorescence signal on the photon energy is given by [28, 83]:

$$I(E) = I_0 \rho \sigma \frac{\eta_K \alpha_K}{1+\alpha} \frac{\pi}{2} \Gamma S(E, \mathbf{k}) \tag{2.25}$$

where I_0 is the incident photon flux, ρ the effective area density of nuclei, σ the nuclear resonant absorption cross section, η_K the fluorescence yield, α and α_K the total and partial internal conversion coefficients, respectively, Γ the linewidth of the nuclear excitation, and $\mathbf{k}$ the wave vector of the incoming photon. $S(E, \mathbf{k})$ stands for the normalized probability of nuclear inelastic absorption and is given by [84, 85]:

$$S(E, \mathbf{k}) = \frac{1}{2\pi} \int \exp\left(-iE\tau - \frac{\Gamma}{2}|\tau|\right) \frac{1}{n_r} \sum_m F_m(\mathbf{k}, \tau) d\tau \tag{2.26}$$

where n_r is the total number of resonant nuclei in the unit cell, which are labeled with index m. $F(\mathbf{k}, t)$ denotes the space-time correlation function introduced by van Hove [86] which describes the correlation of the displacements of the nucleus in two different moments in time separated by the time interval $t = \hbar\tau$ under harmonic approximation. $S(E, \mathbf{k})$ can be decomposed in terms of a multiphonon expansion [85]:

$$S(E, \mathbf{k}) = f_{LM} \left(\delta_\Gamma(0) + \sum_{n=1}^{\infty} S_n(E, \mathbf{k})\right) \tag{2.27}$$

$$= f_{LM}\, \delta_\Gamma(0) + S'(E, \mathbf{k}) \tag{2.28}$$

where $\delta_\Gamma(0)$ is the elastic part of the absorption, i.e. the zero-phonon excitation, and the n-th term of $S'_n(E, \mathbf{k})$ denotes the inelastic absorption accompanied by the creation or annihilation of n phonons.

In the reference system of a vibrating nucleus, the energy of an incoming photon is determined by the projection of the velocity of the nucleus to the wave vector $\mathbf{k}$ of the photon [87]. In a lattice with cubic symmetry the vibrational velocities along the main crystallographic directions are equal and $S(E, \mathbf{k})$ is isotropic. In case of polycrystalline or powder samples an average velocity of all phonon modes is projected to $\mathbf{k}$ and consequently an isotropic, averaged $S(E, \mathbf{k})$ is measured. In a single crystalline lattice with non-cubic symmetry, however, the different force constants along the main crystallographic directions lead to anisotropic velocities of the nuclei. Therefore, NIS enables the determination of the anisotropic $S(E, \mathbf{k})$ in single crystalline non-cubic lattices [84, 87]. This anisotropy can be very pronounced, as will be demonstrated later for α-$FeSi_2$.

The Lipkin sum rules [88, 89] allow to directly extract a number of quantities from $S(E, \mathbf{k})$ by calculating its first three moments:

$$\int ES(E, \mathbf{k})dE = E_R \tag{2.29}$$

$$\int (E - E_R)^2 S(E, \mathbf{k})dE = 4E_R T \tag{2.30}$$

$$\int (E - E_R)^3 S(E, \mathbf{k})dE = \frac{\hbar^2}{m} E_R F \tag{2.31}$$

where T is the average kinetic energy of the resonant nuclei and F is the mean force constant of the bound nuclei.

The nuclear resonant absorption cross section is by orders of magnitude larger for $E = 0$ compared to $E \neq 0$ [81]. This leads to significant differences in penetration depth and consequently different numbers of nuclei involved in the elastic and the inelastic processes. The resulting bias in the relative contributions to $S(E, \mathbf{k})$ is described by:

$$I(E, \mathbf{k}) = A\ (S'(E, \mathbf{k}) + C\, f_{LM}\, \delta_\Gamma(0)) \tag{2.32}$$

Under consideration of Equation (2.29) the normalization factor A can be calculated as:

$$A = \frac{1}{E_R} \int E\, I(E, \mathbf{k})dE. \tag{2.33}$$

With this, the inelastic part of the measured intensity $I'(E, \mathbf{k}) = A\, \Sigma_{n=1}^{\infty} S'_n(E, \mathbf{k})$ can be determined by subtraction of the elastic peak. Since $\int S'(E, \mathbf{k}) = 1 - f_{LM}$ the Lamb-Mössbauer factor can directly be derived as:

$$f_{LM} = 1 - \frac{1}{A} \int I'(E, \mathbf{k})dE \tag{2.34}$$

and consequently the mean square displacement of the nuclear resonant nuclei can be determined (eq. 2.24) to be:

$$\langle x^2 \rangle = -\frac{ln(f_{LM})}{\mathbf{k}^2}. \tag{2.35}$$

Under the assumption of a harmonic behavior of the lattice, the single and multi-

phonon terms of the series expansion in Equation (2.27) are given by [84]:

$$S_1(E,\mathbf{k}) = \frac{E_R\ g(E,\mathbf{s})}{E(1-e^{-\beta E})} \qquad n=1 \tag{2.36}$$

$$S_{n>1}(E,\mathbf{k}) = \frac{1}{n}\int_{-\infty}^{\infty} S_1(E')S_{n-1}(E-E')dE' \qquad n>1 \tag{2.37}$$

where $\mathbf{s} = \mathbf{k}/k$ and $g(E,\mathbf{s})$ is the normalized phonon density of states (PDOS) [51]:

$$\int_0^{\infty} g(E)dE = 1. \tag{2.38}$$

The relative contribution of the n-phonon term is given by [85]:

$$\int S_n(E)dE = \frac{-ln(f_{LM})^n}{n!}. \tag{2.39}$$

Consequently, for f_{LM} close to unity the series expansion converges rapidly and the one-phonon term is dominant. However, in case of small f_{LM} values the multiphonon contribution cannot be neglected, and the calculation of $g(E,\mathbf{s})$ from $S_1(E,\mathbf{k})$ using Equation (2.37) requires further considerations.

The ratio of the one-phonon absorption probability obtained for positive and negative value of E is universally given by the *detailed balance* $S_1(E>0) = e^{-\beta E}S_1(E<0)$. For the calculation of the PDOS both sides of the spectrum can be used and $g(E)$ can be written as [81]:

$$g(E,\mathbf{s}) = \begin{cases} \frac{E}{E_R} tanh\left(\frac{\beta E}{2}\right)\left(S_1(E,\mathbf{k}) + S_1(-E,\mathbf{k})\right) & \text{for } E>0 \\ 0 & \text{for } E\leq 0 \end{cases} \tag{2.40}$$

As discussed above for $S(E,\mathbf{k})$, the PDOS obtained by NIS for an anisotropic single-crystalline lattice depends on the relative orientation of the wave vector $\mathbf{k}$ of the x-ray beam with respect to the main crystallographic directions.

It was shown by Hu et al. [90] that the low-energy part of the PDOS obtained by NIS is related to the velocity of sound v_s by:

$$\lim_{E\to 0}\frac{g(E)}{E^2} = \frac{m}{\rho}\frac{1}{2\pi^2\hbar^3 v_s^3} \tag{2.41}$$

where m is the mass of the resonant nuclei and ρ is the mass density. Unlike the properties determined above, v_S is not an isotope specific property but gives information on the entire lattice in case of compound materials.

Experimental setup

The main challenges in a NIS experiment are to provide an extremely bright x-ray beam, which is matching the transition energy of the nucleus and is monochromatized to the meV range, and to detect the signal of the weak phonon side bands of the resonant elastic peak against the intense prompt signal (i.e. $S_1(E)$, $S_n(E)$ against $S_0(E)$ in Figure 2.10). These requirements are met at dedicated beamlines

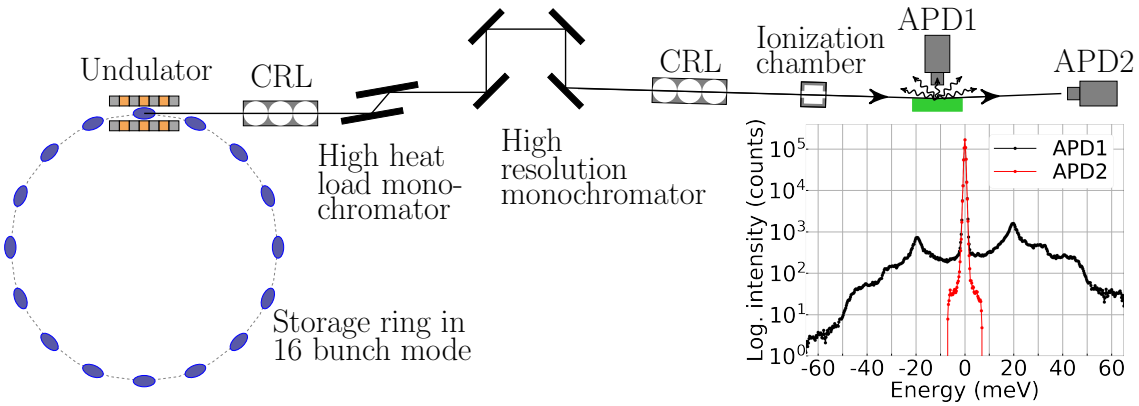

Figure 2.11: Schematic layout of a NRS beamline. The functionality of the respective components is discussed in section 2.2.3. On the right an experimental result obtained at room temperature on α-$FeSi_2$ nanoislands is shown. APD1 detects the inelastic signal of the K-fluorescence, APD2 the elastic nuclear forward scattering signal.

at the 3^{rd} generation synchrotron radiation facilities of ESRF, APS, PETRA III and SPRING-8. The measurements discussed in this thesis were conducted at the beamlines ID18 [91] of the ESRF and P01 [92] of PETRA III. In Figure 2.11 a scheme of a beamline setup for NIS experiments is given. For the time discrimination between the prompt electronic and delayed nuclear signal, the storage ring has to be operated in a suitable timing mode. This is realized by arranging the circulating electrons in the storage ring in bunches, e.g. in case of the ESRF in a 16 bunch mode, which implies an interval of Δt=176 ns between the pulses, or in the larger ring of PETRA III a 40 bunch mode with Δt=192 ns. The SR is generated by deflection of the electrons in bending magnets, wigglers or undulators. Due to the demand for high flux in a narrow spectral range, the latter are required for NRS experiments. The undulator consists of a regular array of permanent magnets with alternating polarization directions, which create a periodic magnetic field. Electrons passing through that field are forced to oscillate sinusoidally with a period of a few centimeters and emit SR in narrow energy bands of the spectrum. The linearly polarized SR is very intense ($\sim 10^{13}$ photons/sec/eV) and highly collimated ($\sim$8-12 μrad vertically, $\sim$20-40 μrad horizontally) [82]. A detailed discussion of SR used for NRS experiments is given in [93]. The undulator spectrum is narrowed down to FWHM$\sim$eV at the nuclear transition energy by a high-heat-load monochromator. Subsequently, the monochromatization is further increased to the meV range by a high-resolution monochromator (HRM). An HRM consists of a series of perfect silicon single crystals which employ Bragg diffraction of high order symmetric and asymmetric reflections to increase the resolution by factor of 10^7 with an efficiency of about 50%. An overview on the monochromatization of synchrotron radiation for NRS experiments is given in [94]. By adjusting the angles between the HRM crystals with high precision piezo motors with a mechanical resolution of $\sim$25 nanorad, the beam energy can be set in a range of hundreds of meV, which is much larger than the energy range in which lattice vibrations occur. Compound refractive lenses (CRLs) and/or Kirkpatrick-Baez mirrors are used for the focusing of the beam. The intensity I_0 of

the incoming beam is measured for normalization of the obtained scattering signal by an ionization chamber. NIS experiments on nanostructures grown on substrates are typically conducted in grazing incidence geometry, to ensure a large footprint of the beam in order to maximize the available scattering volume. For the measurement of the nuclear decay signal, the detectors have to be able to sustain the immense intensity of the prompt electronic scattering and to measure single delayed photons within the lifetime of the nuclear excitation of several tens of nanoseconds. Avalanche photoiodes (APDs) exhibit a time resolution in the nanosecond range and by timing of the APD with respect to the bunch structure of the storage ring, the delayed nuclear decay signal can be measured without any background from electronic scattering. The noise level is determined by the detector itself and the downstream electronics and is typically low. Two APDs are used in the experimental setup. The first (APD1 in Fig. 2.11) records the K-fluorescence signal, which is emitted over the full solid angle, therefore the detector has to be as close to the sample as possible. In ambient pressure experiments the distance between sample surface and the active zone of the APD is ∼1mm. The second (APD2 in Fig. 2.11) records the coherent elastic signal of nuclear forward scattering (NFS). In Figure 2.11 the inset on the right displays the spectra measured by the respective detectors for an NIS experiment conducted at room temperature on α-$FeSi_2$ nanoislands. APD1 records the spectrum of phonon-assisted nuclear inelastic absorption used to determine the PDOS of the material as discussed above. The NFS spectrum obtained with APD2 is used for subtraction of the elastic peak from the NIS signal, for determination of the experimental resolution and as a precise energy reference. In contrast to conventional Mössbauer spectroscopy, the resolution of NRS experiments is not determined by the natural linewidth of the excited nuclear state, but by the bandwidth of the high resolution monochromator. An overview on the detectors used for NRS experiments is given in [95].

2.2.4. *Ab initio* lattice dynamics

For a thorough comprehension of the experimentally obtained PDOS a comparison with theoretical results is indispensable. Over the last two decades, first-principles calculations, also called *ab initio* calculations, based on the density functional theory (DFT) have proven to be a powerful theoretical approach for the determination of the lattice dynamics of crystals [96, 97]. This approach only requires very basic parameters for calculation of the complete vibrational behavior of a lattice, namely the mass and number of the atoms of the constituents and the structure of the lattice. In a first step this input is used to calculate the ground state of the electronic system under adiabatic approximation, i.e. with the nuclei being at rest. The Hohenberg-Kohn theorem [98] states that this ground state can unambiguously be described by the electron density of the system. The total energy is a unique functional of the electron density which consequently defines the potential of the system. Furthermore, the theorem states that the ground state of the electron density also minimizes the total energy and therefore determines all physical properties of the system. With this the $3N$ dimensional problem of solving the Schrödinger equation for a lattice containing N atoms is reduced to the three dimensional description

of the electron density. After stabilization of the system, the Hellmann-Feynman forces are obtained by displacing the nonequivalent atoms from their equilibrium positions. The phonon dispersion relations are obtained for the high symmetry directions by solution of the Kohn-Sham equations [99] by the direct method [100] under the local-density approximation.

An important aspect of the *ab initio* calculations performed for comparison with the experimental results obtained within this thesis is the calculation of the direction projected PDOS in anisotropic crystals. For the comparison of theory and experiment, the relative contributions of the PDOS projected along the main crystallographic directions have to be determined. In the *ab initio* calculations the phonon normal modes are obtained by solving the eigenvalue problem of the dynamical matrix $D(\mathbf{k})$:

$$D(\mathbf{k})\mathbf{e}(\mathbf{k}_j) = \omega^2(\mathbf{k}_j)\mathbf{e}(\mathbf{k}_j) \tag{2.42}$$

where $\omega(\mathbf{k}_j)$ denotes the phonon frequencies for wave vector $\mathbf{k}$ and phonon dispersion band index j, and $\mathbf{e}(\mathbf{k}_j)$ are the phonon polarization vectors. In an alternative formulation to Equation (2.6), the PDOS is given by:

$$g(\omega) = \frac{1}{3N}\sum_j \int_{BZ} \delta\left(\omega - \omega(\mathbf{k}_j)\right) d^3\mathbf{k} \tag{2.43}$$

where N is the number of states and the integral over BZ stands for the summation over all $\mathbf{k}$ values within the Brillouin zone. Generally, the symmetric tensor $G^{\mu}_{il}(\omega)$ can be defined [101]:

$$G^{\mu}_{il}(\omega) = \frac{1}{3N}\sum_j \int_{BZ} e^{\mu}_i(\mathbf{k}_j)[e^{\mu}_l(\mathbf{k}_j)]^* \delta(\omega - \omega(\mathbf{k}_j)) d^3\mathbf{k} \tag{2.44}$$

where μ denotes an individual atom and the indexes i, l define the Cartesian components of the polarization vector $\mathbf{e}$. The PDOS projected along the main crystallographic directions of the lattice, i.e. for the crystals investigated within this thesis x, y and z, can be calculated by the diagonal elements, $G^{\mu}_{xx}(\omega)$, $G^{\mu}_{yy}(\omega)$, and $G^{\mu}_{zz}(\omega)$. The PDOS projected along an arbitrary direction $\boldsymbol{\kappa}$ can be obtained from $G^{\mu}_{il}(\omega)$ by:

$$g^{\mu}_{\kappa}(\omega) = \sum_{i,l=1}^{3} \kappa_i \kappa_l G^{\mu}_{il}(\omega) \tag{2.45}$$

where κ_i, κ_l are the Cartesian components of $\boldsymbol{\kappa}$. For the comparison with NIS measurements, $g^{\mu}_{\kappa}(\omega)$ is calculated by assuming that $\boldsymbol{\kappa}$ is oriented along the wavevector of the incoming x-ray beam, and μ denotes the Mössbauer-active isotope.

The *ab initio* calculations presented in the following chapters were performed within the DFT implemented in the VASP code [102, 103], employing the generalized gradient approximation [104, 105]. The interaction between ions and electrons was described using the projector augmented-wave method [106, 107]. The phonon dispersion relations are calculated using the direct method incorporated into the PHONON program [108]. All *ab initio* calculations presented in this thesis were performed by Dr. habil. Piekarz, Dr. Sternik, Dr. Sikora and Dr. Ptok at the Institute of Nuclear Physics (PAS) in Krakow, Poland.

3. Properties of iron silicides

The following chapter gives an overview of the structural properties of the investigated iron silicides, i.e. Fe_3Si, β-$FeSi_2$ and α-$FeSi_2$. The literature on the growth of Fe_3Si on the GaAs(001) surface and of $FeSi_2$ nanostructures on the Si(111) and Si(110) surface is summarized. Furthermore, the *ab initio* calculated phonon dispersion relations and phonon density of states of Fe_3Si, β-$FeSi_2$ and α-$FeSi_2$ are presented.

3.1. Structural properties of iron silicides

The Fe-Si phase diagram shows a rich variety of compounds that span over a wide range of stoichiometries, Fe_3Si, Fe_2Si, Fe_5Si_3 FeSi and $FeSi_2$ [109, 110]. Schematic representations of the unit cells of the compounds investigated within this thesis, i.e. Fe_3Si, β-$FeSi_2$ and α-$FeSi_2$, are given in Figure 3.1.

The ferromagnetic Fe_3Si exhibits a cubic DO_3 structure (space group $Fm\bar{3}m$) with a lattice parameter $a = 5.64\,\text{Å}$ [111] and a Curie temperature $T_C = 567\,^\circ\text{C}$ [38]. The compound is stable over a wide range of Si content, from 10 to 26.6 atomic percent Si [112]. The crystallographic structure is preserved in the off-stoichiometric region by occupation of Si lattice sites by Fe atoms and vice versa [113]. Fe_3Si can be assigned as a full Heusler alloy consisting of four interpenetrating fcc sublattices at the positions A(0,0,0), B(0.25,0.25,0.25), C(0.5,0.5,0.5), and D(0.75,0.75,0.75). The A, B and C sublattices are occupied by Fe atoms, the D sublattice by Si atoms. The Fe[B] sites, which are located in the mixed Fe/Si layers in the Fe_3Si unit cell, have 8 iron atoms as nearest neighbors, the Fe[A,C] sites 4 iron and 4 silicon atoms. The first coordination sphere and the magnetic moment of the Fe[B] atoms are the same as in the *bcc* crystal phase of Fe , $\mu_{\text{Fe[B]}} = 2.2\mu_B$, while the magnetic moment of the Fe[A,C] atoms is reduced to $\mu_{\text{Fe[A,C]}} = 1.35\mu_B$. The Si atoms have a negative magnetic moment of $\mu_{\text{Si}} = -0.07\mu_B$ [114].

$FeSi_2$ is a particularly interesting member of the technologically important class of transition metal silicides, since it is the only representative that forms metallic and semiconducting phases. The orthorhombic unit cell of the semiconducting β-$FeSi_2$ [Fig. 3.1(b)] belongs to the $Cmca$ space group and exhibits lattice parameters $a = 9.86\,\text{Å}$, $b = 7.79\,\text{Å}$ and $c = 7.88\,\text{Å}$ [115]. It contains 8 Fe and 16 Si atoms with two nonequivalent sites for each element. The material exhibits a direct band gap in the range of $0.84-0.88\,\text{eV}$ [42, 43, 116, 117] and was promoted as a promising candidate for applications in optoelectronics [41] and photovoltaics [44, 45]. At low temperatures an additional indirect band gap was revealed and strong electron-phonon coupling was evidenced [118, 119]. Furthermore, a relatively high thermoelectric figure-of-merit ZT=0.4 can be achieved upon doping, leading to the consideration of β-$FeSi_2$ for applications in this field [46].

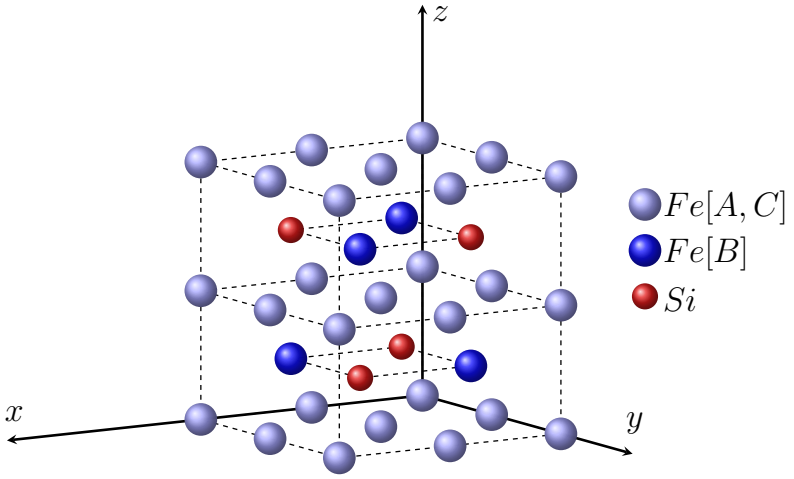

(a) Fe_3Si unit cell

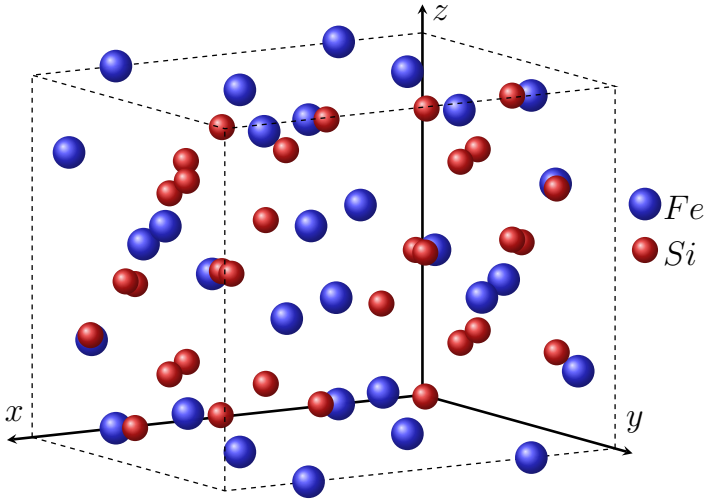

(b) β-$FeSi_2$ unit cell

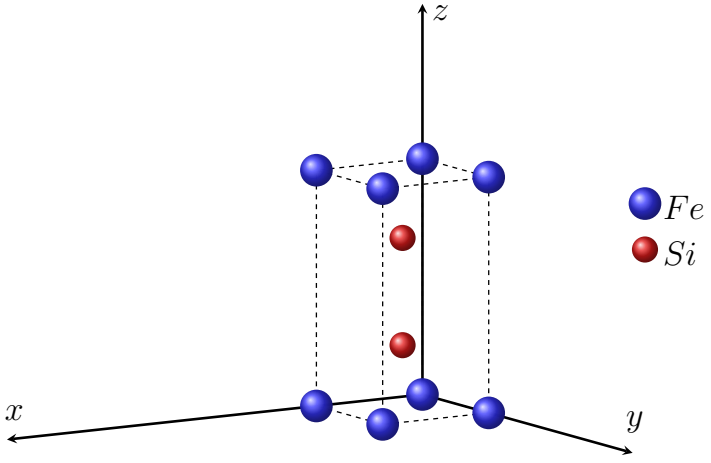

(c) α-$FeSi_2$ unit cell

Figure 3.1: Schematic representation of the unit cells of the investigated iron silicides. The lattice parameters are given in section 3.1.

Above temperatures of 950 °C, β-$FeSi_2$ is reversibly transformed into the metallic high-temperature α-$FeSi_2$ phase [110, 117]. The tetragonal unit cell of α-$FeSi_2$ [Fig. 3.1(c)] belongs to the space group $P4/mmm$ and exhibits lattice parameters $a = b = 2.70$ Å and $c = 5.14$ Å and an internal atomic position of the Si atoms $z = 0.2725$ [101, 120]. Due to the small lattice mismatch of certain crystallographic planes of α-$FeSi_2$ and silicon, this phase can be stabilized in nanostructures grown on silicon surfaces [121]. Magnetic measurements on such surface-stabilized α-$FeSi_2$ at room temperature revealed a superparamagnetic behavior [122, 123]. For thin films of α-$FeSi_2$ a ferromagnetic-semiconductor-like behavior was observed below 50 K [124]. Moreover, theoretical studies showed that changes in the stoichiometry induce magnetism in α-$FeSi_2$ and that an increase of the Si content may even lead to ferromagnetism [125].

3.2. Growth of iron silicide nanostructures

The magnetic and structural properties of Fe_3Si promoted this material as a promising candidate for device applications, for example in high density magnetic data storage, and as a model system for the investigation of spintronic systems. Fe_3Si exhibits a spin polarization of 45 % [111], and room-temperature spin injection from Fe_3Si into GaAs, Ge and Si has been reported [38–40]. One of the key issues for the realization of Fe_3Si based devices is the growth of micro- and nanostructures with a high structural quality on semiconductor substrates. This has been achieved in various configurations, inter alia on Ge(111), Ge(110) and Ge (001) [126–129], Si(111) [130, 131] and GaAs(111) [132]. A novel approach for the growth of Fe_3Si nanostructures is the coating of single-crystalline GaAs nanowires with an epitaxial Fe_3Si shell, resulting in the formation of 'nanobar magnets' [37]. Since (001) oriented substrates are prevalent in the semiconductor industry, also the growth of Fe_3Si/GaAs(001) heterostructures has thoroughly been investigated. The Fe_3Si/GaAs(001) interface offers the possibility to grow epitaxial heterostructures with a high degree of crystalline perfection of the film and the interface. The preparation of atomically flat GaAs(001) surfaces for the overgrowth with Fe_3Si films is a well established process. In case of correct stoichiometry of the silicide, the lattice mismatch between Fe_3Si and GaAs ($a_{GaAs} = 5.65$ Å) is below 0.5% and almost strain-free interfaces can be grown [38, 133, 134]. Consequently, the stoichiometry of the Fe_3Si layer can precisely be controlled by x-ray diffraction measurements, since the diffraction peaks of Fe_3Si and GaAs only occur at the same position in case of the ideal Fe-Si ratio [113, 135]. Compared to other metal/semiconductor interfaces, the Fe_3Si/GaAs(001) heterostructure exhibits a high thermal robustness and is stable up to 425 °C [38]. By fine-tuning of the growth parameters, i.e. growth temperature, Fe-Si flux and flux ratio, annealing temperature and time, Fe_3Si layers with high structural quality and long range order can be achieved [136–138]. Transmission electron microscope measurements showed that the Fe_3Si forms perfectly coherent, atomically flat interfaces with the GaAs(001) surface [134, 139, 140]. Grazing incidence x-ray diffraction experiments indicated different atomic configurations at the interface, even for samples grown at nominally equal growth conditions [133]. The same study revealed that

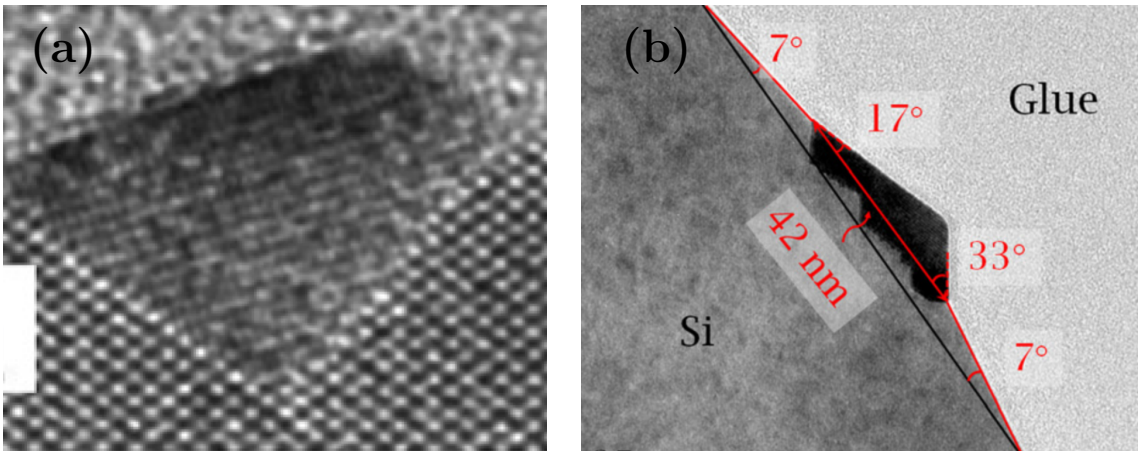

Figure 3.2: Transmission electron microscope images of endotaxial $FeSi_2$ nanowires grown on Si(110) taken from (a) [143] and (b) [144].

the Fe_3Si is terminated by mixed Fe-Si layers, as proposed by theory [141], which exhibit a certain degree of disorder due to exchange of atoms between Fe and Si sites. The growth of Fe_3Si on GaAs(001) starts with the formation of Fe_3Si islands with a height of 3 to 4 ML ($1\,\mathrm{ML} \equiv 0.28\,\mathrm{nm}$). At depositions of about 7 ML the onset of layer-by-layer growth is observed [134, 142].

Due to the variety of possible applications in Si-based nanoelectronics, the growth of $FeSi_2$ nanostructures on Si substrates has comprehensively been investigated during the last decades. In addition to the bulk Fe-Si phases described above, several metastable, strain-stabilized $FeSi_{1+x}$ phases with $0 \leq x \leq 1$ can be formed on different Si surfaces. These phases exhibit lattice parameters close to the value of Si and are stable at room temperature up to a critical size of the nanostructures. As a result, multiple Fe-Si phases can coexist on the very same Si surface. Which phases are actually formed depends on the choice of growth technique, the orientation of the Si surface, as well as the growth parameters, such as substrate temperature, growth rate, amount of deposited material, etc. Schematic phase diagrams have been reported for the growth on Si(111) [145–147] and Si(001) [148, 149], whereas the differentiation of phases seems to be more difficult for the Si(110) surface [150, 151]. Three main growth techniques are applied: solid phase epitaxy (SPE), reactive deposition epitaxy (RDE), and codeposition of Si and Fe. In SPE, the Si substrate is held at room temperature during the deposition of Fe and the Fe-Si compounds are formed by chemical reaction during a subsequent annealing cycle. RDE describes the deposition of Fe onto a heated Si substrate, which results in an immediate reaction of both components. Both techniques can be combined with the codeposition of Si and Fe, which offers the possibility to further tune the stoichiometry and to grow heterostructures with atomically flat interfaces. The orientation of the Si surface does not only influence the phase, but also determines the shape of the grown nanostructures. In the vast majority of reports the Si(111) and Si(001) surfaces are used for the growth of islands and films. On vicinal Si(111) surfaces with 4° miscut, elongated stripes of α-$FeSi_2$ can be grown at the step edges [122]. On Si(001), self-assembled α-$FeSi_2$ nanowires were grown by a combination of reac-

tive deposition epitaxy and nitride-mediated epitaxy [152]. The study reports that the nanowire formation is not induced by the well known mechanisms of anisotropic lattice mismatch or breaking of the surface symmetry by formation of twin-related interfaces. Instead, the lattice mismatch between the $FeSi_2$ nanostructure and the Si substrate is minimized by the formation of 1D structures, which are embedded into the substrate. This mechanism is known as endotaxy and occurs when the plane favorable for epitaxial growth is inclined with respect to the substrate surface [153, 154]. With this approach, uniaxially aligned nanostructures can be grown, where the orientation is determined by the substrate surface symmetry. Several studies on the growth of $FeSi_2$ on Si(110) also report the formation of uniaxially aligned endotaxial nanowires [36, 144, 151, 155]. In Figure 3.2 two exemplary transmission electron microscopy cross sections of endotaxial $FeSi_2$ nanowires grown on Si(110) are shown.

3.3. *Ab initio* lattice dynamics calculations of Fe_3Si, β-$FeSi_2$ and α-$FeSi_2$

For comparison with the experimental data obtained within this thesis, *ab initio* calculations of the lattice dynamics of Fe_3Si, β-$FeSi_2$ and α-$FeSi_2$ were conducted. All calculations presented in the following were performed by Dr. habil. Piekarz, Dr. Sternik, Dr. Sikora and Dr. Ptok in the group of Prof. Parlinski from the Institute of Nuclear Physics (PAS) in Krakow, Poland.

Figure 3.3 shows the results of *ab initio* lattice dynamics calculations performed by our collaboration partners for Fe_3Si, β-$FeSi_2$ and α-$FeSi_2$. In the left panels, labeled with (i), the phonon dispersion relations are displayed for each compound. The middle (ii) panels show the total phonon density of states and the element resolved Fe- and Si-partial subspectra. Since nuclear inelastic scattering is isotope-selective, the PDOS obtained with this method is the partial PDOS of the resonant isotope, i.e. for the samples investigated within this thesis the ^{57}Fe partial PDOS. Therefore, the panels (iii) on the right depict the Fe-partial PDOS, decomposed into its Fe[A,C] and Fe[B] subspectra in case of Fe_3Si and into its polarization-projected subspectra in case of β-$FeSi_2$ and α-$FeSi_2$. The differentiation between the respective subspectra is essential for the evaluation of the experimental data presented in the following chapters.

For Fe_3Si the number of atoms per unit cell is $s = 4$, resulting in 9 optical branches and 3 acoustic branches in the PDR [Fig. 3.3(a)(i)]. Generally, *fcc* lattices exhibit degenerated transverse acoustic modes along Γ-X and Γ-L, while along Γ-K all branches can be identified separately [49]. This can also be observed for the *fcc*-based Fe_3Si crystal structure. At energies between 20 and 40 meV several vibrational modes overlap, while above 40 meV three decoupled optical branches are present. A comparison with the Fe-partial and Si-partial PDOS presented in Figure 3.3(a)(ii) shows that these high energy modes predominantly originate from vibrations of the lighter Si atoms, while for energies below 40 meV the contribution of the Fe atoms is prevailing. In general the total PDOS of Fe_3Si is characterized by distinct peaks around 18 and 43 meV and several overlapping peaks between 22 and 38 meV.

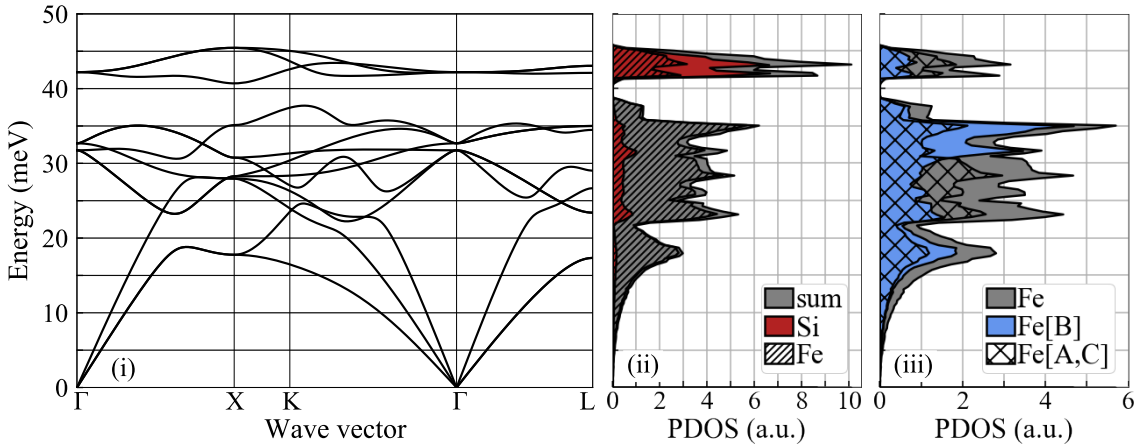

(a) Fe_3Si: *ab initio* calculated (i) PDR, (ii) Fe-partial, Si-partial, and total PDOS, and (iii) Fe-partial PDOS decomposed into its site specific Fe[B] and Fe[A,C] contributions.

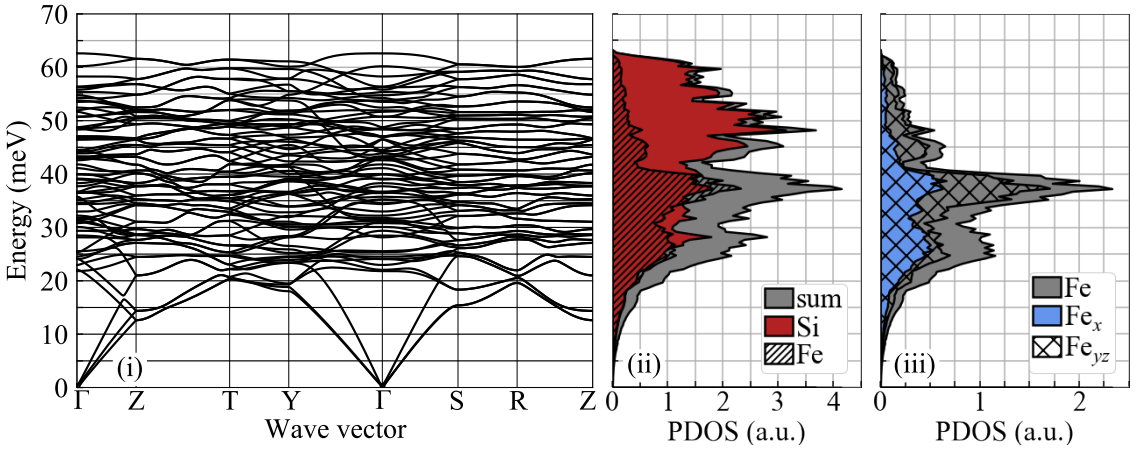

(b) β-$FeSi_2$: *ab initio* calculated (i) PDR, (ii) Fe-partial, Si-partial, and total PDOS, and (iii) Fe-partial, polarization-projected PDOS with x- and yz-polarized subspectra.

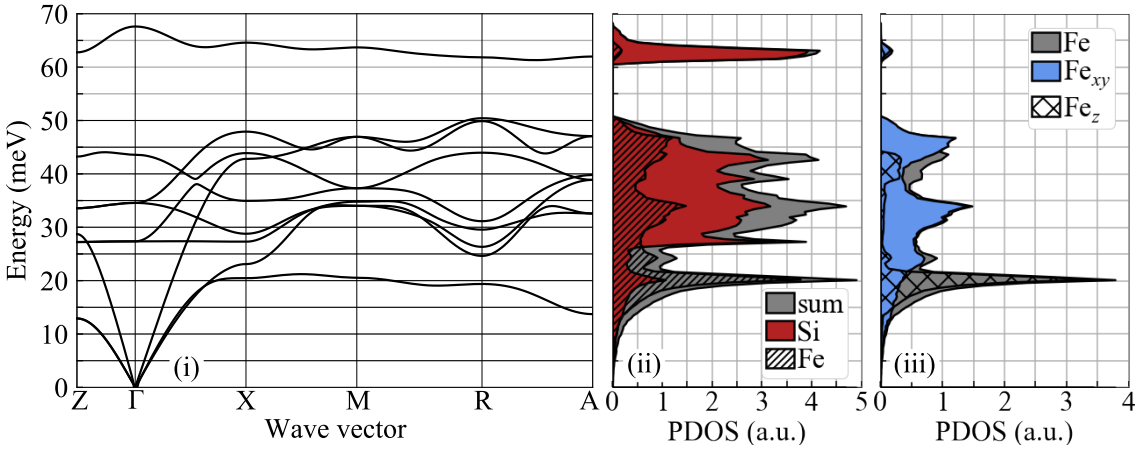

(c) α-$FeSi_2$: *ab initio* calculated (i) PDR, (ii) Fe-partial, Si-partial, and total PDOS, and (iii) Fe-partial, polarization-projected PDOS with xy- and z-polarized subspectra.

Figure 3.3: *Ab initio* calculated phonon dispersion relations and phonon density of states of Fe_3Si, β-$FeSi_2$ and α-$FeSi_2$.

The results are in good accordance with *ab initio* calculations done by Dennler and Hafner [156] and Liang et al. [157] and inelastic neutron scattering data obtained by Randl et al. [158]. A decomposition of the Fe-partial PDOS into its Fe[A,C] and Fe[B] subspectra [Fig. 3.3(a)(iii)] shows a stronger coupling of the Fe[A,C] atoms to the high-energy mode of the Si atoms at 43 meV. This is explained by the fact that the Fe[A,C] atoms have 4 Si atoms as nearest neighbors while the first shell of the Fe[B] atoms contains solely Fe atoms. The cubic structure of Fe_3Si implies that the PDOS projected along x, y and z direction are identical.

The large number of atoms per unit cell in case of β-$FeSi_2$ leads to a complex PDR with a total of 69 optical branches [Fig. 3.3(b)(i)]. This large number of overlapping vibrational modes results in rather broad frequency distribution of the normal modes as visible in the total PDOS in Figure 3.3(b)(ii). Above energies of 40 meV the PDOS is dominated by the contribution of the Si atoms, while below 40 meV both subspectra exhibit similar intensities. A comparison of these results with *ab initio* calculations performed by Liang et al. [157] and Tani et al. [159] shows a good agreement. The Fe-partial PDOS is also in good accordance with the results of a combined NIS and *ab initio* study of polycrystalline β-$FeSi_2$ by Walterfang et al. [160]. Due to the small differences in the lattice parameters along y and z direction of the orthorhombic unit cell of β-$FeSi_2$, the PDOS of vibrations polarized along these directions are very similar. Therefore, Figure 3.3(b)(iii) shows the Fe-partial PDOS decomposed into the combined contribution of yz-polarized vibrations and the contribution of the x-polarized vibrations. Both subspectra exhibit similar features that occur up to the cutoff energy of 62 meV with two broad peaks around 27 meV and around 37.5 meV. A differentiation between the two nonequivalent sites occupied by Fe atoms in the β-$FeSi_2$ unit cell is not required for the evaluation of the experimental data presented in the following.

The PDR of α-$FeSi_2$ exhibits 6 optical branches, 5 in the region between 25 to about 50 meV and one distinctly decoupled mode around 63 meV [Fig. 3.3(c)(i)]. The corresponding PDOS is characterized by pronounced peaks at 20 meV, mainly originating from an acoustic mode of Fe atoms along X-M, and 63 meV, mainly originating from the high-energy optical mode of Si atoms. In the intermediate region both elemental contributions overlap. Here it can be noted that in all three compounds the Si vibrations are prevailing in the high-energy part of the PDOS, since the lighter Si atoms vibrate with higher frequencies. In the tetragonal unit cell of α-$FeSi_2$ the x- and y-projected PDOS are identical and are merged in the Fe-partial, polarization-projected PDOS presented in Figure 3.3(c)(iii). A distinct decoupling of the vibrations with xy and z polarization is observed. The z-polarized phonon modes constitute a peak at 20 meV together with a minor plateau around 40 meV. The xy-polarized vibrations exhibit a broader spectrum, which dominates the Fe-partial PDOS at higher energies, i.e. between 25 and 50 meV with peaks at 33 and 45 meV. These results constitute the first determination of the complete lattice dynamics of α-$FeSi_2$ and are published in reference [101].

4. Lattice dynamics of the epitaxial, strain-free Fe_3Si/GaAs heterostructure

The physical properties of interfaces are of particular interest, since novel phenomena commonly emerge at the transition between two dissimilar materials. The interface regions are often the active parts in electronic devices, or to use the phrase Herbert Kroemer coined in his Nobel lecture [161]: "Often, it may be said that the interface is the device". While electronic and magnetic excitations have widely been investigated, the behavior of lattice excitations at interfaces remains poorly understood. For the elimination of undesired additional alterations of the lattice dynamics, e.g. induced by strain relaxation or disorder, a relaxed interface structure with an excellent structural quality is required. The strain-free Fe_3Si/GaAs heterostructure constitutes an ideal model system for such investigations, since the high degree of crystalline perfection of the GaAs substrate is maintained throughout the interface area and the Fe_3Si crystal. Nuclear inelastic scattering provides the exceptional sensitivity to measure samples containing a single atomic layer of a Mössbauer-active isotope, which is a prerequisite for the selective determination of the lattice dynamics of the atomic layers directly adjacent to the interface.

For that purpose, Fe_3Si thin films with thicknesses ranging from bulk-like samples to a few monolayers were prepared by molecular-beam epitaxy. In the following, the preparation and characterization of these samples is described. The Fe-partial phonon density of states, obtained from nuclear inelastic scattering, is presented and compared with *ab initio* calculations. Furthermore, the vibrational anomalies observed upon reduction of the film thickness as well as the alterations of the thermodynamic and elastic properties are discussed.

4.1. Sample preparation and characterization

The samples were prepared in collaboration with the Paul-Drude-Institut für Festkörperelektronik, using the MBE system shown in Figure 2.4. GaAs(001) substrates were deoxidized at 580 °C in an As atmosphere with P=10^{-5} Pa, in a UHV chamber dedicated to the growth of III-V semiconductors. At the same temperature, the GaAs(001) substrates were overgrown with a 350 nm thick GaAs buffer layer, resulting in an As-rich c(4×4) reconstructed GaAs(001) surface, as evidenced by RHEED [Fig. 4.1(a), 4.1(f)]. Subsequently, the substrates were transferred under UHV conditions to a separate, As-free metal growth chamber with a base pressure of 10^{-8} Pa. The Fe_3Si layers were grown by coevaporation of Fe and Si, using iron

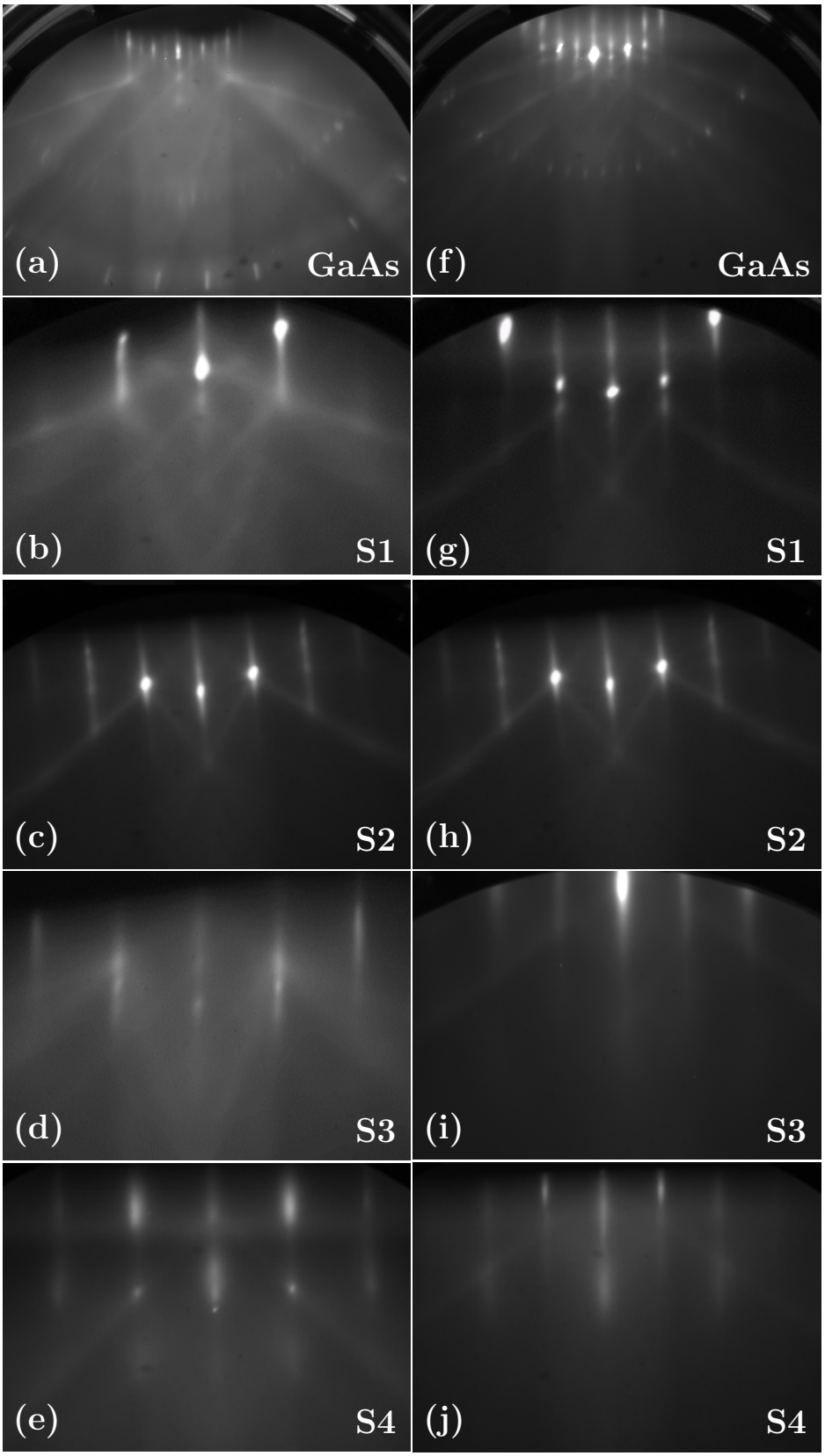

Figure 4.1: RHEED patterns measured with E = 20 keV along the GaAs/Fe_3Si [010] (a)-(e) and [110] (f)-(j) azimuth. (a) and (f) show the diffraction pattern obtained for the GaAs(001) surface after growth of the buffer layer, (b)-(e) and (g)-(j) the pattern obtained for the Fe_3Si(001) surface of the indicated samples.

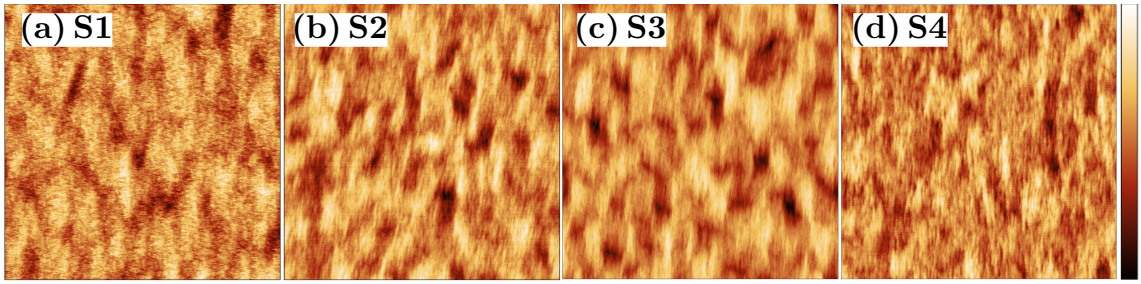

Figure 4.2: 10×10 μm AFM images of the indicated samples with height scale (a) 0 - 6 nm, (b) 0 - 4 nm, (c) 0 - 6 nm, and (d) 0 - 4 nm. The color scale depicted on the right applies for all images.

enriched to 96 % in the Mössbauer active isotope ^{57}Fe. During deposition, the GaAs substrate was held at a growth temperature of $T_G = 200\,°C$, following a well established procedure for growth of high quality $Fe_3Si(001)/GaAs(001)$ heterostructures [113]. In the following, four samples with nominal Fe_3Si layer thicknesses of 36 monolayers (ML) (S1), 8 ML (S2), 6 ML (S3) and 3 ML (S4) are discussed. One ML corresponds to a thickness of 0.28 nm and consists of two atomic layers, one pure Fe layer and one mixed Fe/Si layer [Fig. 3.1(a)]. All measurements described herein are conducted at room temperature. The crystallographic structure of the Fe_3Si surfaces was investigated by RHEED measurements. The images obtained along $Fe_3Si[010]$ and $Fe_3Si[110]$ are presented in Figure 4.1(b) - 4.1(e) and 4.1(g) - 4.1(j), respectively. For all samples streaky diffraction patterns are observed, indicating the formation of crystalline and smooth Fe_3Si surfaces. By comparison of the inter-streak distances before and after growth, the reported epitaxial relation of $Fe_3Si(001)||GaAs(001)$ with $Fe_3Si[100]||GaAs[100]$ is confirmed. All samples were capped with 4 nm of amorphous Ge deposited at 150 °C, in order to prevent oxidation of the Fe_3Si layer and to eliminate surface vibrational modes. At this growth temperature interface reactions and intermixing of the Ge and Fe_3Si do not take place [137].

After the capping, the surface morphology was characterized by *ex situ* AFM

Table 4.1: Thickness and R_{rms} values of the Fe_3Si and Ge layers of S1 - S4 obtained from the XRR data [Fig. 4.3(c)] analysis and AFM The nominal Fe_3Si and Ge layer thickness is given for comparison.

	layer	thickness (nm)		R_{rms} (nm)	
		nominal	simulation	AFM	simulation
S1	Fe_3Si	10.1	9.4		0.3
	Ge	4.0	4.0	0.8	0.3
S2	Fe_3Si	2.3	2.3		0.5
	Ge	4.0	3.7	0.5	0.6
S3	Fe_3Si	1.7	1.7		0.5
	Ge	4.0	3.6	0.8	1.0
S4	Fe_3Si	0.85	0.84		1.0
	Ge	4.0	4.0	0.4	0.7

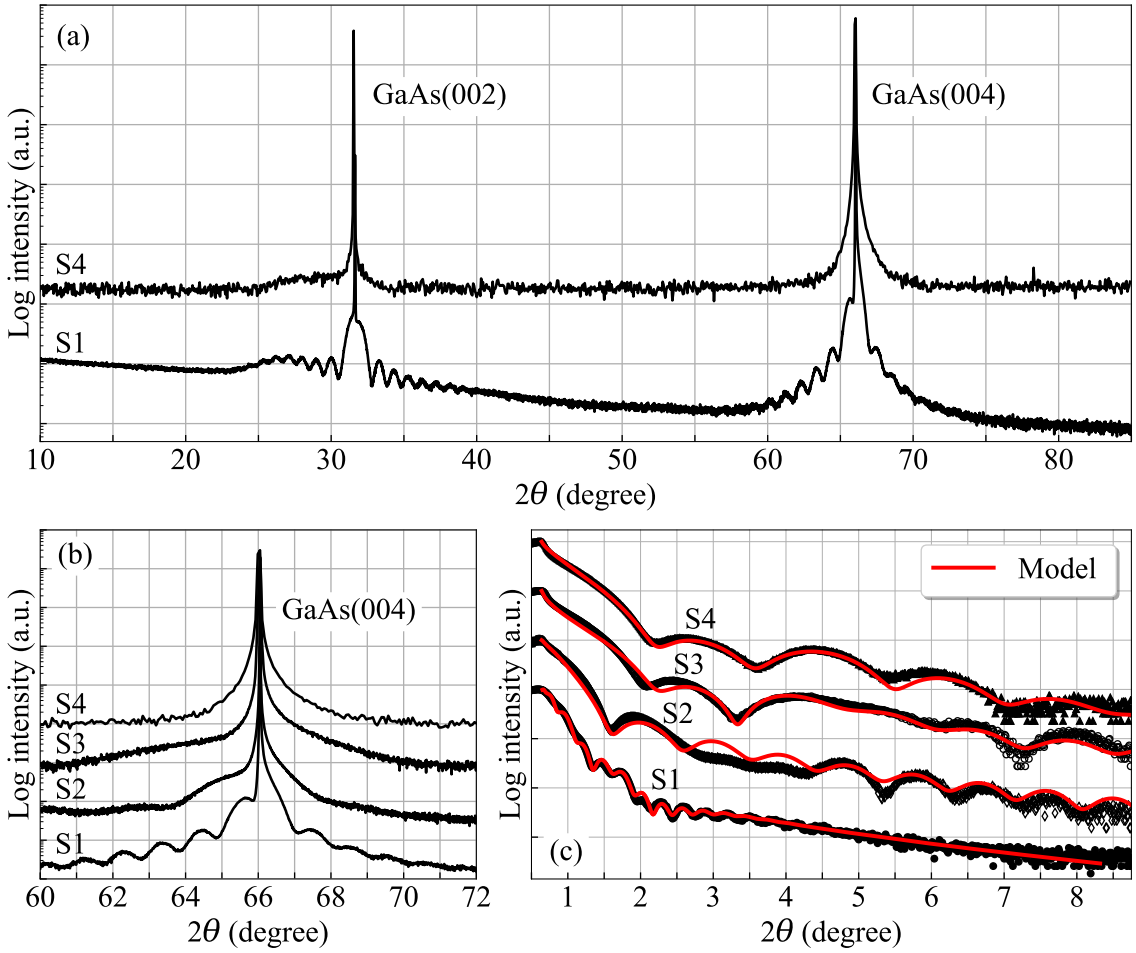

Figure 4.3: (a) Wide range θ-2θ XRD scan of S1 and S4. (b) Close-up of the θ-2θ XRD scans around the GaAs(004) reflection of S1 - S4. (c) Experimental XRR (symbols) and corresponding simulated profiles (solid lines) of S1 - S4. All measurements were done using the Cu K_α line.

measurements. In Figure 4.2 generic AFM images of S1 - S4 are presented, in Table 4.1 the corresponding root-mean-square roughness (R_{rms}) values are given. For all samples smooth surfaces with R_{rms} values below 1 nm are observed. The same applies for the surface morphology of a typical GaAs(001) surface after deposition of the buffer layer.

The crystalline structure and layer properties of the samples was investigated by *ex situ* x-ray diffraction (XRD) and x-ray reflectivity (XRR), respectively, with a X-Pert PRO MRD system using Cu $K_{\alpha 1}$ radiation. In Figure 4.3(a) θ-2θ overview XRD scans of S1 and S4 are shown. Both scans are characterized by the GaAs(002) and (004) substrate diffraction peaks. For S1 the broader Fe_3Si(002) and (004) diffraction peaks of the 36 ML Fe_3Si layer are superimposed onto the sharp diffraction peaks of the GaAs substrate, which is evidence of a perfect stoichiometry of the Fe_3Si layer [113]. No additional peaks are observed, confirming the phase purity of the samples [162]. Several oscillations of thickness fringes are observed for both diffraction peaks, which indicate a high quality of the interfaces. The very low layer

thickness of S4 prevents a detection of the Fe_3Si crystal structure by the used XRD setup. The detailed scans around GaAs(004) of S1 - S4 presented in Figure 4.3(b) confirm the epitaxial nature of the Fe_3Si films. For S2 a broad peak originating from the 8 ML thick Fe_3Si layer and one faint oscillation of the thickness fringes can be seen, while for the 6 ML thick Fe_3Si layer of S3 a broad shoulder is visible. The XRR measurements presented in Figure 4.3(c) show distinct oscillations for all samples, confirming the high layer and interface quality. Further insight into the layer properties was gained by simulation of the experimental XRR curves using the *GenX* software package [163]. The values obtained for the Fe_3Si and Ge layer thickness and interface roughness are presented in Table 4.1. For comparison, the respective nominal layer thickness in nanometers and the R_{rms} values of the Ge layer, determined from the AFM measurements, are given. In general, a good agreement is observed between simulation and experiment. The results for the Fe_3Si and Ge layer thickness are in good accordance with the nominal values. The relatively high R_{rms} value obtained for the Fe_3Si layer in S4, which is above the nominal layer thickness, indicates the formation of islands. On the contrary, the R_{rms} values of the Fe_3Si layer are significantly reduced for S1, S2 and S3 and the growth of continuous films is indicated.

The microscopic structure of the heterostructures was investigated by a high resolution transmission electron microscopy (TEM) study. The measurements were performed by Dr. Jenichen at the Paul-Drude-Institut für Festkörperelektronik. The samples were prepared for the measurements by mechanical lapping and polishing, followed by argon ion milling. Images were acquired with a JEOL 3010 TEM operating at 300 kV and a JEOL 2100F TEM operating at 200 kV. The results obtained for S1, S3 and S4 are presented in Figure 4.4, in Figure 4.5 magnified high resolution TEM images of S3 and S4 are depicted. For visual reference, yellow lines indicate the Fe_3Si/GaAs, blue lines the Fe_3Si/Ge, and green lines the Ge/glue interface. For S1 the nominal Fe_3Si layer thickness of 36 ML is confirmed by the TEM measurements [Fig. 4.4(a), 4.4(b)]. The epitaxial film exhibits smooth interfaces with a high degree of crystalline perfection at both, the Ge/Fe_3Si and the Fe_3Si/GaAs interface. For S3 [Fig. 4.4(c), 4.4(d)] a continuous film with islands on top is observed. In the TEM images of S4 [Fig. 4.4(e), 4.4(f)] the crystal structure of the GaAs and the Fe_3Si is resolved and a smooth epitaxial transition is observed at the interface. The reduction of the nominal film thickness to 3 ML in S4 leads to the formation of flat Fe_3Si islands that only partially cover the GaAs surface. In the magnified TEM images of S3 and S4 [Fig. 4.5(a), 4.5(b)] the Fe_3Si(001) crystal planes are resolved. The thickness of the continuous film observed in Figure 4.5(a) for S3 is 4 ML. With an island on top, the total thickness of the Fe_3Si film amounts to 7 ML. The islands present in S4 exhibit a height of 4 ML and a width of about 20 ML. This is in accordance with [134] and [142], where initially the Volmer-Weber type growth of 3 ML high islands is reported, which coalescence to a continuous film upon deposition of about 7 ML of Fe_3Si.

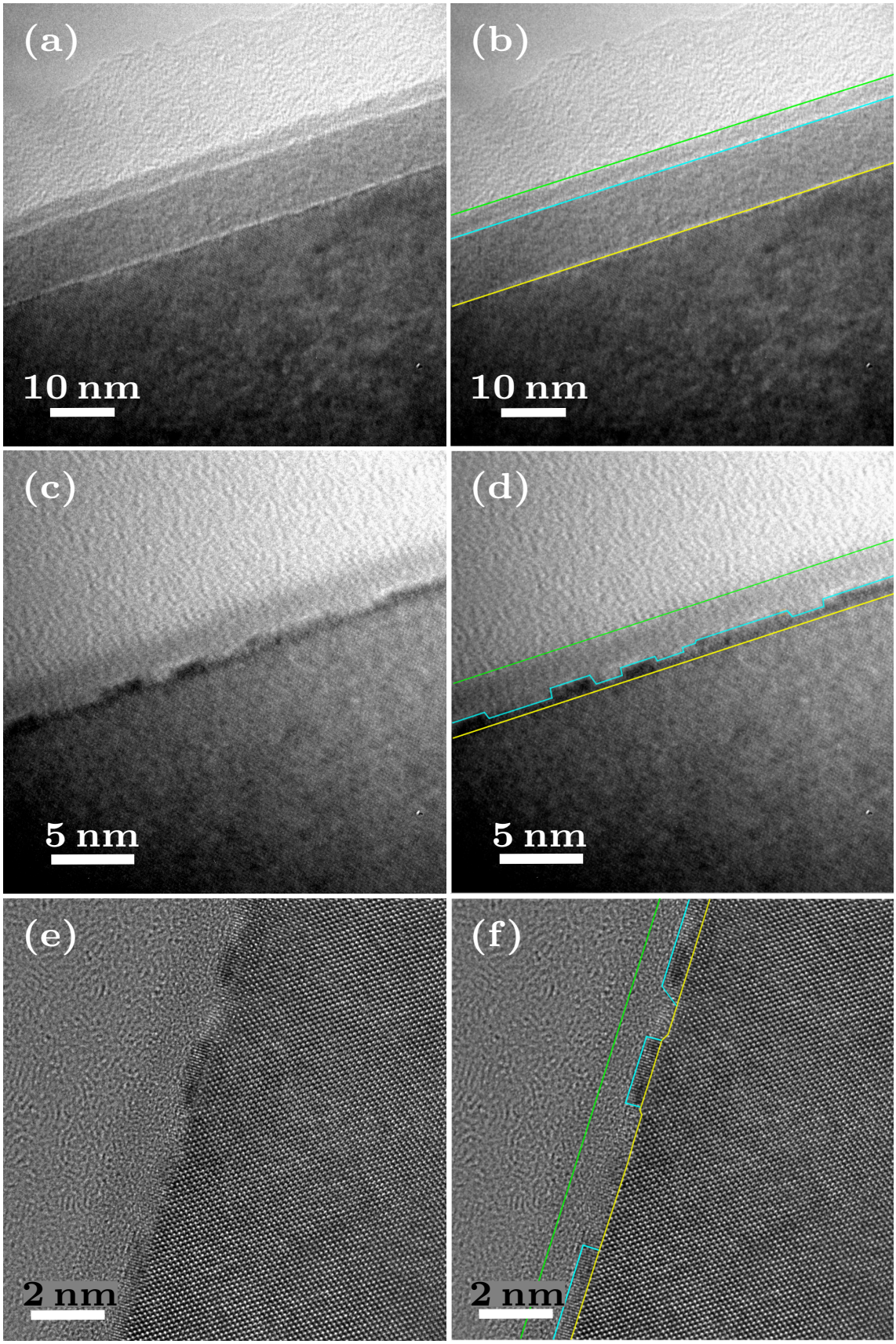

Figure 4.4: High resolution transmission electron microscope images of S1 (a,b), S3 (c,d) and S4 (e,f). In the right column the yellow lines indicate the Fe_3Si/GaAs, the blue lines the Fe_3Si/Ge and the green lines the Ge/glue interface.

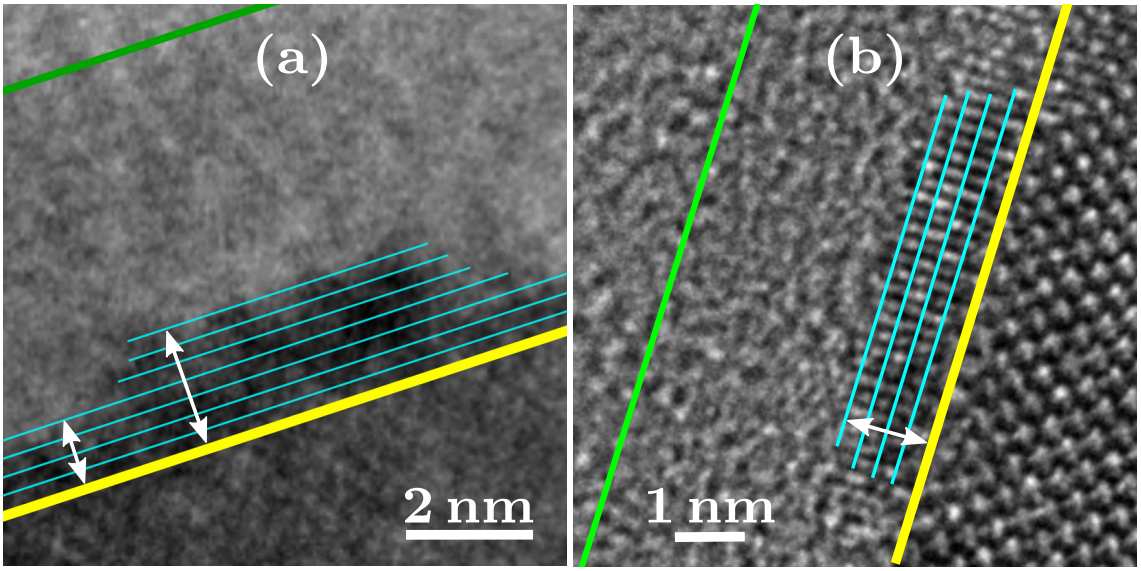

Figure 4.5: Magnified high resolution TEM images of S3 (a) and S4 (b). Yellow lines indicate the Fe_3Si/GaAs interface and green lines the Ge/glue interface. The lattice planes of the Fe_3Si monolayers, consisting of two atomic layers, are indicated with blue lines.

4.2. Lattice dynamics

The Fe-partial phonon density of states of S1 - S4 was determined by nuclear inelastic scattering experiments, performed at the Dynamics Beamline P01 at PETRA III [92]. The samples were measured at grazing incidence geometry (incidence angle $< 0.2°$) with an energy resolution of 0.9 meV and the wave vector of the x-ray beam being parallel to Fe_3Si[010]. In Figure 4.6 the obtained results are presented. The PDOS of the 36 ML Fe_3Si of S1 is characterized by peaks at 17, 34, and 41.5 meV and overlapping modes between 21.5 and 28 meV. The experimental results of S1 are compared with the *ab initio* calculated Fe-partial PDOS of bulk Fe_3Si [Fig. 3.3(a)]. To account for the phonon damping inherently present in real crystals, the *ab initio* calculated PDOS is convoluted with the damped harmonic oscillator function, as described in section 2.1.3. A remarkable agreement between experiment and theory is observed for a quality factor of $Q_{bulk} = 21 \pm 1$. The given uncertainty of Q is an upper bound. Additionally, the *ab initio* calculated PDOS was convoluted with a Gaussian function with FWHM = 1.9 meV, which is by a factor of 2 higher than the experimental resolution. The result is depicted with a dashed black line,

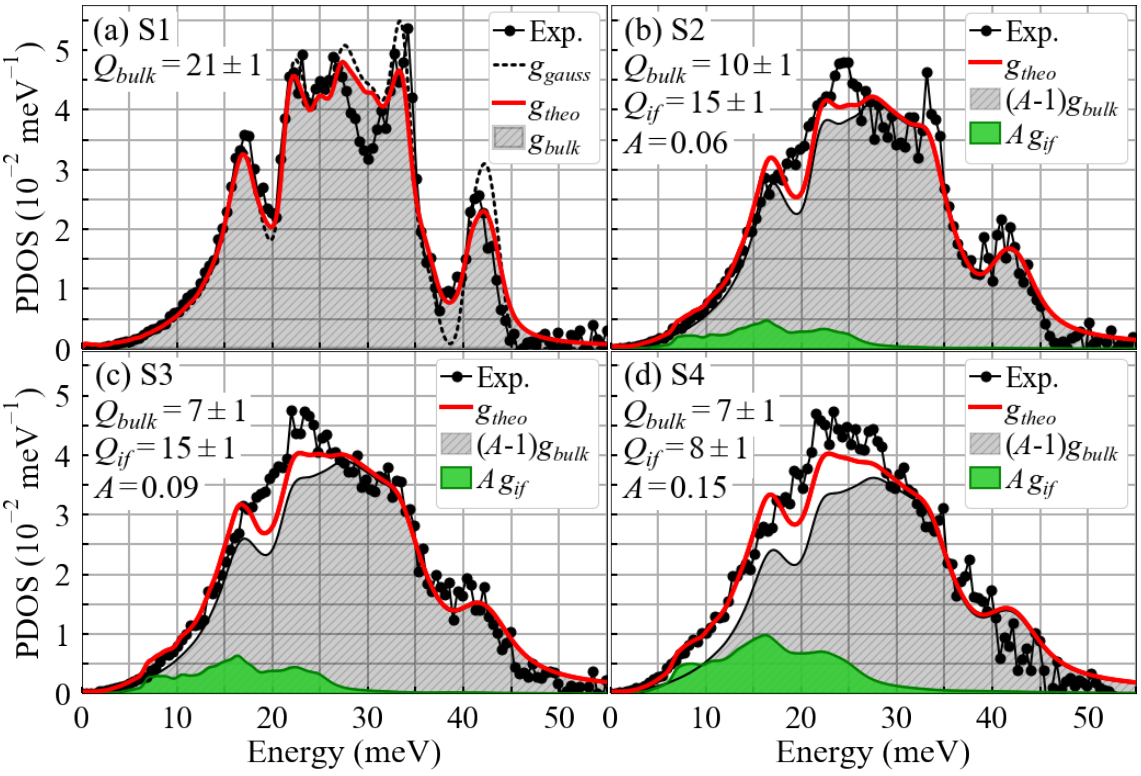

Figure 4.6: Fe-partial PDOS of the indicated samples obtained along Fe_3Si[010], compared with the respective results for $g_{theo}(E)$. The fit results of S2 - S4 are decomposed into their weighted bulk $[(A-1)\,g_{bulk}]$ and interface $(A\,g_{if})$ contributions, the PDOS of S1 was fitted using only g_{bulk}. On the upper left the results obtained for the respective quality factors and the relative weight of the interface contribution are given. In (a) the dashed line marks the convolution of the *ab initio* calculated PDOS with a Gauss function with FWHM = 1.9 meV.

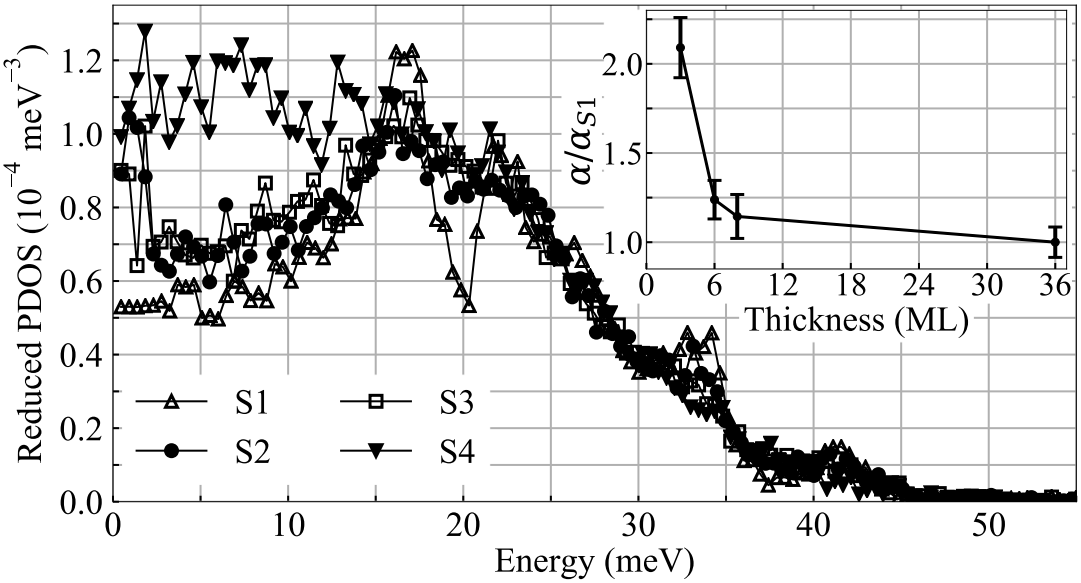

Figure 4.7: Reduced PDOS $[g(E)/E^2]$ of S1 - S4. The inset shows the coefficient α obtained from $g(e) = \alpha E^2$ in the range from 4 - 8 meV as a function of the nominal Fe_3Si film thickness given in monolayers, normalized to α_{S1}.

denoted with g_{gauss} in Figure 4.6(a). With this approach the height of the peak at 17 meV is underestimated, while the high-energy peak at 41.5 meV is significantly overestimated. These deviations show that a correct modeling of the experimental PDOS with *ab initio* results can only be achieved under consideration of energy-dependent phonon damping, which is included by the DHO function.

The gradual reduction of the Fe_3Si layer thickness from S1 to S4 is accompanied by a gradual damping of the PDOS features and an enhancement of states at low and high energies. For S4 an almost featureless vibrational spectrum is observed. In the reduced PDOS $g(E)/E^2$, plotted in Figure 4.7, the enhancement of low-energy states upon reduction of the Fe_3Si film thickness from S1 to S4 is evident. The low-energy part of all samples can be described by the Debye model for a three-dimensional crystal $g(E) = \alpha E^2$. A deviation from the quadratic behavior is not observed, as it is reported for low-dimensional nanoparticles (e.g. [164]). It has theoretically been demonstrated that these deviations originate from low-coordinated surface atoms [165], which are not present in the epitaxial and capped nanostructures investigated here. For quantification of the low-energy enhancement, the α values of S1 - S4 were determined by fitting of the reduced PDOS in the range of 4 - 8 meV. The PDOS below 4 meV is excluded, because of the subtraction of the elastic peak (S_0 in Figure 2.10) from the nuclear inelastic scattering spectrum. The results, normalized to the value obtained for S1, are plotted as a function of the film thickness in the inset in Figure 4.7. The plot shows that the number of low-energy states is enhanced by a factor of 2.1 in S4 compared to S1. For the native Fe(110) surface [31], ultra-thin Fe(110) films deposited on W(110) [29] and Fe nanoparticles [164] a similar increase of the number of phonon states below ≈10 meV was attributed to surface-specific modes, tensile epitaxial strain and structural disorder at grain boundaries, respectively. However, these effects are excluded in the Ge-covered,

lattice-matched and single-crystalline Fe_3Si/GaAs heterostructure investigated here and the vibrational anomalies are expected to arise from interface-specific phonon states.

In order to test this hypothesis, the lattice dynamics of the $Fe_3Si(001)$/GaAs(001) heterostructure was determined by first-principles calculations. The results presented in Figure 4.8 are based on the work of Dr. Piekarz and Dr. Sternik from the Institute of Nuclear Physics in Krakow. The graphs represent the *ab initio* calculated, layer-specific Fe-, Si-, Ga-, and As-partial PDOS projected along (xy) and across (z) the Fe_3Si/GaAs interface. For comparison, the PDOS of the respective atom in the same kind of layer in bulk Fe_3Si or GaAs is shown as a shaded area. The calculations were performed assuming a Fe_3Si/GaAs heterostructure consisting of 12 atomic layers forming a $\sqrt{2a} \times \sqrt{2a} \times c$ supercell with 76 atoms and periodic boundary conditions. The supercell is depicted in Figure 4.9. The colors and atomic labels correspond to the PDOS shown in Figure 4.8.

In the atomic layers relatively far away from the interface, i.e. Fe4, Fe3/Si3, and As3, only minor deviations from the bulk PDOS are observed along and across the interface. In the Fe2 layer a significant enhancement of low-energy states is observed for the z-polarized PDOS, whereas in the Ga1 layer the low-energy enhancement is particularly strong for xy-polarized vibrations. In the layers directly adjacent to the interface, Fe1/Si1 and As1, the high-energy peaks present in the bulk crystal are suppressed along both polarizations. The xy-polarized PDOS of the Fe1 atoms shows remarkable differences to its bulk counterpart, mainly a strong enhancement of the low-energy states with new vibrational modes occurring between 6 - 18 meV and between 20 - 25 meV. The PDOS of the Si1 atoms still exhibits states at higher energies, but also shows a significant shift of the overall PDOS to lower energies. Furthermore, the initially isotropic vibrational spectra of the cubic systems exhibit a pronounced anisotropy of vibrations with xy- and z-polarization.

Since the experiments were conducted at grazing-incidence geometry, i.e. with the wave vector of the x-ray beam oriented parallel to the interface, Figure 4.6 depicts the Fe-partial xy-polarized PDOS of S1 - S4 (detailed discussion in section 2.2.3). Consequently, the *ab initio* calculated Fe-partial xy-polarized PDOS was used for the comparison between theory and experiment. The experimental PDOS of S2, S3 and S4, were modeled with the following function:

$$g_{theo}(E) = A\, g_{if}(E, Q_{if}) + (1 - A)\, g_{bulk}(E, Q_{bulk}) \tag{4.1}$$

where $g_{if}(E, Q_{if})$ and $g_{bulk}(E, Q_{bulk})$ are the *ab initio* calculated xy-projected Fe-partial PDOS of the interface and bulk Fe_3Si, respectively, convoluted with the DHO function with quality factors Q_{if} and Q_{bulk}, while A stands for the relative interface atomic fraction. The experimental PDOS were fitted with Eq. 4.1 using the least-squares method with Q_{bulk}, Q_{if}, and A being variable parameters. The best agreement between theory and experiment was achieved when only the PDOS of the first interface layer is considered, therefore in the following g_{if} is equal to the PDOS of Fe1 xy in Figure 4.8(d). In Figure 4.6(b) - 4.6(d) the results obtained for g_{theo} are presented together with the bulk and interface subspectra. Furthermore, the obtained Q_{bulk}, Q_{if}, and A values are given. In general, the experimental results are very well reproduced by g_{theo}. In particular, the step-like increase of the exper-

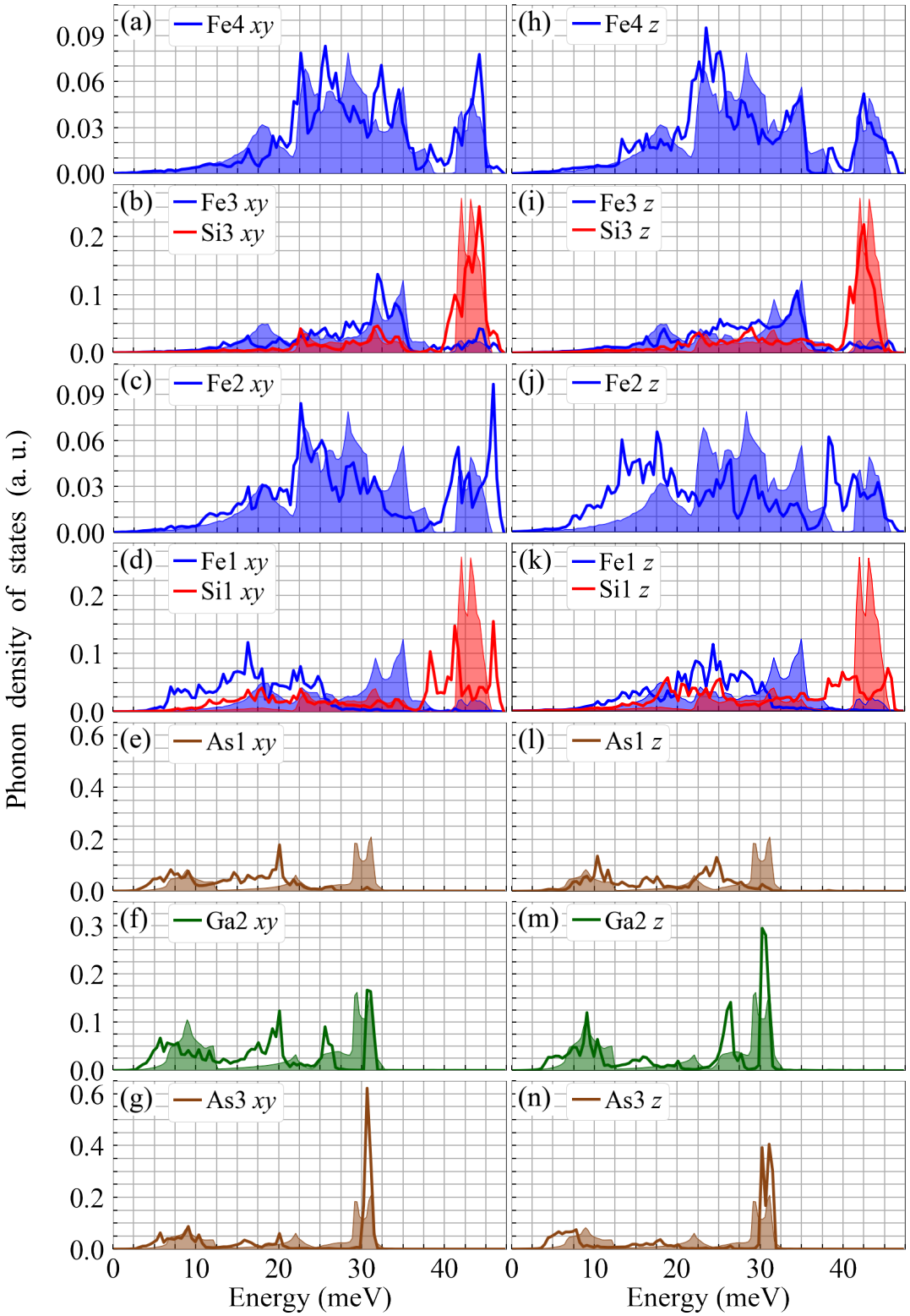

Figure 4.8: *Ab initio* calculated, layer-specific Fe-, Si-, As-, and Ga-partial PDOS projected along [(a-g)] and across [(h-n)] the interface (solid lines), compared with the corresponding spectra in bulk material (shaded area). The colors and legend entries designate the corresponding type of atom and atomic layer, which are depicted in Figure 4.9.

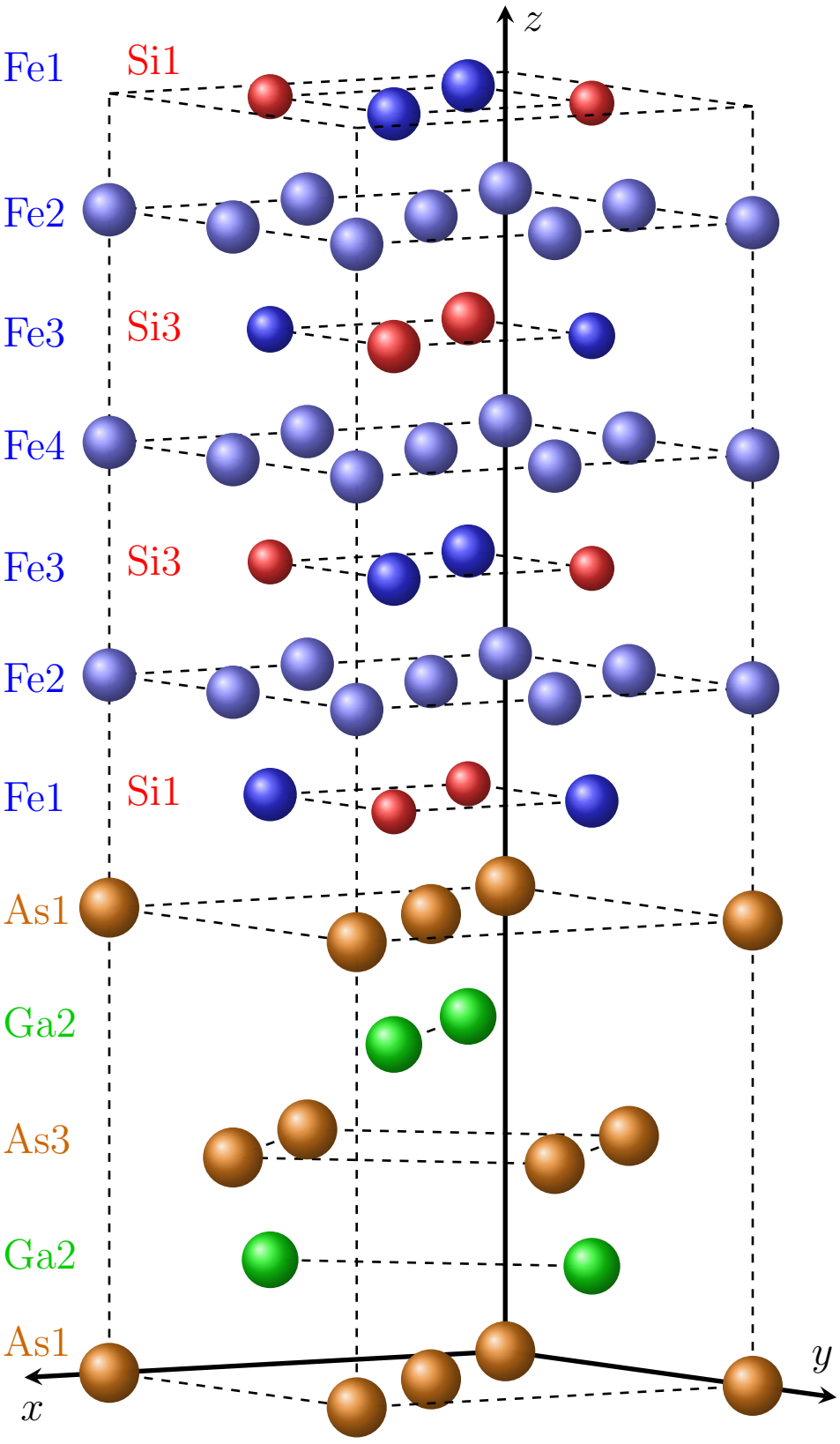

Figure 4.9: Atomic configuration of the $Fe_3Si(001)/GaAs(001)$ supercell used to calculate the interface lattice dynamics presented in Figure 4.8.

imental PDOS of S4 at 7 meV, which is also visible in the reduced PDOS, clearly originates from the peak at 7 meV in the Fe1 *xy* PDOS [Fig. 4.8(d)]. Based on the results of the TEM study presented above, it can be assumed that the 2D islands of S4 consist of 6 to 8 atomic layers, which implies a 1/7 (0.14) contribution of the first interface layer Fe1. For S3 the average thickness of the Fe_3Si layer is estimated to be 12 atomic layers, i.e. a relative Fe1 contribution of 1/12 (0.08) is expected, while for S2 the Fe_3Si film consists of 16 atomic layers, leading to a relative Fe1 contribution of 1/16 (0.06). These values are in excellent agreement with the relative interface atomic fractions A obtained by the fitting procedure. For all three samples deviations between the experimental PDOS and g_{theo} are observed in the range 17 – 27 meV. The reason could be additional interface-specific modes present at the Ge/Fe_3Si interface, which is not included in the model. Indeed, the same type of calculations as presented in Figure 4.8 have also been conducted for the epitaxial Ge/Fe_3Si interface. They reveal a similar shift of the PDOS to lower energies, indicating that the observed effect generally occurs in metal/semiconductor heterostructures. But with the chosen *ab initio* approach it is not possible to model the amorphous/crystalline Ge/Fe_3Si interface present in the samples and therefore a definite conclusions on the effect of this interface on the experimental PDOS cannot be drawn.

The quality factors obtained from the least-squares optimization discussed above are inversely proportional to the strength of the damping. The results show that Q_{bulk} of S2 is significantly increased compared to the equal values obtained for S3 and S4. To understand this trend, it has to be considered that in S3 and S4 the value of Q_{bulk} is strongly influenced by the Ge/Fe_3Si interface. The TEM study showed that solely flat islands are formed in case of S4, while flat islands on top of a thin continuous layer are observed for S3. On the contrary, for S2 we can assume a continuous Fe_3Si film [142] with a significantly smaller Fe_3Si/Ge interface area. Consequently, the damping effects arising from the disorder present at the amorphous/crystalline interface are reduced and the obtained Q_{bulk} is increased in S2 compared to S3 and S4. On the other hand, S2 and S3 exhibit the same Q_{if} values, which are almost twice as large as for S4. Q_{if} is determined by the properties of the Fe_3Si/GaAs interface, which is continuous in case of S2 and S3, whereas for the islands in S4 the periodicity is broken along the interface. Thus, phonons propagating along the interface experience a stronger damping in S4 and Q_{if} is reduced compared to S2 and S3.

4.3. Thermodynamic and elastic properties

In Table 4.2 the thermodynamic and elastic properties obtained from the Fe-partial PDOS of S1 - S4 are compared with the values determined from the respective $g_{theo}(E)$ and the *xy*- and *z*-polarized PDOS of the first interface layer Fe1. The experimental values show a decrease of 9 % of the mean force constant in the smallest Fe_3Si nanostructures of S4 compared to the bulk-like film of S1. The softening of the lattice is also reflected in the mean square displacement and the vibrational entropy, which are increased by 36 % and 6 %, respectively, in S4 compared to S1.

Table 4.2: Experimental (exp.) and theoretical (theo.) values of the Fe-partial mean force constant F, mean square displacement $\langle x^2 \rangle$ and vibrational entropy S_V of S1 - S4 and the xy- and z-projected values for the Fe1 layer of the Fe_3Si/GaAs interface. The coefficient α derived from the low-energy part of the PDOS [$g(E) = \alpha E^2$] and the sound velocity v_S are also given.

		F	$\langle x^2 \rangle$	S_V	α	v_S
		(N/m)	$(10^{-2}$ Å$^2)$	$(k_B/at.)$	$(10^{-5} meV^{-3})$	(m/s)
S1/bulk	exp.	175(3)	1.4(2)	3.19(2)	5.8(3)	3848(231)
	theo.	176	1.8	3.15	-	-
S2	exp.	173(3)	1.5(2)	3.22(2)	6.6(6)	3679(328)
	theo.	170	1.9	3.23	-	-
S3	exp.	172(4)	1.6(2)	3.24(2)	7.2(5)	3584(226)
	theo.	167	2.0	3.27	-	-
S4	exp.	159(5)	1.9(2)	3.38(2)	12.1(7)	3009(161)
	theo.	161	2.1	3.35	-	-
Fe1	xy	74	3.9	4.47	-	
	z	121	2.0	3.62	-	

Comparison with the values obtained from the respective $g_{theo}(E)$ shows a very good agreement, confirming that the first-principles theory reliably explains the observed interface effects. The lattice softening and vibrational anisotropy induced on the cubic Fe_3Si crystal by the broken translational symmetry at the interface is clearly reflected in the thermodynamic properties of the Fe1 layer. The reduction of the mean force constant amounts to 58 % along the interface, while across the interface it is reduced by 31 %, compared to the bulk value. The mean square displacement increases by a factor of 2.2 in the xy-projection and only by 1.1 in the z-projection and S_V is increased by 42 % from the bulk value along the interface, whereas across the interface the relative increase is 15 %.

Furthermore, the absolute α values, which are plotted as relative values in Figure 4.7, are given in Table 4.2. The corresponding errors are equal to one standard deviation obtained by the least squares optimization. Using Equation (2.41), they can be used for calculation of the velocity of sound v_S in the Fe_3Si crystal. In addition, the corresponding theoretical value was determined from the slope of the acoustic branches of the phonon dispersions to be v_S=4823 m/s. The experimental values are significantly smaller, since in a real system the propagation of sound waves is decelerated due to phonon scattering by crystal defects, which is not considered in the *ab initio* calculations performed under assumption of a perfect lattice. The increase of α by a factor of 2.1 in S4 compared to S1 is also reflected in the corresponding v_S, which is reduced by 25 % in S4 compared to S1. This behavior can be attributed to the enhanced phonon scattering in the smaller nanostructures, which is also evidenced from the evolution of the quality factors.

4.4. Conclusions

In this study, the lattice dynamics of the epitaxial, strain-free Fe_3Si/GaAs heterostructure was investigated. For this purpose, Fe_3Si layers with nominal thicknesses of 36, 8, 6 and 3 monolayers were epitaxially grown on atomically flat GaAs(001) surfaces. All samples were capped with 4 nm of amorphous Ge to prevent oxidation of the Fe_3Si layer and to eliminate surface vibrational modes. The surface morphology as well as the crystal and interface structure was investigated by AFM, XRD, XRR and TEM. The results showed the formation of epitaxial Fe_3Si/GaAs heterostructures with a high degree of crystalline perfection and sharp interfaces. Deposition of 36 monolayers of Fe_3Si leads to the formation of a continuous film, the same can be assumed for the 8 monolayer sample. Upon deposition of 6 monolayers a continuous film with islands on top is formed and the deposition of 3 monolayers results in the formation of 2D Fe_3Si islands.

The Fe-partial PDOS of Fe_3Si, projected along [010], was obtained by nuclear inelastic scattering. The results reveal up to a two-fold enhancement of the low-energy states compared to the bulk material, as well as a distinct damping of the peaks for a layer thickness of 8 monolayers and below. *Ab initio* calculations showed that novel, interface-specific vibrational modes emerge at the epitaxial Fe_3Si/GaAs transition. The deviations from the PDOS of the bulk material are mostly localized in the first atomic layer directly adjacent to the interface and are characterized by a strong shift of phonon states to lower energies. Furthermore, the broken translational symmetry induces a pronounced anisotropy on vibrations along and across the interface. The experimental results are comprehensively understood by modeling the obtained PDOS with a combination of the *ab initio* calculated interface-specific and bulk PDOS. The relative fractions of both contributions obtained by least-squares fits are in excellent accordance with the results from the TEM study. The evolution of the interface- and bulk-specific quality factors was fully explained by the different Fe_3Si layer morphologies. Furthermore, the thermodynamic and elastic properties revealed a significant softening of the Fe_3Si layer in the smallest structures compared to the bulk-like film, i.e. a 9 % reduction of the mean force constant, a 25 % reduction of the velocity of sound and an increase of the mean square displacement by 36 %.

The results reveal the existence of interface-specific vibrational modes in epitaxial, strain-free interfaces, which induce significant alterations on the thermodynamic and elastic properties compared to their bulk counterparts. This constitutes a major step forward in the controlled modification of the lattice dynamics in two-dimensional systems.

5. Lattice dynamics of metastable α-phase $FeSi_2$ nanostructures

Despite its unique properties, hitherto only scarce theoretical data on particular thermodynamic properties of the high-temperature phase α-$FeSi_2$ is available in literature [151, 166]. The plausible reason is that data collection above the transition temperature of 950 °C is very ambitious, since the vibrational spectrum is dominated by multiphonon excitations at such high temperatures. A path to circumvent this limitation was shown by several studies that reported the growth of metastable metallic Fe-Si phases on the Si(111) surface, i.e. s-$FeSi_{1+x}$ [167] and γ-$FeSi_2$ [168–170], which exhibit a cubic structure and lattice parameters close to the value of silicon. Up to a critical size, the formation of these lattice-matched phases is energetically favorable over the formation of strained β-$FeSi_2$. Applying the same mechanism, the tetragonal α-$FeSi_2$ can be stabilized at room temperature in epitaxial nanostructures by deposition of a few Fe monolayers on the Si surface [115, 121, 171–174]. In conjunction with the high sensitivity of nuclear inelastic scattering even to very small amounts of the Mössbauer-active isotope, this provides a path for the investigation of the lattice dynamics of α-$FeSi_2$.

Within the framework of this thesis, a growth protocol for epitaxial α-phase $FeSi_2$ nanostructures on the Si(111) surface was established and the lattice dynamics of this compound was investigated as a function of size and shape of the nanostructures. The sample preparation and characterization is presented in the following. The Fe-partial phonon density of states, obtained from nuclear inelastic scattering, is given and by comparison with *ab initio* calculations the effect of spatial confinement to the nanometer scale on the vibrational behavior and the thermoelastic properties is discussed.

5.1. Sample preparation and characterization

The samples were grown in the UHV-Analysis lab at KIT under UHV conditions ($P < 1\times10^{-8}$ Pa) using the MBE system shown in Figure 2.4. The Si(111) substrates were degassed in UHV at 650 °C for 4 h. Subsequently, the native SiO_2 layer was removed by heating the substrate two times to 1250 °C for 30 seconds. The nanostructures were grown by reactive deposition epitaxy (RDE), i.e. a certain amount of iron θ_{Fe} was deposited on the Si(111) substrate heated to the growth temperature T_G. An electron beam evaporator was used to create an atomic beam of high purity iron, enriched to 96 % in the Mössbauer-active isotope ^{57}Fe. The coverage was controlled by a quartz oscillator with an accuracy of 10 % and is given in Å and ML units. The given θ_{Fe} in Å corresponds to the thickness of an imaginary continuous

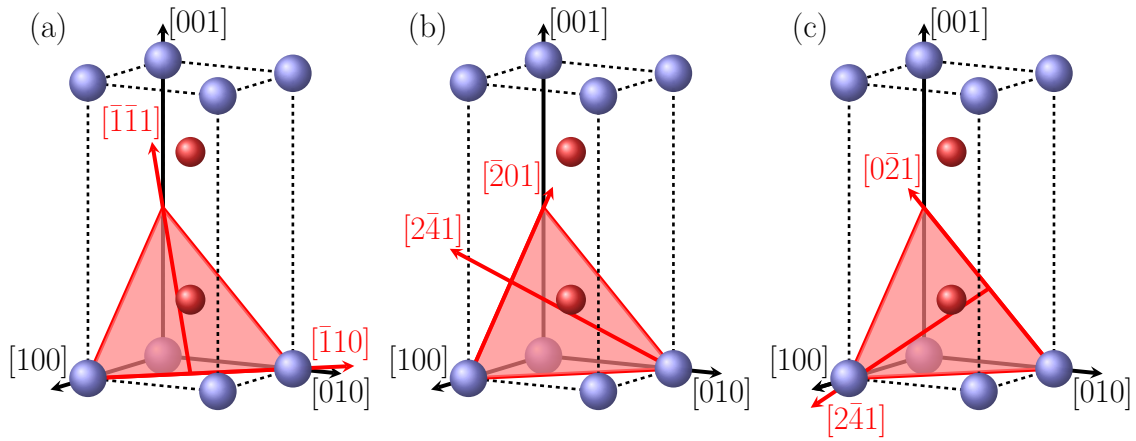

Figure 5.1: Unit cell of α-$FeSi_2$ with the α-$FeSi_2$(112) plane and the respective crystallographic directions of (a) configuration (i), (b) configuration (ii), (c) configuration (iii). For details see text.

Fe layer on the Si surface, whereas 1 ML ≙ one Fe atom per 1×1 Si(111) surface mesh [153]. The details of the growth and experimental conditions of the samples used for investigation of the lattice dynamics, referred to as S1 - S6, are summarized in Table 5.1. S1 was annealed at $T_A = 770\,°C$ for $t_A = 2\,h$ directly after the growth process to examine possible effects of annealing on the crystal structure and the lattice dynamics. After the structural characterization with RHEED and AFM, S1, S3, S5 and S6 were transferred in UHV to the sputter chamber shown in Figure 2.3 with a base pressure of $P < 1\times10^{-6}$ Pa and were capped with 4 nm of amorphous Si, deposited at room temperature. S2 and S4 were capped after the NIS experiments. All measurements described in the following were conducted at room temperature.

The growth of epitaxial α-phase $FeSi_2$ nanostructures on the Si(111) surface is thoroughly investigated, inter alia by electron microscopy [115, 171, 172], grazing-incidence x-ray diffraction [173], and combined RHEED and grazing-incidence x-ray diffraction [121]. The orientation of the α-$FeSi_2$ unit cell on the Si surface is driven by the minimization of the lattice mismatch. This is achieved when the

Table 5.1: Overview of the investigated samples. θ_{Fe} stands for the deposited amount of ^{57}Fe, T_G for the growth temperature, T_A for the annealing temperature and t_A for the annealing time. The last column denotes if the sample was capped with Si or measured *in situ* during the NIS experiment.

Sample	θ_{Fe} [Å]	θ_{Fe} [ML]	T_G [°C]	T_A [°C]	t_A [h]	NIS exp.
S1	2.2(2)	5.7(6)	700(10)	770(10)	2	Si cap
S2	2.2(2)	5.7(6)	700(10)	-	-	*in situ*
S3	0.6(1)	1.6(2)	700(10)	-	-	Si cap
S4	2.2(2)	5.7(6)	500(10)	-	-	*in situ*
S5	0.6(1)	1.6(2)	650(10)	-	-	Si cap
S6	0.6(1)	1.6(2)	500(10)	-	-	Si cap

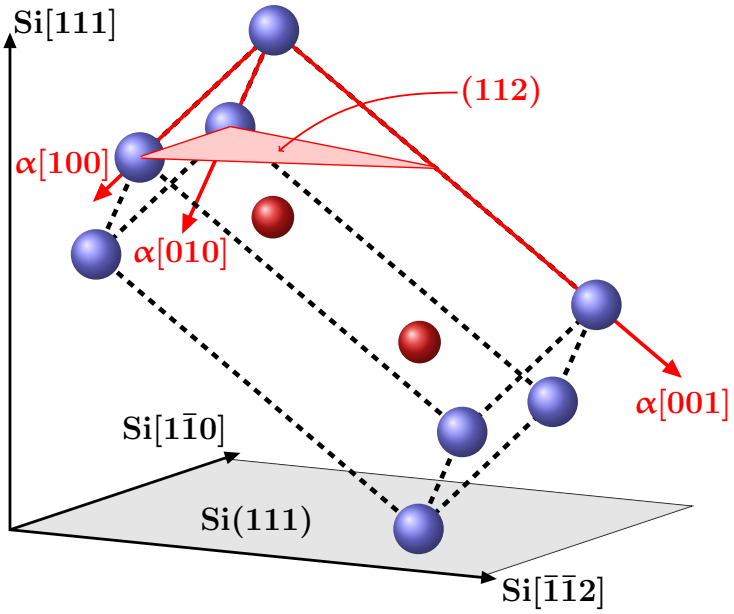

Figure 5.2: Configuration (i) (see text) of the α-$FeSi_2$ unit cell on the Si(111) surface. Directions and planes related to Si (α-$FeSi_2$) are given in black (red). Fe atoms are depicted in blue, Si atoms in red.

α-$FeSi_2$(112) plane is parallel to the Si(111) surface plane [α-$FeSi_2$(112)||Si(111)]. Due to the threefold symmetry of the Si(111) surface, the α-$FeSi_2$ unit cell can be accommodated in three different domain orientations rotated by 120° [115]:
(i) α-$FeSi_2$[$\bar{1}$10]||Si[1$\bar{1}$0] and α-$FeSi_2$[$\bar{1}\bar{1}$1]||Si[$\bar{1}\bar{1}$2],
(ii) α-$FeSi_2$[$\bar{2}$01]||Si[1$\bar{1}$0] and α-$FeSi_2$[2$\bar{4}$1]||Si[$\bar{1}\bar{1}$2],
(iii) α-$FeSi_2$[0$\bar{2}$1]||Si[1$\bar{1}$0] and α-$FeSi_2$[4$\bar{2}$1]||Si[$\bar{1}\bar{1}$2].
The coexistence of all three configurations on the same Si(111) surface gives rise to a pseudohexagonal surface symmetry [121, 173]. In Figure 5.1 the α-$FeSi_2$ unit cell is depicted together with the respective crystallographic directions aligned along Si[1$\bar{1}$0] and Si[$\bar{1}\bar{1}$2] in configuration (i)-(iii). The epitaxial relation between the Si(111) surface and configuration (i) is plotted in Figure 5.2. The lattice mismatch (defined as $(a_{Si} - a_{FeSi_2})/a_{Si}$) amounts to 0.79 % along Si[1$\bar{1}$0] and 3.92 % along Si[$\bar{1}\bar{1}$2] for all three configurations. For simplicity, in the following the directions of the RHEED, EXAFS, and NIS measurements, as well as the directions in the AFM images, are given along the orthogonal nonequivalent directions Si$\langle\bar{1}10\rangle$ and Si$\langle11\bar{2}\rangle$ of the Si(111) surface.

In Figure 5.3 the RHEED patterns obtained along Si$\langle11\bar{2}\rangle$ and Si$\langle\bar{1}10\rangle$ for the substrate (a,h) and for S1-S6 (b-g, i-n) are shown. Before growth, the diffraction pattern of a clean 7×7 reconstructed Si(111) surface is observed for all substrates. In Figure 5.3(c) the reflections of the Si$\langle11\bar{2}\rangle$ diffraction pattern are labeled according to [171]. The central (222) reflection and the intermediate (021) and (201) reflections are framed by the second order (042)/(402) and ($\bar{2}$20)/(2$\bar{2}$0) reflections. Due to the lower θ_{Fe}, the main spot of the Si(111) surface is still visible for S3, S5 and S6. In the RHEED patterns of S1-S4 well-separated diffraction spots are observed, which indicates a transmission geometry with the beam passing through 3D nanoislands.

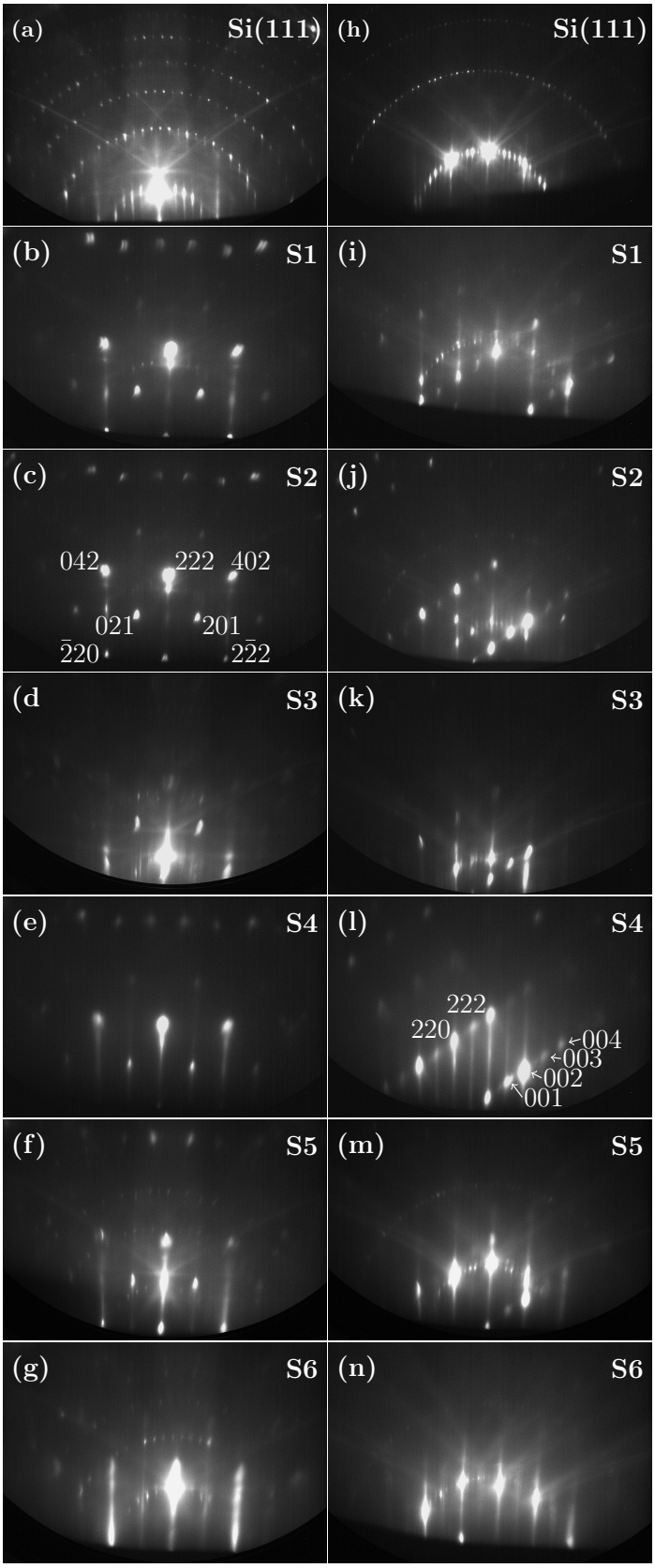

Figure 5.3: RHEED patterns of the Si(111) substrate (a), (h) and the investigated samples (b)–(g), (i)–(n) obtained with $E = 28\,\mathrm{keV}$ along Si$\langle 11\bar{2}\rangle$ (a-g) and Si$\langle \bar{1}10\rangle$ (h-n). In (c) and (l), the reflections are indicated following [171].

On the contrary, the patterns of S5 and especially S6 show a stronger contribution of streaks, suggesting the growth of 2D nanostructures with a small extension perpendicular to the Si(111) surface compared to their lateral extension. The 3D to 2D transition can also be observed in the RHEED patterns obtained along Si$\langle\bar{1}10\rangle$ [Fig. 5.3(i) - 5.3(n)]. The Si$\langle\bar{1}10\rangle$ diffraction pattern consists of two rows of spots containing the (001), (002), (003), (004), and (220), (222) reflections [Fig. 5.3(l)] [171]. The inclination angle formed between the shadow edge and the two imaginary lines the reflections are aligned on amounts to $\approx 35\,^{\circ}$. That corresponds to the tilt of the α-$FeSi_2$ unit cell with respect to the Si(111) surface, i.e. the angle between Si$[\bar{1}\bar{1}2]$ and α-$FeSi_2[001]$ (Fig. 5.2). When the sample is rotated around the surface normal, this inclination angle is repeated every $120\,^{\circ}$. Therefore, it can be concluded that all three possible epitaxial configurations of the α-$FeSi_2$ unit cell on the Si(111) surface are present in the investigated samples. Except for S4, the diffraction patterns show a contribution of the 7×7 reconstructed Si(111) surface, indicating the formation of well separated nanostructures. A comparison of the presented diffraction patterns with the results obtained by RHEED [121] confirms that the investigated structure is surface-stabilized tetragonal α-$FeSi_2$, forming the epitaxial relationship to the Si(111) substrate discussed above. Furthermore, the observed electron diffraction patterns coincide with the reciprocal space nodes theoretically predicted for tetragonal α-$FeSi_2$ on Si(111) and are in contradiction to the patterns expected for the cubic surface-stabilized s- and γ-phases [171], and the exclusive growth of α-$FeSi_2$ can be assumed.

The surface morphology of the samples, specifically the average height, average width and the shape of the nanostructures, was investigated by AFM. Exemplary AFM images of S1 - S6 are depicted in Figure 5.4. Figure 5.5 shows the normalized size distribution of the nanostructures obtained from the AFM measurements. For S1 the formation of triangular islands [Fig. 5.4(a)] with an average height of $\overline{h} = 20\,\text{nm}$ and an average width of $\overline{w} = 66\,\text{nm}$ [Fig. 5.5(a), 5.5(g)], measured along the symmetry axis of the triangle, is observed. S2 was grown with the same θ_{Fe} at the same T_G as S1 without post-growth annealing, resulting in the formation of islands with a slightly decreased average height of $\overline{h} = 18\,\text{nm}$ and a slightly increased average width of $\overline{w} = 72\,\text{nm}$. A closer look at Figure 5.4(b) shows a broadening of the islands of S2 along Si$\langle 11\bar{2}\rangle$, which is the direction of the AFM-tip movement. This indicates a degradation of the AFM tip used for this measurement, leading to a blurring of the image and a distortion of the nanostructure shape (as discussed in Section 2.2.2). In case of S3, the triangular shape of the nanoislands reoccurs. The reduction of θ_{Fe} compared to S1 and S2 leads to a reduction of the average height ($\overline{h}_1 = 15\,\text{nm}$) and width ($\overline{w}_1 = 49\,\text{nm}$). As observed for S1, the symmetry axis of the triangular islands is oriented along Si$\langle 11\bar{2}\rangle$, whereas the edges are pointing along Si$\langle\bar{1}10\rangle$. A similar orientation of triangular islands on Si(111) has previously been observed for $FeSi_2$ [175] and $CoSi_2$ [176]. In addition to the 3D islands, the AFM image of S3 reveals laterally extended ($\overline{w}_2 = 163\,\text{nm}$) flat ($\overline{h}_2 = 1.7\,\text{nm}$) structures. The reduction of the growth temperature to $T_G = 500\,^{\circ}\text{C}$ in case of S4 leads to a significantly narrowed height distribution with an average value of $\overline{h} = 4.4\,\text{nm}$, while the width is only slightly reduced to $\overline{w} = 44\,\text{nm}$. Despite the higher T_G compared to S4, the lower θ_{Fe} in case of S5 further narrows the height and the width distribution

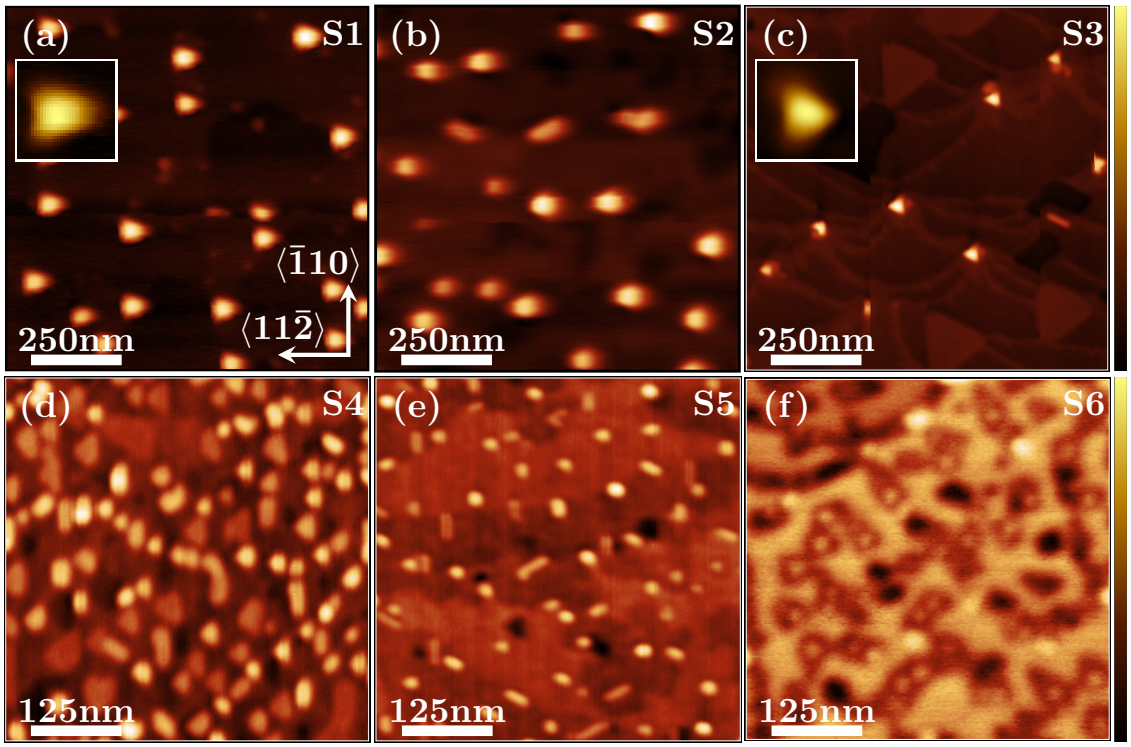

Figure 5.4: AFM images of the indicated samples with height scale (a) 0 - 36 nm, (b) 0 - 34 nm, (c) 0 - 24 nm, (d) 0 - 12 nm, (e) 0 - 11 nm, and (f) 0 - 9 nm. The crystallographic directions of the Si(111) surface are indicated in (a) and apply for all images. The color scales depicted on the right apply for all images. In the insets of (a) and (c) enlarged islands are depicted.

and the average values are reduced to $\overline{h} = 2.1$ nm and $\overline{w} = 27$ nm. The combination of low T_G and low θ_{Fe} applied in case of S6 leads to the formation of an intermittent $FeSi_2$ film along with islands grown in the Si surface areas not covered by the film. The average height of the islands is $\bar{h}_i = 0.8$ nm, the average height of the film is $\bar{h}_f = 2.1$ nm and the average island width is $\bar{w}$=18 nm.

As a conclusion, the samples can be divided into two growth regimes: the samples grown at $T_G = 700\,^{\circ}$C (S1 - S3) exhibit $\overline{w}/\overline{h}$-ratios between 3 and 4, whereas the samples grown at lower temperatures (S4 - S6) form flat nanostructures with $\overline{w}/\overline{h}$-ratios between 10 and 13. While the post-growth annealing conducted in case of S1 does not significantly change the morphology compared to S2, a reduction of θ_{Fe} from 2.2 Å (S2) to 0.6 Å (S3) at $T_G = 700\,^{\circ}$C leads to the formation of the very flat structures with large lateral extensions, which are only observed at this particular growth conditions. The reduction of T_G by 50 °C in S5 compared S3, both grown with $\theta_{Fe} = 0.6$ Å, leads to pronounced changes in the surface morphology and a significantly increased $\overline{w}/\overline{h}$ ratio. For $\theta_{Fe} = 2.2$ Å the 3D - 2D transition is observed in the temperature range from 700 °C to 500 °C. While the amount of deposited iron θ_{Fe} has a clear influence on the morphology, the growth temperature T_G seems to be the more important parameter for tuning the shape of the nanostructures.

The local crystal structure of S1 - S4 and S6 was determined by Fe K-edge x-ray absorption spectroscopy at the SUL-X beamline of the synchrotron radiation source

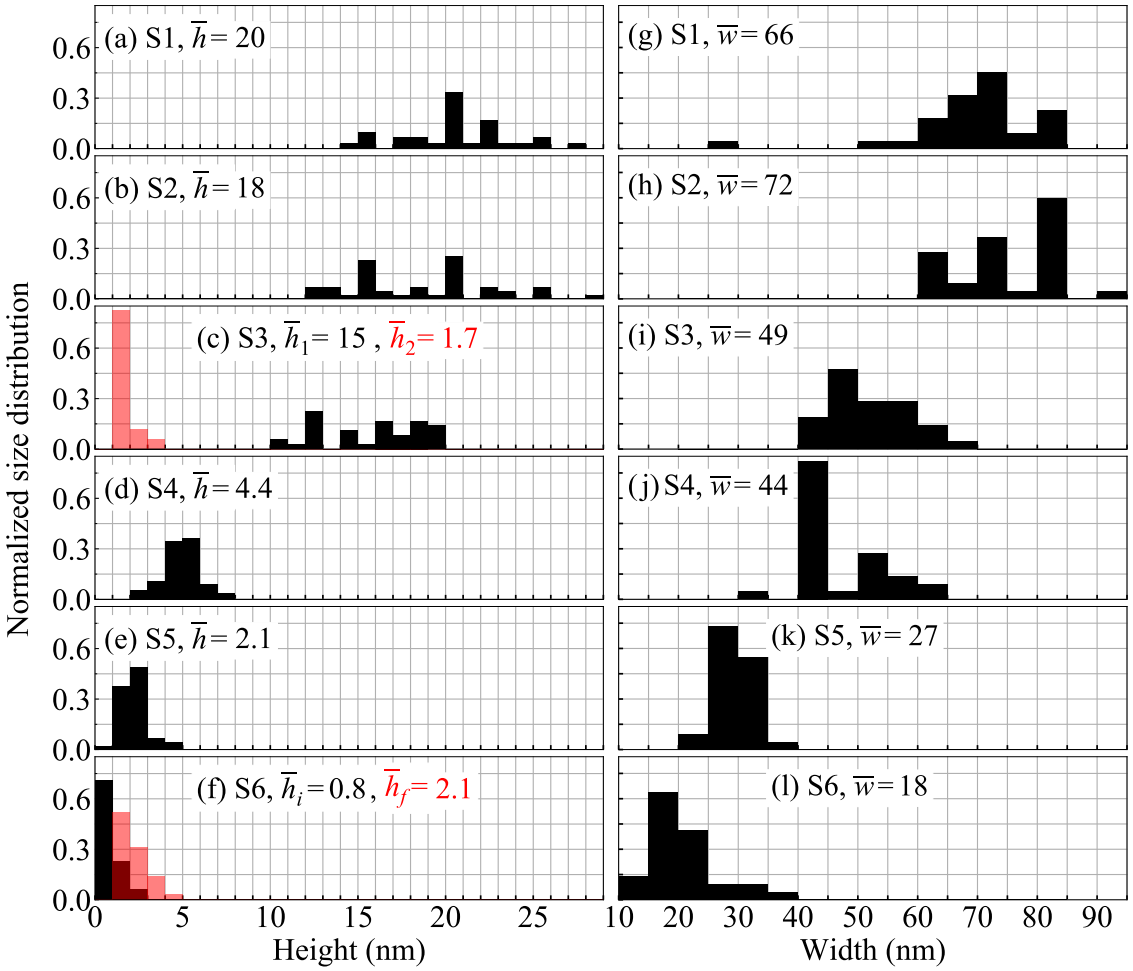

Figure 5.5: Normalized distribution of height (a)–(f) and width (g)–(l) of the nanostructures of the indicated samples deduced from the AFM study. The respective average values are given in nm. For S3 and S6 the height of the flat structures ($\bar{h}_2$) and the film ($\bar{h}_f$), respectively, are additionally given in red. The number of islands measured to obtain the distribution for each sample ranges between 30 and 55.

KARA at KIT. The measurements were conducted *ex situ*, i.e. after capping of the samples with 4 nm of amorphous Si. The experimental conditions are given in section 2.2.2. The fits of the EXAFS spectra presented in the following were performed by Dr. Vitova (Institute for Nuclear Waste Disposal, KIT). In Figure 5.6 the representative XAFS spectra, EXAFS spectra and Fourier transform of the EXAFS, obtained for the biggest and smallest nanostructures of S1 and S6, are depicted. In Figure 5.6(c) and 5.6(d) a very good agreement between the experimentally obtained and the modeled EXAFS spectra is observed. The spectra are weighted with k^3 for amplification of the oscillations at higher k values. Also the experimental Fourier transformed EXAFS are well reproduced by the fits for the first two coordination spheres, i.e. for the Si1.1 and Fe1.1 nearest neighbors [Fig. 5.6(e), 5.6(f)]. The results obtained for the interatomic distances and the coordination numbers of the Fe-Fe and Fe-Si scattering paths from the fits of S1 - S4 and S6 are presented in Table 5.2. They are compared with the theoretically predicted values of Fe-Si

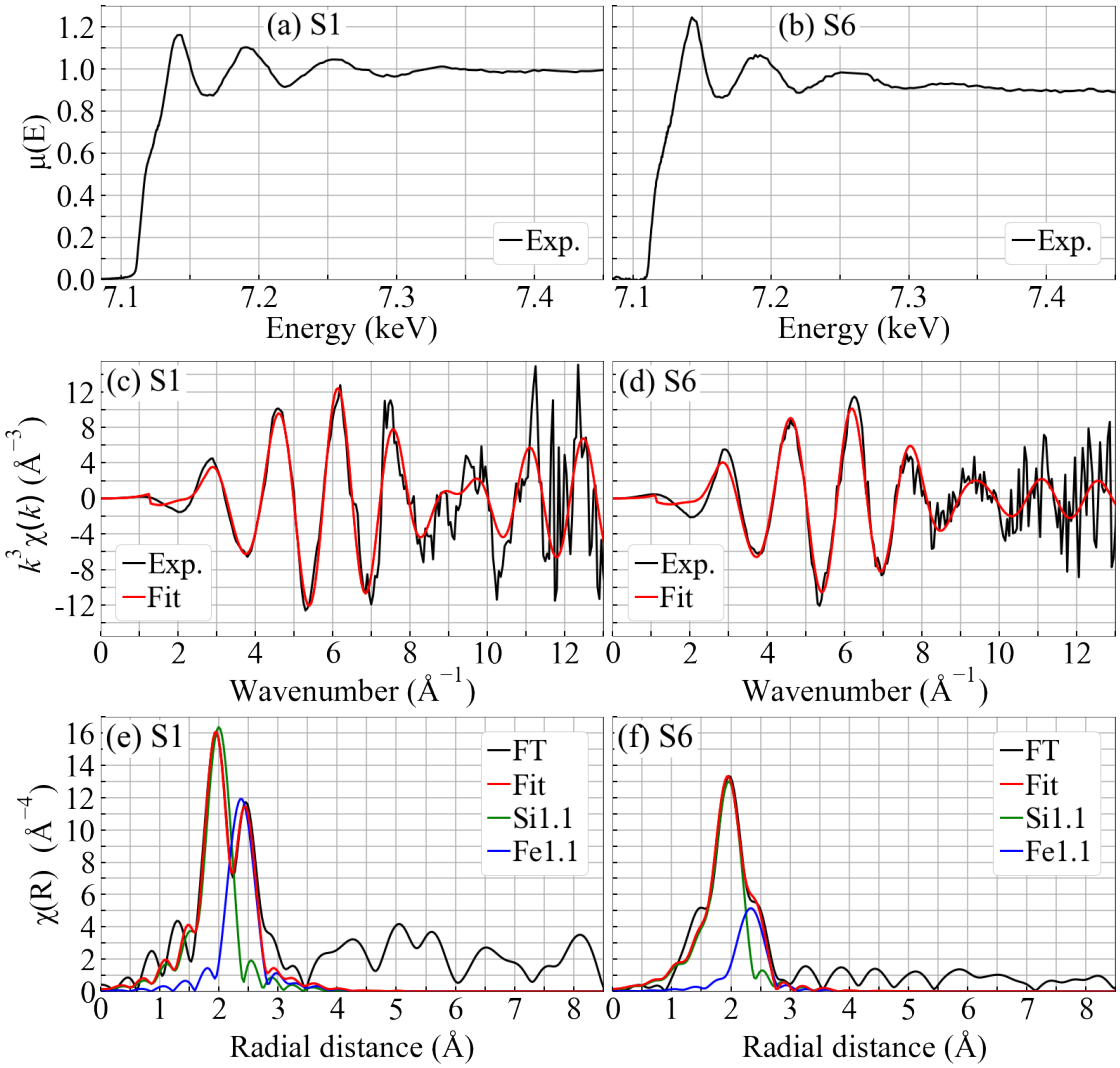

Figure 5.6: (a), (b) Normalized Fe K-edge XAFS spectra of S1 and S6. (c), (d) Fe K-edge EXAFS spectra (black) and the respective best fit results (red) obtained by modeling with α-$FeSi_2$. (e), (f) Fourier transform (FT) of the EXAFS spectra of (c) and (d), together with the respective fits and element-resolved subspectra.

phases formed on Si(111), i.e. α-, β-, γ- and s-phase [145–147]. By comparison of the interatomic distances obtained from the data analysis, the formation of γ- and β-phase $FeSi_2$ is excluded. The theoretically predicted coordination numbers for the s-phase clearly deviate from the fit results, while for α-$FeSi_2$ a good agreement is observed for both parameters. Thus, in combination with the RHEED study, the EXAFS results confirm the exclusive formation of α-$FeSi_2$. S6 exhibits a slightly reduced Fe-Fe distance as well as the lowest Fe-Fe and the highest Fe-Si coordination number. These variation in the coordination numbers most like originates from an accumulation of Si at the interface, as reported for $FeSi_2$ nanostructures grown on Si(111) [174]. Besides the interatomic distances and coordination numbers, with EXAFS also the mean square displacement (σ^2 in Table 5.2) of the atoms can be determined. For the Fe-Si scattering path the corresponding values are obtained by

the modeling of the EXAFS spectra, while for the Fe-Fe scattering path they were fixed during the optimization to the values obtained by NIS, which are presented below. On average, an increase of σ^2 is observed as the size of the nanostructures is decreasing from S1 to S6. This behavior can be explained by the larger relative amount of atoms located at the interfaces and surface in case smaller structures, where the reduction of the interatomic force constants leads to atomic vibrations with larger amplitudes.

Table 5.2: Interatomic distances (d), coordination numbers and mean square displacement (σ^2) obtained from modeling of the experimental EXAFS spectra and theoretical values for the expected $FeSi_2$ phases. The σ^2 values of the Fe-Si scattering path are obtained from the EXAFS fits, whereas for the Fe-Fe scattering path the values obtained by NIS are given. The k-range corresponds to the modeled range of the experimental EXAFS data. The values for α- and β-phase are obtained from ICSD 5257 and 9119, respectively, for s- and γ-phase no literature is available.

Sample	k-range ($Å^{-1}$)	Scattering path	d (Å)	Coord. number	σ^2 ($10^{-2}Å^2$)
S1	3.8 – 12.6	Fe-Si	2.36(1)	6.8(7)	0.40(1)
		Fe-Fe	2.69(1)	3.7(6)	1.08(2)
S2	3.8 – 15.5	Fe-Si	2.36(1)	8.2(2)	0.47(3)
		Fe-Fe	2.69(1)	3.9(2)	1.17(2)
S3	3.8 – 12.6	Fe-Si	2.36(2)	6.7(7)	0.70(2)
		Fe-Fe	2.70(2)	3.1(11)	1.15(2)
S4	3.8 – 12.6	Fe-Si	2.36(1)	7.7(9)	0.50(1)
		Fe-Fe	2.69(2)	3.7(6)	1.19(2)
S6	3.8 – 12.6	Fe-Si	2.35(2)	8.5(13)	0.70(2)
		Fe-Fe	2.67(3)	2.7(8)	1.22(2)
α-phase	-	Fe-Si	2.36	8	
		Fe-Fe	2.70	4	
β-phase	-	Fe-Si	2.36	8	
		Fe-Fe	2.97	2	
s-phase	-	Fe-Si	2.39	8	
		Fe-Fe	2.76	6	
γ-phase	-	Fe-Si	2.33	8	
		Fe-Fe	3.81	12	

5.2. Lattice dynamics

The Fe-partial phonon density of states of S1-S6 was obtained from nuclear inelastic scattering experiments performed at the Dynamics Beamline P01 at PETRA III [92] and the Nuclear Resonance Beamline ID18 at the ESRF [91]. As given in Table 5.1, S2 and S4 were measured *in situ*, i.e. after growth and characterization with RHEED and AFM they were transported to the beamlines under UHV conditions in a dedicated UHV chamber [177]. All measurements were performed at grazing-incidence geometry with an incidence angle $< 0.2°$ and an x-ray beam with dimensions of 1.5 mm × 0.01 mm (h×v, FWHM). The energy resolution for the photons with an energy of 14.413 keV was 0.7 meV at ID18 (S1, S2) and 1.1 meV at P01 (S3 - S6).

In Figure 5.7(a) - 5.7(f) the Fe-partial PDOS of S1 - S6, obtained along the orthogonal directions Si$\langle\bar{1}10\rangle$ and Si$\langle11\bar{2}\rangle$ of the Si(111) surface, are compared. For S3 only the spectrum along Si$\langle\bar{1}10\rangle$ was obtained. A comparison with the *ab initio* calculated Fe-partial PDOS of α-$FeSi_2$ [Fig. 3.3(c)(iii)] shows a good agreement of the peak positions between theory and experiment. The experimental PDOS is composed of the main peak of the z-polarized vibrations at 20 meV and the two peaks of the xy-polarized vibrations, which exhibit a shift of about 1 – 2 meV to lower energies compared to the theoretically predicted positions of 33 meV and 45 meV. Furthermore, S1 and S2, which were measured with higher energy resolution, exhibit a minor peak at 24 meV, whereas for S3 – S6 a shoulder is observed at similar energies. The minor peak in the *ab initio* calculated Fe-partial PDOS at 63 meV is also indicated in the experimental spectra. A comparison of the PDOS of S1 - S6 reveals a clear effect of the size of the nanostructures on the shape of the PDOS. While the peak of the z-polarized vibrations at 20 meV is very pronounced in S1 and S2, it is gradually damped with reducing average nanostructure size and is almost

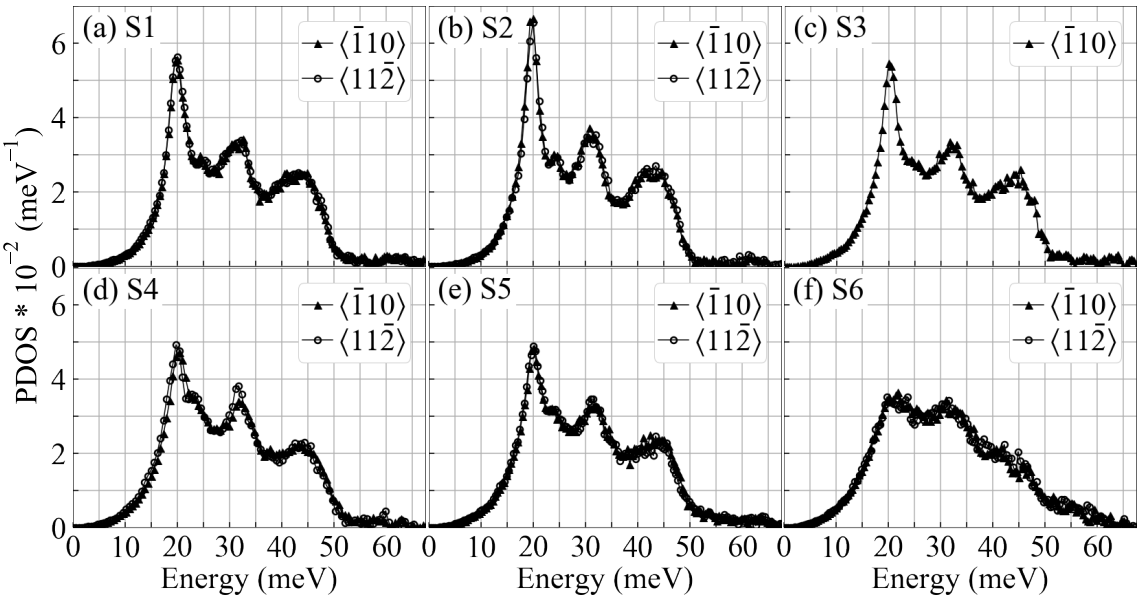

Figure 5.7: Fe-partial PDOS of the indicated samples obtained along Si$\langle\bar{1}10\rangle$ and Si$\langle11\bar{2}\rangle$.

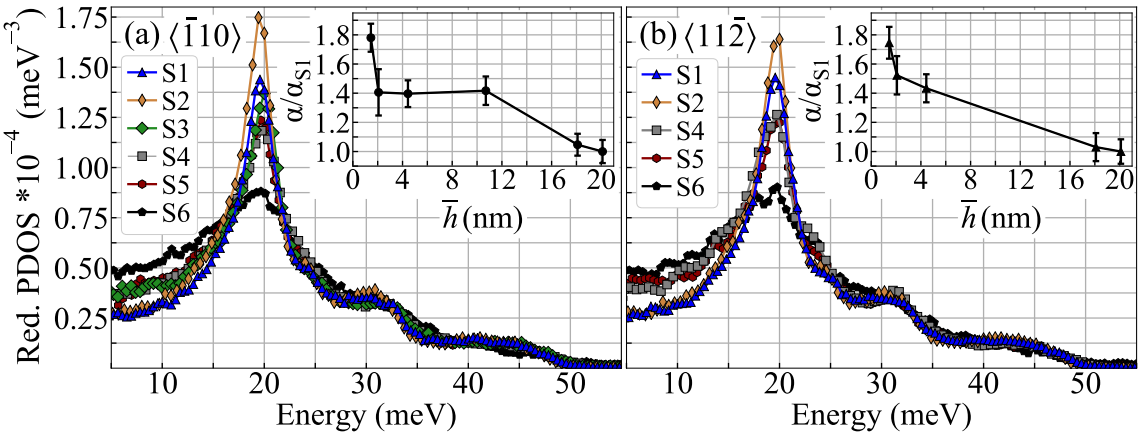

Figure 5.8: Fe-partial reduced PDOS $[g(E)/E^2]$ of the indicated samples obtained along (a) Si$\langle\bar{1}10\rangle$ and (b) Si$\langle11\bar{2}\rangle$. The insets show the coefficient α, normalized to the value of α_{S1}, obtained from $g(E) = \alpha E^2$ for the range 4,- 10 meV as a function of average island height.

completely suppressed in case of S6. On the other hand, the peaks at 33 and 45 meV, which originate from the xy-polarized vibrations, are less affected by the reduction of the average nanostructure size and a significant alteration is only observed in S6.

The damping of the peak at 20 meV is accompanied by an increase in the number of states at lower energies. This can clearly be seen in the reduced PDOS $[g(E)/E^2]$, which is compared for S1 - S6 for the measurements along Si$\langle\bar{1}10\rangle$ and Si$\langle11\bar{2}\rangle$ in Figure 5.8. According to the Debye model, the low-energy part of the PDOS can be described by $g(E) = \alpha E^2$ and consequently the low-energy enhancement in the smaller nanostructures can be quantified by determination of α. The insets in Figure 5.8 show the α values obtained for the range from 4 - 10 meV as a function of the average island height, normalized to the value obtained for S1. Due to the subtraction of the elastic peak (S_0 in Figure 2.10) from the nuclear inelastic scattering signal, the PDOS below 4 meV is not considered. Indeed, the number of low-energy states is enhanced by a factor of 1.8 along Si$\langle\bar{1}10\rangle$ and by 1.7 along Si$\langle11\bar{2}\rangle$ in S6 compared to S1. A similar behavior has been observed for thin films [18, 29] and surfaces [31], where it was attributed to epitaxial strain as well as broken translational symmetry at surfaces and interfaces. Also interface-specific vibrational modes could lead to the enhancement at low energies, as observed in Chapter 4. Consequently, it is more pronounced in small nanostructures, which exhibit a higher surface/interface-to-volume ratio.

Furthermore, the PDOS obtained along the orthogonal directions Si$\langle\bar{1}10\rangle$ and Si$\langle11\bar{2}\rangle$ are almost identical and a vibrational anisotropy is not observed. This contradicts earlier measurements on non-cubic single-crystalline systems, which revealed a strong vibrational anisotropy [87, 178, 179], and can be understood by consideration of the orientation of the α-$FeSi_2$ crystal on the Si(111) surface. The PDOS measured along a certain crystallographic direction is composed of a specific combination of x-, y-, and z-polarized phonons, as explained in section 2.2.3. In section 2.2.4 the approach used in the following for calculation of the relative weight of each contribution is discussed in detail. It projects the x, y and z vectors of the

α-$FeSi_2$ unit cell on the crystallographic direction the wave vector of the incoming x-ray beam is parallel to, denoted by the vector $\boldsymbol{\kappa}$. All vectors are expressed in the Cartesian coordinates of the tetragonal α-$FeSi_2$ unit cell. The *ab initio* calculations presented in this chapter where conducted for an 1 % tensile strained α-$FeSi_2$ lattice ($a = b = 2.727$ Å and $c = 5.14$ Å), to account for the epitaxial strain discussed above. Furthermore, it has to be taken into account that the RHEED study revealed that three domain orientations of the α-$FeSi_2$ crystal are present on the Si(111) surface. Consequently, the measurement along Si$\langle\bar{1}10\rangle$ corresponds to the simultaneous measurement along α-$FeSi_2[\bar{1}10]$, α-$FeSi_2[\bar{2}01]$, and α-$FeSi_2[0\bar{2}1]$; the measurement along Si$\langle 11\bar{2}\rangle$ corresponds to the measurement along α-$FeSi_2[\bar{1}\bar{1}1]$, α-$FeSi_2[2\bar{4}1]$ and α-$FeSi_2[4\bar{2}1]$. First, the normalized $\boldsymbol{\kappa}$ vectors are calculated for the three α-$FeSi_2$ directions parallel to the respective direction of measurement. For Si$\langle\bar{1}10\rangle$ it follows:

$$\kappa_{[\bar{1}10]} = \frac{1}{\sqrt{2a^2}}[-1a, 1a, 0], \tag{5.1}$$

$$\kappa_{[\bar{2}01]} = \frac{1}{\sqrt{4a^2 + c^2}}[-2a, 0, c], \tag{5.2}$$

$$\kappa_{[0\bar{2}1]} = \frac{1}{\sqrt{4a^2 + c^2}}[0, -2a, c], \tag{5.3}$$

while for measurements along Si$\langle 11\bar{2}\rangle$ it follows:

$$\kappa_{[\bar{1}\bar{1}1]} = \frac{1}{\sqrt{2a^2 + c^2}}[-1a, -1a, 1c], \tag{5.4}$$

$$\kappa_{[2\bar{4}1]} = \frac{1}{\sqrt{20a^2 + c^2}}[2a, -4a, c], \tag{5.5}$$

$$\kappa_{[4\bar{2}1]} = \frac{1}{\sqrt{20a^2 + c^2}}[4a, -2a, c]. \tag{5.6}$$

The PDOS $g^{\langle\bar{1}10\rangle}(E)$ measured along Si$\langle\bar{1}10\rangle$ is composed of the direction projected contributions $g_x(E)$, $g_y(E)$, and $g_z(E)$. Each contribution is weighted by the factors $A_x^{\langle\bar{1}10\rangle}$, $A_y^{\langle\bar{1}10\rangle}$, and $A_z^{\langle\bar{1}10\rangle}$, which are determined from the respective $\boldsymbol{\kappa}$ as:

$$\begin{aligned} g^{\langle\bar{1}10\rangle}(E) =& A_x^{\langle\bar{1}10\rangle} g_x(E) + A_y^{\langle\bar{1}10\rangle} g_y(E) + A_z^{\langle\bar{1}10\rangle} g_z(E) \\ =& \frac{1}{3}\left((\kappa^x_{[\bar{1}10]})^2 + (\kappa^x_{[\bar{2}01]})^2 + (\kappa^x_{[0\bar{2}1]})^2\right) g_x(E) \\ &+ \frac{1}{3}\left((\kappa^y_{[\bar{1}10]})^2 + (\kappa^y_{[\bar{2}01]})^2 + (\kappa^y_{[0\bar{2}1]})^2\right) g_y(E) \\ &+ \frac{1}{3}\left((\kappa^z_{[\bar{1}10]})^2 + (\kappa^z_{[\bar{2}01]})^2 + (\kappa^z_{[0\bar{2}1]})^2\right) g_z(E). \end{aligned} \tag{5.7}$$

The 1/3 factors follow from the assumption that all three domain orientations are equally likely. This yields $A_x^{\langle\bar{1}10\rangle} = A_y^{\langle\bar{1}10\rangle} = 0.3428$ and $A_z^{\langle\bar{1}10\rangle} = 0.3144$. The same procedure used for measurements along Si$\langle 11\bar{2}\rangle$ leads to $A_x^{\langle 11\bar{2}\rangle} = A_y^{\langle 11\bar{2}\rangle} = 0.3432$ and $A_z^{Si\langle 11\bar{2}\rangle} = 0.3136$. For the tetragonal α-$FeSi_2$ $g_x(E) = g_y(E)$ and therefore in the following $A_{xy}^{Si\langle\bar{1}10\rangle} = 0.6856$ and $A_{xy}^{Si\langle 11\bar{2}\rangle} = 0.6864$ are used. The differences in the weighting factors for Si$\langle\bar{1}10\rangle$ and Si$\langle 11\bar{2}\rangle$ are well below 1 %, which results in the vibrational isotropy observed in Figure 5.7(a) - 5.7(f).

Next, the gradual broadening of the PDOS features with decreasing nanostructure size is discussed. As described in section 2.1.3, the damping originates from a reduction of the phonon lifetime due to scattering at defects and dislocations, and can be described by the DHO function. The experimental PDOS is modeled by convolution of the *ab initio* calculated, direction-projected Fe-partial PDOS of α-$FeSi_2$, calculated for an 1 % tensile strained lattice, with the DHO function. The Q values leading to the best agreement between theory and experiment are determined by the least-squares method and are used to quantify the strength of the damping. The function used for description of the experimental spectra is given by:

$$g_{th}(E, Q_{xy}, Q_z) \;=\; A_{xy}\, g_{xy}(E, Q_{xy}) + A_z\, g_z(E, Q_z), \tag{5.8}$$

where $g_{xy}(E, Q_{xy})$ and $g_z(E, Q_z)$ are the *ab initio* calculated *xy*- and *z*-polarized Fe-partial PDOS, respectively, convoluted with the DHO function. Each contribution is weighted by the factors determined above, $A_{xy} = 0.69$ and $A_z = 0.31$. To ensure a valid comparison between the fit results obtained for samples measured at different beamlines with different energy resolutions, the *ab initio* calculated absorption probability density of α-$FeSi_2$ was convoluted with a Voigt profile with the FWHM corresponding to the energy resolution used for the respective sample. From these spectra the $g_{xy}(E)$ and $g_z(E)$ used for the modeling were calculated for each sample. Due to the observed vibrational isotropy, only the results obtained by modeling of the PDOS obtained along Si$\langle\bar{1}10\rangle$ are presented in the following.

The experimental data is fitted with two different approaches. In the first it is assumed that *xy*- and *z*-polarized phonons experience the same damping, consequently $Q_{xy} = Q_z$ in Equation (5.8). The results of the fits are presented in Figure 5.9(a) - 5.9(f). In general, the damping of the features in the experimentally obtained PDOS is well reproduced by the convolution of the *ab initio* calculated PDOS with the DHO function. The Q values obtained for S2 are significantly higher compared to S1, despite the fact that both samples were grown at the same conditions and exhibit similar average sizes and size distributions of the islands (see Fig. 5.5). A measurable effect of the capping layer present in S1 or the free surface present in S2 is not expected, since the low surface-to-volume ratio in the large islands of S1 and S2 implies that ca. 90 % of the Fe atoms exhibit a bulk-like coordination. A possible reason for the differences could be the post-growth annealing of S1, which was conducted at 70 °C above the growth temperature. This could lead to interdiffusion between substrate and islands and a reduction of interface sharpness, and consequently to an increased fraction of atoms located at irregular sites. For S3 the AFM study revealed that large 3D islands and flat 2D structures are formed. Therefore, the clear reduction of the Q value compared to S2 can be explained by stronger damping of phonons in the 2D structures. The distinct reduction of average height in S4 is also reflected by reduction of Q compared to S3. The Q obtained for S5 coincides within the error bars with S4, despite the further reduction of the average island height and width. It can be expected that the higher T_G in case of S5 leads to a higher degree of crystalline order and therefore to a reduction of the concentration of defects inside the nanostructures. This could compensate the size effect, as it was observed for Fe nanoparticles [164]. Another reason for the similar quality factors could be the fact that S4 is measured *in situ*, whereas S5 was capped with Si. Com-

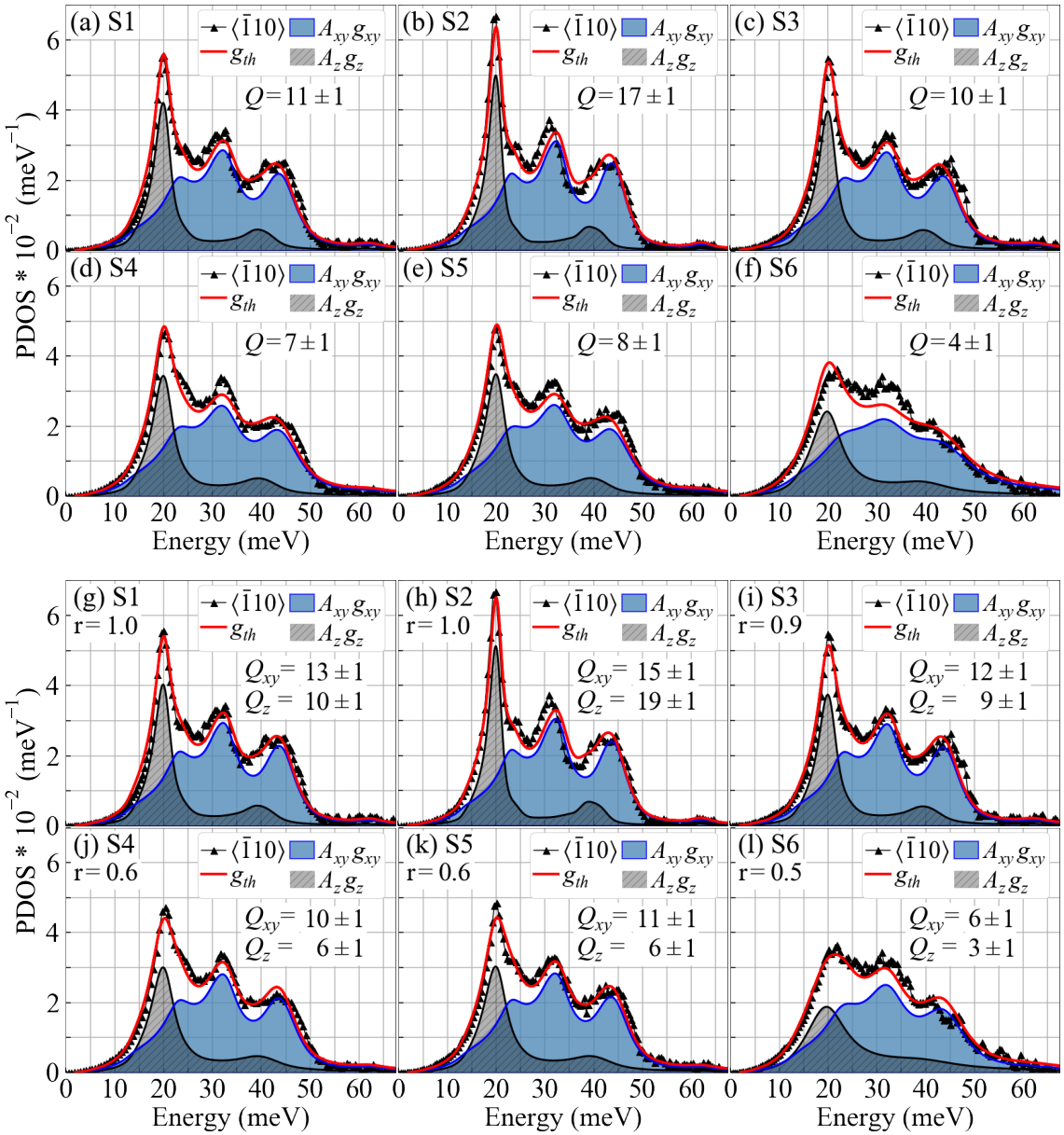

Figure 5.9: Comparison of the experimental PDOS obtained along Si$\langle\bar{1}10\rangle$ with the respective $g^{\langle\bar{1}10\rangle}(E)$ with (a)-(f) one common quality factor Q and (g)-(l) independent Q_{xy} and Q_z. The fit results are decomposed into their weighted xy ($A_{xy}g_{xy}$) and z (A_zg_z) contributions. In (g)-(l) the ratio between the sum of squares residuals from the fits assuming Q and Q_{xy}, Q_z of the respective sample are given as r.

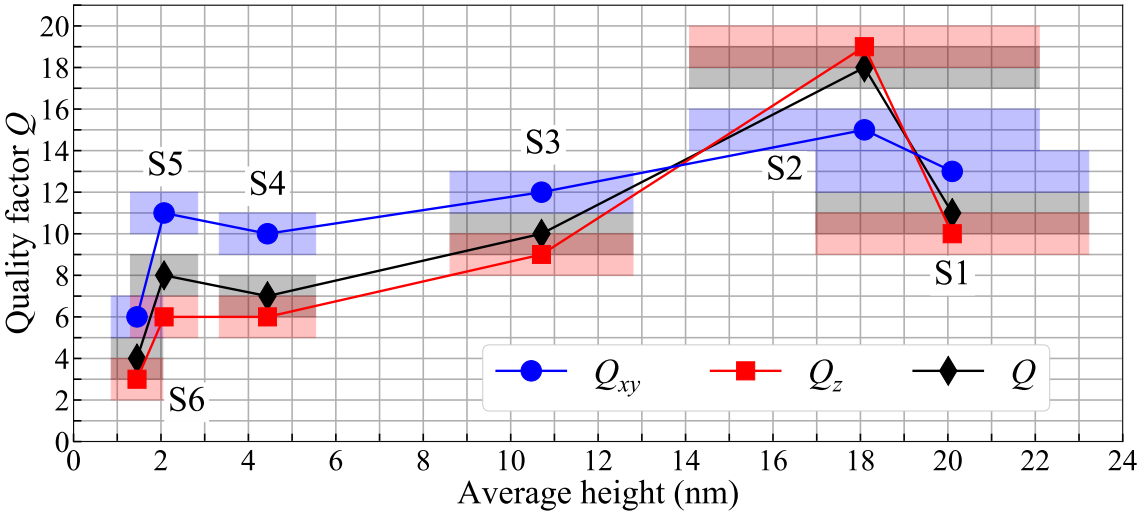

Figure 5.10: Quality factors Q and Q_{xy}, Q_z as a function of the average nanostructure height. The error of the height values corresponds to one standard deviation of the height distribution given in Figure 5.5.

pared to S1 and S2, the surface-to-volume ratio of the nanostructures in S4 and S5 is significantly higher, and hence the influence of the capping layer on the PDOS of S5 is no longer negligible. Surfaces typically exhibit phonon modes with lower energies due to the lower coordination of the surface atoms. The capping layer could partially suppress these surface modes and compensate the phonon-damping effect induced by the reduction of structure height. For S6 the Q value is again reduced compared to S4 and S5. In contrast to the strain-free Fe_3Si/GaAs heterostructure discussed in Chapter 4, the enhancement of low-energy states observed for the α-$FeSi_2$ nanostructures can completely be reproduced by convolution of the bulk *ab initio* calculated PDOS with the DHO function and does not require an additional interface specific component. The tensile-strained nanostructures investigated here were grown by reactive deposition epitaxy, which implies a certain degree of disorder at the Si/silicide interface [115]. As a consequence, no distinct interface-specific modes are observed. Furthermore, it is indicated in S4 and S5 and evident in S6 that the approach using $Q_{xy} = Q_z$ fails to model the height of the peak of the xy-polarized vibrations at 33 meV.

The second approach uses independent Q_{xy} and Q_z values for the modeling, in order to evaluate a possible polarization-dependence of the damping. The results are compared to the experimental data obtained along Si$\langle\bar{1}10\rangle$ in Figure 5.9(g) - 5.9(l). A very good agreement between theory and experiment is observed for all samples. In Figure 5.10 the quality factors obtained from the least-squares optimization for both approaches are plotted as a function of average nanostructure height. The width of the nanostructures is not considered, since the width/height ratio is between 3 and 4 for S1 – S3 and between 10 and 13 for S4 – S6. For this reason, confinement effects are expected to arise primarily due to the reduction of the height of the nanostructures. For all samples the Q values obatined with the first approach are in between the Q_{xy} and Q_z values obtained with the second. The dependence of the quality factors

obtained with both approaches on the nanostructure height can be explained by the increasing surface/interface-to-volume ratio upon reduction of $\bar{h}$. The growth of silicide/Si heterostructures by reactive deposition epitaxy is accompanied by an intrinsic degree of disorder at the silicide/Si interface [115]. In addition, the crystal periodicity is broken at the surface of the *in situ* measured nanostructures and at the transition to the amorphous Si layer in case of the capped samples. In both cases, the scattering of phonons is enhanced and the width of the respective PDOS features is increased. For nanostructures grown at the same temperature with different θ_{Fe} it can be assumed that the surface-to-volume ratio is higher for smaller θ_{Fe} (e.g. in S4 and S6). Consequently, the relative fraction of atoms at the surface/interface is increased and the damping effects have a stronger influence on the overall PDOS.

For evaluation of the two approaches, the sum of squared residuals obtained with the second approach is divided by the result obtained with the first. The ratio is given as r in Figure 5.9(g) - 5.9(l). It can be seen by the unassisted eye and is confirmed by the r values that both approaches lead to very similar results in case of the large 3D islands of S1, S2 and S3. While for S1 and S2 the sums of squared residuals are the same, for S3 it is increased by 10 % if $Q_{xy} = Q_z$ is assumed. In contrast, the results obtained for S4, S5 and S6 show that in case of the 2D islands the fit quality significantly improves when independent Q_{xy} and Q_z are used, since the peak of the z-polarized phonons undergoes a stronger damping compared to the xy-polarized vibrations. This effect could be attributed to a more efficient coupling of the low-energy z-polarized phonons to the soft modes present at surfaces and interfaces, compared to the high-energy xy-polarized vibrations. In addition, the strong spatial confinement in the nanostructures of S4, S5, and especially S6, could have a more pronounced effect on the long-wavelength acoustic phonons that constitute the PDOS peak at 20 meV, in contrast to the higher-energy, xy-polarized optical phonons. In any case, the reduction of the characteristic crystal size below 10 nm results in an anomalously strong damping of low-energy phonons that manifests itself in a polarization-dependent broadening of the PDOS features.

The determination of A_{xy} and A_z presented above is evaluated by modeling of the data with A_{xy} and A_z being additional free parameters in the mean square optimization process. Using the first approach, the fitted A_{xy} values are on average increased by 7 %, the Q values coincide within the errors. For the second approach the A_{xy} values are on average increased by 4 %. The obtained Q_{xy} values only slightly deviate and are on average by 4 % lower, while the reduction of A_z leads to an average increase of Q_z by 30 %.

5.3. Thermodynamic and elastic properties

In Table 5.3 the thermodynamic and elastic properties obtained from the Fe-partial xy- and z-polarized *ab initio* calculated PDOS projected along Si$\langle\bar{1}10\rangle$ and Si$\langle11\bar{2}\rangle$ are presented together with the results calculated from the experimental PDOS of S1 - S6. Furthermore, the coefficient α, derived from the low-energy part of the PDOS by the Debye model $g(E) = \alpha E^2$, and the sound velocity v_S are given. The isotropic vibrational behavior observed in the PDOS is also reflected in the mean

Table 5.3: Fe-partial mean force constant F, mean square displacement $\langle x^2 \rangle$, vibrational entropy S_V and lattice heat capacity C_V calculated from the *ab initio* *xy*- and *z*-polarized PDOS for α-phase $FeSi_2$, from their weighted sum projected along $\langle 11\bar{2} \rangle$ and $\langle \bar{1}10 \rangle$, as well as from the experimental PDOS. The coefficient α [$g(E) = \alpha E^2$] and the sound velocity v_S are also given.

	F (N/m)	$\langle x^2 \rangle$ (10^{-2}Å^2)	S_V $(k_B/at.)$	C_V $(k_B/at.)$	α $(10^{-5} meV^{-3})$	v_S (m/s)
theo. $\langle 11\bar{2} \rangle$	232	0.0109	2.81	2.63		
theo. $\langle \bar{1}10 \rangle$	232	0.0109	2.81	2.63		
S1 $\langle 11\bar{2} \rangle$	230(5)	1.10(2)	2.84(2)	2.63(2)	2.81(1)	4903(100)
S1 $\langle \bar{1}10 \rangle$	233(5)	1.08(2)	2.83(2)	2.63(2)	2.77(1)	4922(98)
S2 $\langle 11\bar{2} \rangle$	223(5)	1.14(2)	2.92(2)	2.65(2)	2.89(1)	4854(132)
S2 $\langle \bar{1}10 \rangle$	217(5)	1.17(2)	2.95(2)	2.66(2)	2.90(2)	4848(98)
S3 $\langle \bar{1}10 \rangle$	233(5)	1.15(2)	2.85(2)	2.63(2)	3.93(2)	4382(72)
S4 $\langle 11\bar{2} \rangle$	214(5)	1.23(2)	2.96(2)	2.66(2)	4.02(2)	4348(73)
S4 $\langle \bar{1}10 \rangle$	227(5)	1.19(2)	2.90(2)	2.64(2)	3.87(2)	4404(78)
S5 $\langle 11\bar{2} \rangle$	234(5)	1.19(2)	2.87(2)	2.63(2)	4.27(3)	4262(87)
S5 $\langle \bar{1}10 \rangle$	232(5)	1.16(2)	2.85(2)	2.63(2)	3.90(4)	4394(134)
S6 $\langle 11\bar{2} \rangle$	238(5)	1.22(2)	2.84(2)	2.62(2)	4.90(2)	4072(51)
S6 $\langle \bar{1}10 \rangle$	236(5)	1.22(2)	2.85(2)	2.63(2)	4.94(1)	4061(44)

force constant F, mean square displacement $\langle x^2 \rangle$, vibrational entropy S_V, and lattice heat capacity C_V, calculated from the *ab initio* PDOS projected along Si$\langle \bar{1}10 \rangle$ and Si$\langle 11\bar{2} \rangle$. Except for the mean force constant of S4, the values calculated from the experimental PDOS obtained along Si$\langle \bar{1}10 \rangle$ and Si$\langle 11\bar{2} \rangle$ for S1 – S6 coincide within the errors. The mean force constant of S1 – S6 does not exhibit a clear size-dependent trend. The relatively large values obtained for S6 originate from the enhancement of high-energy states above the cutoff energy, which is induced by the damping of the peak at 45 meV. S4 $\langle \bar{1}10 \rangle$ exhibits the biggest deviation from the theoretical results with a decrease of 8 %. The mean square displacement of S1 is in good accordance with the theoretical values, upon reduction of the average island height it is increased by 12 % in S6 compared to S1. For S_V the experimental values are on average increased by 2.4 %, while for C_V the average increase is below 0.3 %. A dependence on the nanostructure size is not observed for these parameters.

Due to the epitaxial relation and the strong coupling of the nanostructures to the substrate, the low-energy part of the PDOS of all samples can be described by the Debye model for three-dimensional crystals $g(E) = \alpha E^2$. The absolute values of the coeffcient α, which are given as normalized values in the insets of Figure 5.8, are given in Table 5.3. As described in section 2.2.3, the velocity of sound v_S can be calculated from the coefficient α. The theoretical values, obtained from the slope of the acoustic

branches of the phonon dispersions, amount to 5220 m/s for xy-polarized phonons and to 5430 m/s for z-polarized phonons. The values calculated for S1 and S2 are significantly lower compared to the theoretically predicted numbers. The reduction can be explained by the fact that the calculations are performed for a perfect crystal, whereas in a real crystal the propagation of sound waves is decelerated by phonon scattering. The higher surface-to-volume ratio in the smaller nanostructures leads to a further reduction of v_S, by 18 % in S6 compared to S1.

5.4. Conclusions

Epitaxial, surface-stabilized α-$FeSi_2$ nanostructures were grown by reactive deposition epitaxy on the Si(111) surface. The previously reported epitaxial relation between the substrate and the α-$FeSi_2$ crystal was confirmed by RHEED. Via EXAFS, the formation of α-$FeSi_2$ was additionally confirmed and the presence of other known surface-stabilized iron silicides was excluded. With an AFM study the size and shape of the nanostructures was determined. The average height of the nanostructures was in the range from 1.5 nm to 20 nm and the average width ranged from 18 nm to 72 nm. The growth can be divided into two regimes: at $T_G = 700\,^{\circ}\mathrm{C}$ mostly 3D nanostructures with width/height ratios between 3 and 4 are observed, while for $T_G \leq 650\,^{\circ}\mathrm{C}$ the formation of 2D nanostructures with width/height-ratios between 10 and 13 are formed.

The Fe-partial PDOS of the α-$FeSi_2$ nanostructures was determined by room-temperature nuclear inelastic scattering experiments. The probability of nuclear inelastic absorption was measured along two orthogonal directions of the Si(111) surface, Si$\langle\bar{1}10\rangle$ and Si$\langle11\bar{2}\rangle$. The PDOS obtained from these spectra revealed an isotropic behavior of the lattice vibrations, despite the strong vibrational anisotropy of the tetragonal α-$FeSi_2$ unit cell. This effect originates from the epitaxial relation between α-$FeSi_2$ crystal and substrate and the three different domain orientations of the α-$FeSi_2$ on the Si(111) surface. Calculation of the relative weights of the x-, y-, and z-polarized PDOS showed that they are equally weighted along both measurement directions and therefore the vibrational isotropy is observed.

Furthermore, a pronounced size-dependent phonon damping was evidenced. A comprehensive understanding of the effect was achieved by comparison of the experimental data with the *ab initio* calculations for α-$FeSi_2$. The phonon damping observed upon reduction of the nanostructure size was modeled by convolution of the *ab initio* PDOS with the DHO function and is explained by phonon scattering at defects located at surfaces and interfaces. In addition, the modeling revealed an anomalously strong damping of low-energy, z-polarized phonons, compared to high-energy, xy-polarized phonons. This is attributed to a more efficient coupling of the low-energy phonons to low-energy surface/interface-specific vibrational modes and a stronger effect of the spatial confinement on the long-wavelength acoustic phonons.

Calculation of the thermodynamic and elastic properties showed an enhancement of the low-energy states by a factor of 1.8, an increase of the mean square displacement of 12%, and a reduction of the sound velocity by 18 %, in the smallest 2D nanostructures compared to the largest 3D islands.

The reported results demonstrate that atomic vibrations along the crystallographic directions characterized with lower mean force constant, which in general exhibit lower energies, experience an anomalously strong damping upon reduction of the characteristic crystal dimensions to the nanometer scale. This effect is expected to be generally observed in nanostructures of single-crystalline materials with non-cubic unit cells.

6. Lattice dynamics of α-phase $FeSi_2$ nanowires

The continuous miniaturization of device components down to the nanometer scale brought top-down methods like optical lithography to their limits and promoted bottom-up approaches for the fabrication of nanoelectronic components. The growth of self-assembled nanostructures offers the possibility to specifically manipulate the spatial distribution and orientation of structures with dimensions of a few nanometers. Endotaxial silicide nanowires, grown on Si surfaces, exhibit an uniaxial alignment, a high degree of crystalline perfection and thermal stability, and sharp interfaces towards the substrate. These properties, in conjunction with the straightforward integration into Si technology, promoted them as promising candidates for applications in future nanoelectronics [153, 154]. Iron silicide nanowires have successfully been grown on the Si(110) [36, 143, 144, 151, 155, 180–183], Si(001) [184] and Si(553) [185] surface and their electronic and magnetic properties have comprehensively been investigated. Despite the variety of publications, the reports on the crystallographic phase, which determines the basic properties of the nanowires, remain contradictory. For very similar growth conditions, the formation of *s*- [36], γ- [144, 151], and α- [155] $FeSi_2$ nanowires on Si(110) is reported.

While the vibrational properties of nanowires have been extensively investigated by theoretical methods (e.g. [11, 186–196]), the challenges connected to the measurement of the lattice dynamics in nanostructures impede their experimental investigation and the available literature remains scarce. By application of optical methods, vibrational anomalies were revealed in Si [197–201] and III-V [202–204] nanowires. However, these results are restricted to certain vibrational modes and do not offer access to the overall vibrational behavior and the thermodynamic and elastic properties. By NIS the Te-partial PDOS of a Bi_2Te_3 nanowire array with an average nanowire diameter of 56 nm was determined, unveiling a reduction of the speed of sound by 7 % compared to the bulk material [205]. Another NIS study correlated the lattice softening observed upon reduction of the diameter from 100 nm to 18 nm in Sn nanowires to an increase of the critical temperature of the superconducting state [206].

In the following chapter the results of a systematic investigation of the lattice dynamics of endotaxial α-$FeSi_2$ nanowires are presented. First, the sample preparation and characterization, including the determination of the crystal phase of the nanowires, are discussed. Subsequently, the phonon density of states obtained along and across the nanowires is presented and the effect of the reduction of the average nanowire width from 24 nm to 3 nm is examined. The chapter is concluded with the thermodynamic and elastic properties of the nanowires.

6.1. Sample preparation and characterization

The samples were grown on Si(110) substrates in the UHV-Analysis lab at KIT in the MBE system shown in Figure 2.4. The removal of the native oxide layer and the growth process were conducted following the procedure described in Section 5.1. The amount of deposited iron θ_{Fe} is given in Å and monolayer (ML) units, where the Å values correspond to the thickness of an imaginary continuous Fe layer on the Si surface and 1 ML $\hat{=}$ one Fe atom per 1×1 Si(110) surface mesh [153]. Details of the growth and experimental conditions used for the investigated samples, hereinafter referred to as S1 - S7, are summarized in Table 6.1. After the structural characterization by RHEED and AFM, S1, S2, S3, S5, and S6 were capped with 4 nm of amorphous Si following the procedure described in Section 5.1. All measurements described in the following were conducted at room temperature.

In Figure 6.1(a) a typical RHEED pattern obtained for the Si(110) surface after removal of the native SiO_2 layer is shown. The pattern corresponds to a 16×2 reconstructed Si(110) surface [207], which is a prerequisite for the growth of high-aspect-ratio $FeSi_2$ nanowires [144]. Figure 6.1(b) - 6.1(f) shows generic RHEED patterns of S2, obtained after growth of the nanowires along several azimuths of the Si(110) surface. The Si(110) surface directions are given together with the angle between the wave vector of the electron beam and the nanowire orientation. From previous reports it is known that nanowires grown on Si(110) are oriented along Si$\langle\bar{1}10\rangle$, thus an angle of 90° denotes the measurement across the nanowires. The corresponding diffraction pattern consists of straight streaks with superimposed diffraction spots. When the sample surface is rotated with respect to the incoming electron beam, the streaks start to bend and the diffraction spots follow their curvature. The pattern measured along the nanowires [Fig. 6.1(f)] shows diffraction spots arranged on a semicircle. This evolution can be explained by consideration of the reciprocal space of uniaxially aligned, one-dimensional atomic chains. Along the chains, the peri-

Table 6.1: Overview of the investigated samples. θ_{Fe} stands for the deposited amount of ^{57}Fe and T_G for the growth temperature. The average dimensions of the nanowires, determined by the approach discussed in the text, are given as average height $\bar{h}$, width $\bar{w}$ and maximum extension across the nanowires $\bar{d}$. The last column denotes if the sample was capped with Si or measured *in situ* during the NIS experiment.

Sample	θ_{Fe} [Å]	θ_{Fe} [ML]	T_G [°C]	$\bar{h}$ [nm]	$\bar{w}$ [nm]	$\bar{d}$ [nm]	NIS exp.
S1	1.7(2)	3.0(3)	825(20)	15(5)	24(8)	58(20)	Si cap
S2	3.3(3)	6.0(6)	700(10)	11(4)	18(5)	45(12)	Si cap
S3	1.1(1)	2.0(2)	700(10)	5(1)	10(2)	29(5)	Si cap
S4	1.1(1)	2.0(2)	700(10)	6(1)	11(2)	31(6)	*in situ*
S5	0.8(1)	1.5(2)	600(10)	1.0(4)	4.0(5)	11(2)	Si cap
S6	0.6(1)	1.1(1)	600(10)	0.8(1)	3.0(3)	9(1)	Si cap
S7	2.2(2)	4.0(4)	825(20)	17(13)	26(20)	65(20)	-

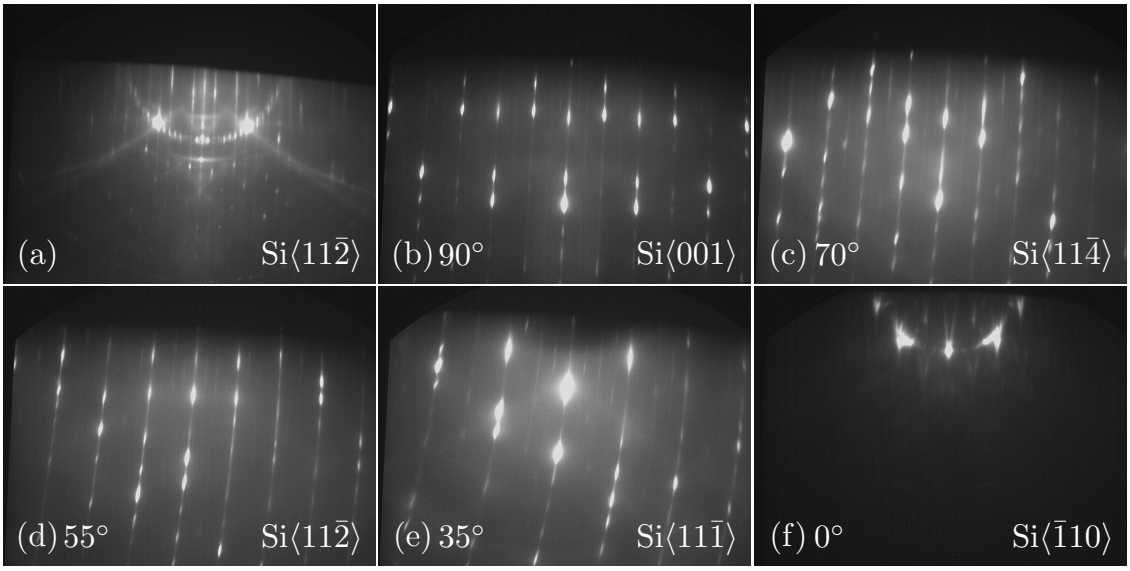

Figure 6.1: RHEED patterns obtained with E = 28 keV along different azimuths of the Si(110) surface. In (a) the diffraction pattern of the 16×2 reconstructed Si(110) surface obtained before growth is visible. In panels (b) - (f) diffraction patterns obtained for S2 along different directions of the Si(110) surface are shown. An angle of 90° denotes the measurement across the nanowires, while 0° denotes the measurement along the nanowires.

odic arrangement of atoms is described by the real space lattice parameter a. The reciprocal space of an arrangement of uncorrelated chains consists of homogeneous two-dimensional reciprocal space planes (RSPs), which are oriented perpendicular to the chains with a fixed inter-plane distance of $2\pi/a$. If the chains have a periodic arrangement perpendicular to their orientation, however, the RSPs are no longer homogeneous and exhibit nodes at certain positions [65, 208, 209]. It has been confirmed by various experimental reports, that these theoretical predictions can be applied for one-dimensional atomic arrangements on crystalline surfaces, e.g. [64, 66, 208, 210]. When the electron beam is parallel to the RSPs, the intersection of the Ewald sphere and the RSPs projeted onto the RHEED screen consists of straight streaks with superimposed diffraction spots, as observed for the measurement across the nanowires [Fig. 6.1(b)]. Upon reduction of the angle between the electron beam and the nanowire orientation, the projection onto the RHEED screen changes from straight lines to sections of ellipses [65]. Correspondingly, the streaks start to bend and the diffraction spots follow their curvature as observed in Figure 6.1(c) - 6.1(e). In addition, the distance between the reflections is increased. When the incident beam is parallel to the nanowires, the diffraction pattern consists of semicircles [Fig. 6.1(f)] and the distance between the neighboring reflections is larger than half the size of the screen. Thus, only the 0^{th} order reflection is visible. This trend is observed for all samples, confirming the formation of single-crystalline, uniaxially aligned nanowires.

In Figure 6.2 RHEED images of S1 - S6 measured across the nanowire orientation are compared. For all samples the main diffraction spots of the Si(110) surface

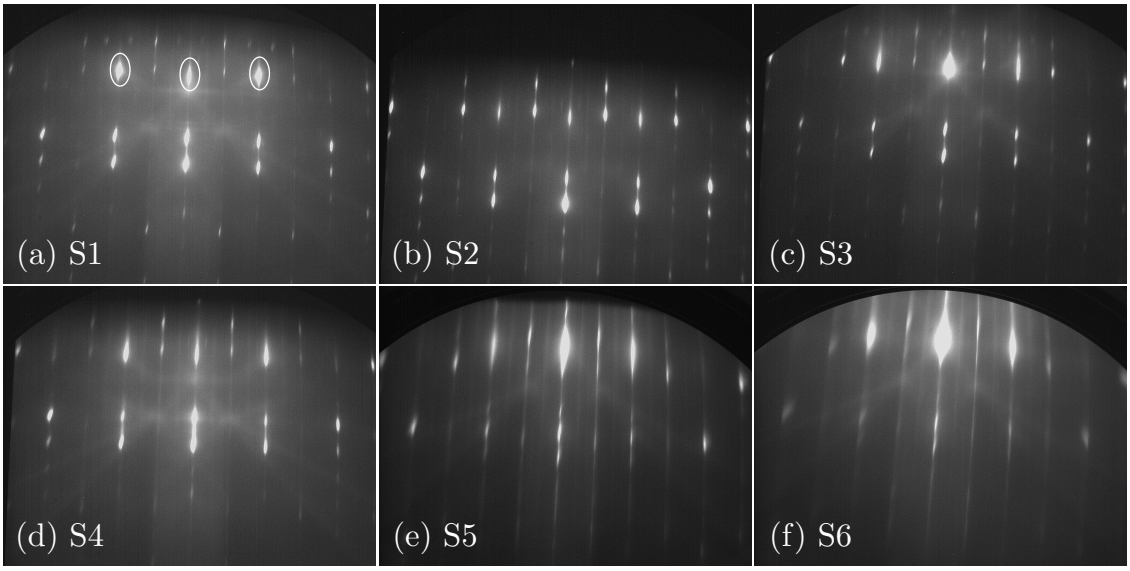

Figure 6.2: RHEED patterns of the indicated samples obtained at RT with E = 28 keV, taken along the Si⟨001⟩ azimuth. The white ellipses in (a) mark the main diffraction spots of the Si(110) surface.

and the nanowires, indicated by white ellipses in Figure 6.2(a), occur at the same positions before and after growth. Therefore, it can be assumed that the nanowires exhibit a very similar lattice parameter as the substrate along Si⟨$\bar{1}$10⟩. The structure of the diffraction patterns shows a clear dependence on the growth temperature T_G. For S1 ($T_G = 825°$ C) pronounced diffraction spots and faint streaks are observed, for S2, S3, and S4 ($T_G = 700°$ C) the relative intensity of the streaks increases and for S5 and S6 ($T_G = 600°$ C) continuous streaks are observed, while the higher order diffraction spots disappear. This indicates that a higher T_G leads to wider nanowires, which exhibit more intense diffraction nodes in the corresponding RSPs, while for smaller nanowires the RSPs are more homogeneous and more intense streaks are observed.

The local crystal structure of the nanowires of S7, S2 and S6 was determined by a combined experimental and theoretical Fe K-edge x-ray absorption spectroscopy study. Since S7 was grown at very similar conditions as S1 (see Table 6.1), it is concluded that the NWs of these two samples exhibit the same crystal structure. The experiments were conducted *ex situ*, i.e. after capping the samples with 4 nm of amorphous Si, under the conditions given in Section 2.2.2. The fits of the EXAFS spectra presented in the following were performed by Dr. Vitova. Samples S7, S2 and S6 cover the entire range of applied θ_{Fe} and T_G values (Tab. 6.1) and the obtained results on the local crystal structure shall likewise apply for the nanowires with intermediate range growth parameters. In Figure 6.3 the XAFS spectra, EXAFS spectra and EXAFS Fourier transforms obtained for S7, S2 and S6 are shown. A very good agreement is observed between the experimentally obtained EXAFS spectra and the fit results. The same applies for the corresponding EXAFS Fourier transforms. The values obtained from the fits for the interatomic distances and the coordination numbers of the Fe-Fe and Fe-Si scattering paths are presented in

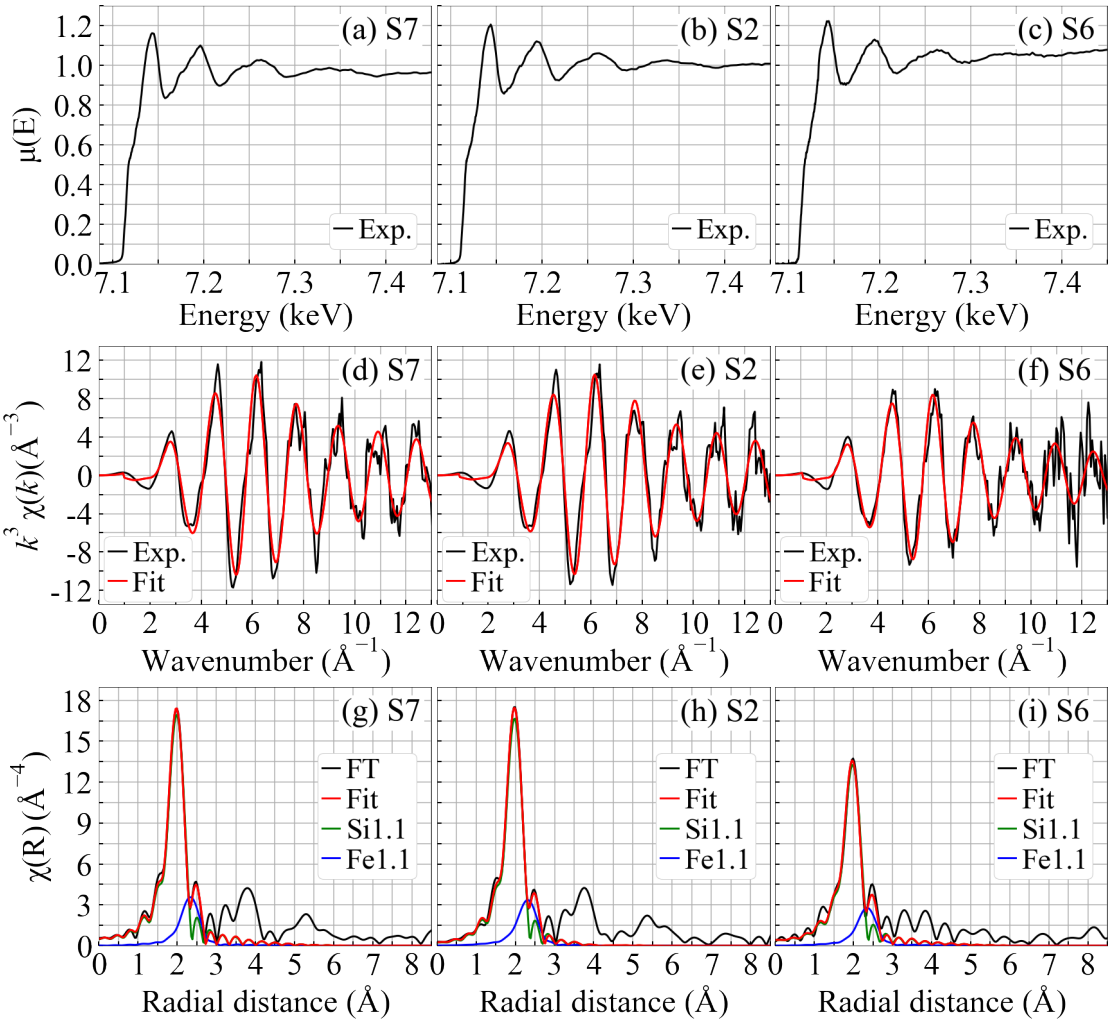

Figure 6.3: (a) - (c) Normalized Fe K-edge XAFS spectra of the indicated samples. (d) - (f) Fe K-edge EXAFS spectra (black) together with the respective best fit results (red), obtained by modeling with α-$FeSi_2$. The spectra are weighted with k^3 for amplification of the oscillations at higher k values. (g) - (i) EXAFS Fourier transforms (FT) together with the respective fits and element-resolved subspectra.

Table 6.2. For comparison, the theoretically predicted values of the crystal phases reported for $FeSi_2$ nanowires on Si(110) are given. For calculation of the theoretical values it has to be considered that in single crystals the intensity of the EXAFS signal depends on the orientation of the x-ray beam relative to the crystal axes. All XAFS spectra were measured with the wave vector of the x-ray beam being parallel to Si[$\bar{1}$10]. From literature, the crystallographic directions of the reported phases parallel to Si[$\bar{1}$10] can be determined: α-$FeSi_2$[1$\bar{1}$0], β-$FeSi_2$[010], γ-$FeSi_2$[$\bar{1}$10] and s-$FeSi_2$[$\bar{1}$10] [115, 147]. Correspondingly, the coordination numbers given in Table 6.2 were calculated with the x-ray beam projected along the respective direction.[i]

[i]In case of the single crystalline α-$FeSi_2$ nanostructures discussed in Chapter 5, various different domain orientations of the α-$FeSi_2$ crystal coexist on the Si(111) surface. The corresponding XAFS spectra are consequently measured as an average along several crystallographic directions and the projection procedure described here is not required.

Table 6.2: Interatomic distances (d), coordination numbers and mean square displacement (σ^2) obtained from modeling of the experimental EXAFS spectra and theoretical values for the expected $FeSi_2$ phases. The σ^2 values of the Fe-Si scattering path are obtained from the EXAFS fits, whereas for the Fe-Fe scattering path the values obtained by NIS are given. The values for α- and β-phase are obtained from ICSD 5257 and 9119, respectively, for s- and γ-phase no literature is available.

Sample	Scattering path	d (Å)	Coord. number	σ^2 (10^{-2}Å^2)
S7	Fe-Si	2.36(1)	7.4(4)	0.41(5)
	Fe-Fe	2.68(1)	2.6(3)	1.00(2)
S2	Fe-Si	2.35(1)	7.3(3)	0.41(4)
	Fe-Fe	2.67(1)	2.8(3)	1.01(2)
S6	Fe-Si	2.35(2)	6.6(5)	0.52(8)
	Fe-Fe	2.69(2)	2.3(5)	1.05(2)
α-phase	Fe-Si	2.36	8	-
	Fe-Fe	2.70	2	-
β-phase	Fe-Si	2.36	6	-
	Fe-Fe	2.97	2	-
s-phase	Fe-Si	2.39	4	-
	Fe-Fe	2.76	4	-
γ-phase	Fe-Si	2.33	4	-
	Fe-Fe	3.81	10	-

The comparison between theory and experiment excludes the formation of β-, s-, or γ-$FeSi_2$. For α-$FeSi_2$, on the other hand, a very good agreement is observed for the interatomic distances in the first and second coordination sphere and also the coordination numbers clearly indicate the formation of this phase. In the previous studies reporting the formation of α- [155], s- [36], and γ-$FeSi_2$ [144, 151], the phase was determined by TEM. Due to the very similar crystalline structure of the surface-stabilized $FeSi_2$ phases, their differentiation on the basis of electron transmission is difficult, as discussed e.g. in [143]. In contrast, the interatomic distances and coordination numbers of the first and second coordination sphere significantly differ for all reported phases. The complementary investigation presented here confirms the formation of α-$FeSi_2$ nanowires, as reported in [155], and resolves the controversy about the crystal phase of $FeSi_2$ nanowires on Si(110).

The mean square displacement values obtained from the EXAFS fits for the Si atoms show a 25 % increase in S6 compared to S7 and S2. The values of S7 and S2 agree with the results obtained for the biggest α-$FeSi_2$ nanoislands discussed in Chapter 5, while the increase upon reduction of the nanostructure size is significantly stronger in the nanoislands. The reason for these differences between nanoislands

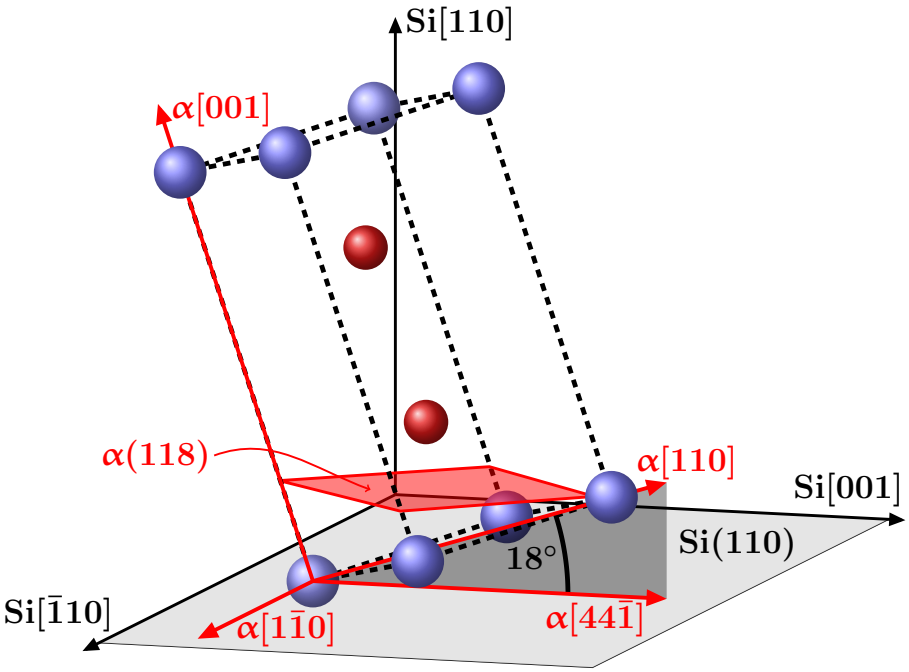

Figure 6.4: Orientation of the α-$FeSi_2$ unit cell on the Si(110) surface. Directions and planes related to Si (α-$FeSi_2$) are given in black (red). Fe atoms are depicted in blue, Si atoms in red.

and nanowires is the lower interface-to-volume ratio and embedded character of the nanowires, which result in a lower contribution of atoms located at surfaces and interfaces, which generally exhibit a larger mean square displacement.

For the growth of α-$FeSi_2$ on Si(111) (see Chapter 5) and Si(001) [152, 211] the commonly reported epitaxial relation is Si{111}||α-$FeSi_2${112}. The lattice mismatch is minimized if Si⟨$\bar{1}$10⟩||α-$FeSi_2$⟨1$\bar{1}$0⟩ [115]. Translated on the Si(110) surface, this leads to: Si(110)||α-$FeSi_2$(118) and Si[$\bar{1}$10]||α-$FeSi_2$[1$\bar{1}$0], as depicted in Figure 6.4. Compared to the Si(111) surface, the situation is simplified by the lower symmetry of the Si(110) surface, which does only allow for one domain orientation. This epitaxial relation leads to a small lattice mismatch [defined as $(a_{Si} - a_{FeSi_2})/a_{Si}$)] of 0.6 % along Si[$\bar{1}$10], which was indicated by the RHEED study, and along Si[001] it amounts to 1 %. The tilt between the α-$FeSi_2$ unit cell and the Si(110) surface is quantified by an angle of 18° between α-$FeSi_2$[110] and Si[001]. Furthermore, this configuration implies that α-$FeSi_2$[44$\bar{1}$] is 0.5° off Si[001] (Fig. 6.4).

The surface morphology of the samples was investigated by AFM. Overview scans of S1 - S6 are shown in Figure 6.5. As expected from the RHEED study, all samples exhibit nanowires uniaxially aligned along Si[$\bar{1}$10]. The formation of uniaxially aligned nanowires on the Si(110) surface may originate from a shape transition of strained islands [184, 212] or the anisotropic diffusion of material [144, 213]. Most likely both mechanism occur simultaneously. The epitaxial relation discussed above implies that α-$FeSi_2$[1$\bar{1}$0]||Si[$\bar{1}$10]. Furthermore, due to the small deviation of 0.5° it is approximated that α-$FeSi_2$[44$\bar{1}$]||Si[001]. For S1, the deposition at $T_G = 825\,°C$ leads to the formation of well separated nanowires with lengths of several µm. In addition, small pyramidal nanodots are observed on the surface, which are reported

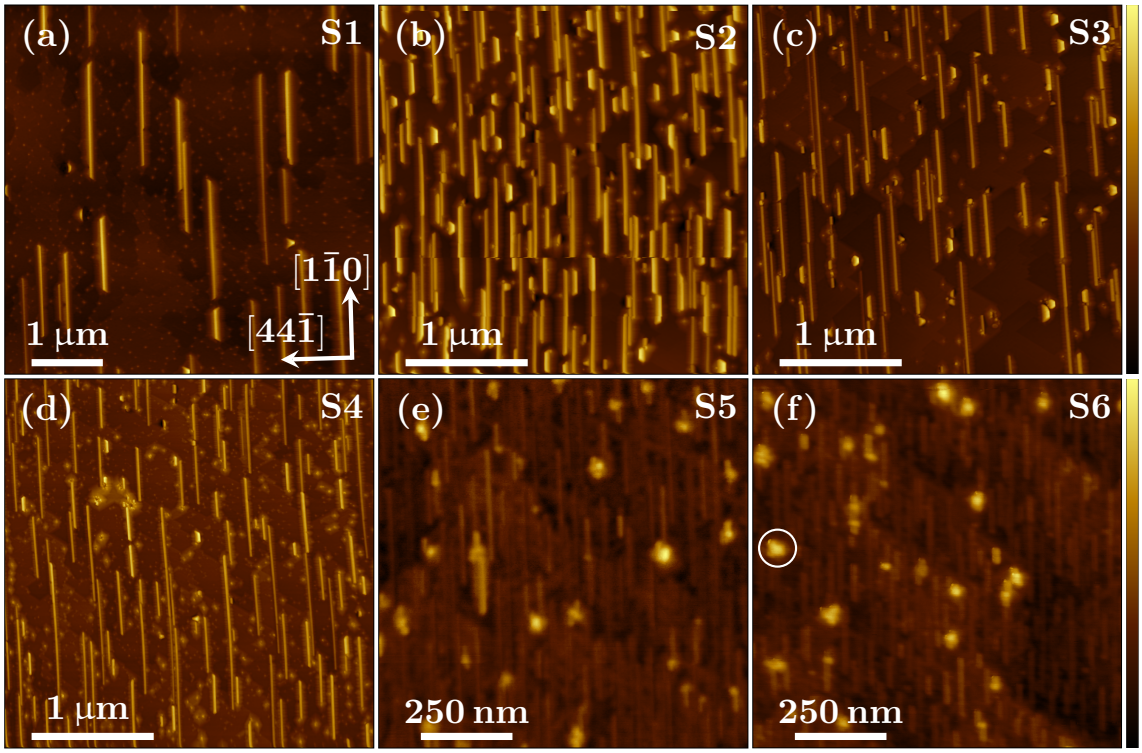

Figure 6.5: AFM images of the indicated samples with height scale (a) 0 - 59 nm, (b) 0 - 39 nm, (c) 0 - 30 nm, (d) 0 - 37 nm, (e) 0 - 10 nm, and (f) 0 - 12 nm. In (a) the crystallographic directions of the α-$FeSi_2$ crystal are indicated. The color scales depicted on the right apply for all images. The white circle in (f) marks an exemplary copper contamination.

to be the initiation points of the nanowire growth [144]. At certain locations, the atomic steps of the 16×2 reconstruction are resolved by the *in situ* non-contact AFM and are visible as chevron structures. The reduction of T_G and the increase of the amount of deposited iron θ_{Fe} in case of S2 lead to densely packed nanowires with lengths ranging from hundreds of nm to several µm. The threefold reduction of θ_{Fe} in S3 and S4 compared to S2 significantly reduces the density of nanowires and increases their aspect ratio. For both samples, a comb-like structure at the nanowires sidewalls is nicely resolved, which is also present in S1 and S2. These are Si facets that originate from the chevron atomic arrangements on the 16×2 reconstructed Si(110) surface and emerge during growth of the silicide [144]. For S5 and S6, which were grown with $T_G = 600\,°C$, the reduced surface mobility of the impinging Fe atoms results in densely packed nanowires with lengths ranging from 100 nm to about 400 nm. In addition, round islands are present, an example is marked with a white circle in Figure 6.5(f). These structures occur after the removal of the native SiO_2 layer and were identified as a copper contamination by x-ray photoelectron spectroscopy. However, the ^{57}Fe-partial phonon density of states obtained with the element and isotope selective NIS is not affected by the Cu islands.

The characteristic parameter for investigation of size effects on the vibrational behavior is the nanowire width and a precise determination of the average values is essential. However, the endotaxial growth mechanism implies a distinctly asymmet-

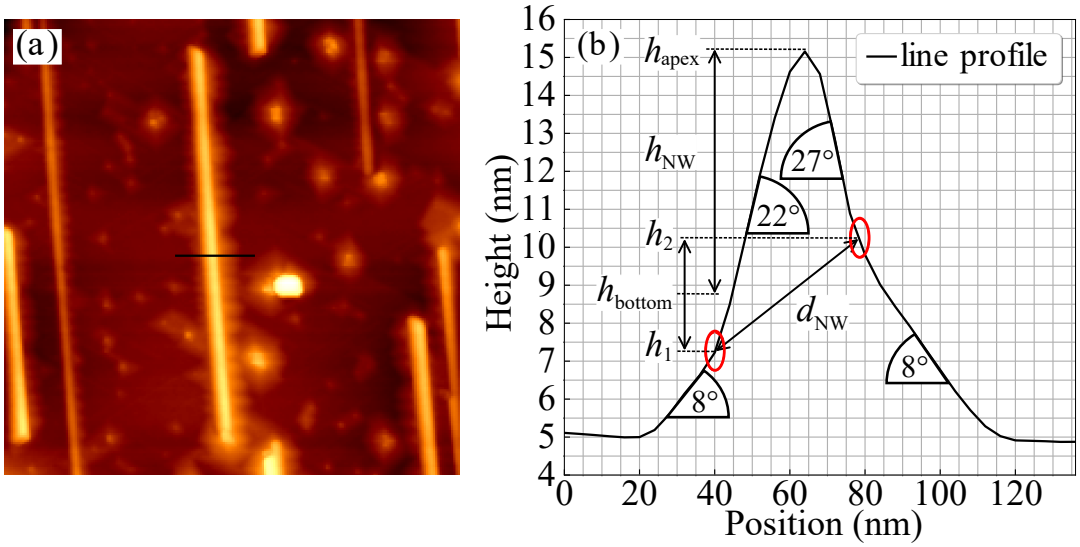

Figure 6.6: (a) AFM image of S3, the black line corresponds to the exemplary line profile shown in (b), which is used for illustration of the determination of the $\bar{h}$, $\bar{w}$ and $\bar{d}$ values given in Table 6.1.

rical shape of the nanowire cross section and that a large fraction of the nanowires is embedded into the substrate. This considerably complicates the determination of the nanowire dimensions. With TEM a precise determination of the dimensions of embedded structures is possible, but the cumbersome preparation of TEM samples limits the number of nanowires that can actually be measured and a statistical evaluation is not possible for a set of seven samples. AFM allows for the measurement of a large number of nanowires in a relatively short time, but the nanowire part below the substrate surface is not accessible. These limitations can be overcome by correlation of the results obtained with both methods. It was demonstrated by comparison of TEM cross sections and STM line scans that the line profile of an $FeSi_2$ nanowire grown on Si(110) consists of two parts: The $FeSi_2$ nanowire, which exhibits angles between 20 ° and 30 ° towards the Si(110) surface, and two Si facets on the left and right, which are seen as a comb-like structure at the nanowires sidewalls, forming angles of about 7 ° towards the Si(110) surface [143, 144] (see Figure 3.2). The AFM images shown in Figure 6.5 exhibit the same topography. In Figure 6.6(a) an exemplary nanowire of S3 is shown, in (b) the corresponding line profile is given. The transition from the Si facets to the $FeSi_2$ nanowire, marked with red ellipses, can clearly be identified. The slope of the sidewalls is very similar to what was previously reported, it changes from 8° to 22° on the left side and from 8° to 27° on the right side of the line profile. The dimensions of the nanowires can be quantified by different parameters. The maximum extension across the nanowire is given by the distance between the inflection points and is denoted by d_{NW} in Figure 6.6(b). However, this is the upper limit for the nanowire width, which is not completely suitable for description of the size effects on the lattice vibrations. Furthermore, the d_{NW} values obtained by AFM are biased due to the shape of the AFM tip. This is especially critical for S5 and S6, which exhibit dimensions comparable to the AFM tip diameter (see Section 2.2.2). In contrast, the height of the nanowire

can be measured with sub-nanometer resolution and is not affected by the AFM tip shape. Therefore, it is preferable to use this parameter for determination of the nanowire dimensions. In [143], a correlation between the height of the nanowires above the Si(110) surface (h_{NW}) and the corresponding cross-sectional area (A_{NW}) was derived by a combined STM/TEM study: $A_{NW} = 2 * (h_{NW} + 1.6)^2$. To account for the asymmetrical shape, the lateral dimension of the nanowires is defined as $w_{NW} = \sqrt{A_{NW}}$ [143]. The average values obtained for S1 - S7 of $\bar{h}_{NW}$, $\bar{w}_{NW}$ and $\bar{d}_{NW}$ are given in Table 6.1 . The height values h_{NW} were measured as the difference between the nanowire apex (h_{apex}) and the middle between the heights measured for the Si substrate/$FeSi_2$ nanowire transition ($h_{bottom} = h_1 + \frac{h_2 - h_1}{2}$) [Fig. 6.6(b)]. The results show a significant reduction of the average nanowire dimension from S1 to S6, from $\bar{w}_{NW} = 24$ nm to $\bar{w}_{NW}$=3 nm and from $\bar{d}_{NW}$=58 nm to $\bar{d}_{NW}$ =9 nm. The parameter used in the following as a characteristic measure for the nanowire dimension is $\bar{w}_{NW}$.

6.2. Lattice dynamics

The Fe-partial phonon density of states of S1 - S6 was obtained from nuclear inelastic scattering experiments performed at the Nuclear Resonance Beamline ID18 at the ESRF [91] and the Dynamics Beamline P01 at PETRA III [92]. At both beamlines, the measurements were performed at grazing-incidence geometry with an incidence angle $< 0.2°$ and an x-ray beam with dimensions of 1.5 mm × 0.01 mm (h × v, FWHM). The energy of the x-ray beam was tuned around the ^{57}Fe resonance at 14.413 keV with an energy resolution of 0.7 meV for S1, S2 (ID18), 1.0 meV for S3, S4 (P01) and 1.3 meV for S5, S6 (P01). For the investigation of possible surface effects, S4 was measured *in situ* in a dedicated UHV chamber [177], while all other samples were covered with a 4 nm Si capping layer.

In Figure 6.7 the Fe-partial PDOS obtained with the wave vector of the x-ray beam being parallel to α-$FeSi_2[1\bar{1}0]$ (left column) and α-$FeSi_2[44\bar{1}]$ (right column) are depicted. Along the nanowires, the PDOS is composed of peaks at 31 meV and 44 meV and a minor peak around 25 meV. The PDOS obtained across the nanowires exhibits the same features, with an addional peak at 20 meV, which is completely absent along the nanowires. A comparison with the *ab initio* calculated, direction-projected Fe-partial PDOS of α-$FeSi_2$ presented in Figure 3.3(c) shows that the PDOS obtained along the nanowires consists of *xy*-polarized vibrations only, whereas the PDOS across the nanowires seems to have an additional contribution of *z*-polarized vibrations. With the same approach as used in Chapter 5, the relative contribution of the *xy*- and *z*-polarized vibrations can be determined by projection of the x, y and z vectors of the α-$FeSi_2$ unit cell on a normalized vector parallel to the wave vector of the incoming x-ray beam, denoted by $\boldsymbol{\kappa}$ (detailed discussion in Section 2.2.4). The vectors are expressed in the Cartesian coordinates of the tetragonal α-$FeSi_2$ unit cell. To account for the lattice mismatch discussed above, the *ab initio* calculations have been conducted for a 0.5 % tensile strained α-$FeSi_2$ lattice with $a = b = 2.714$ Å

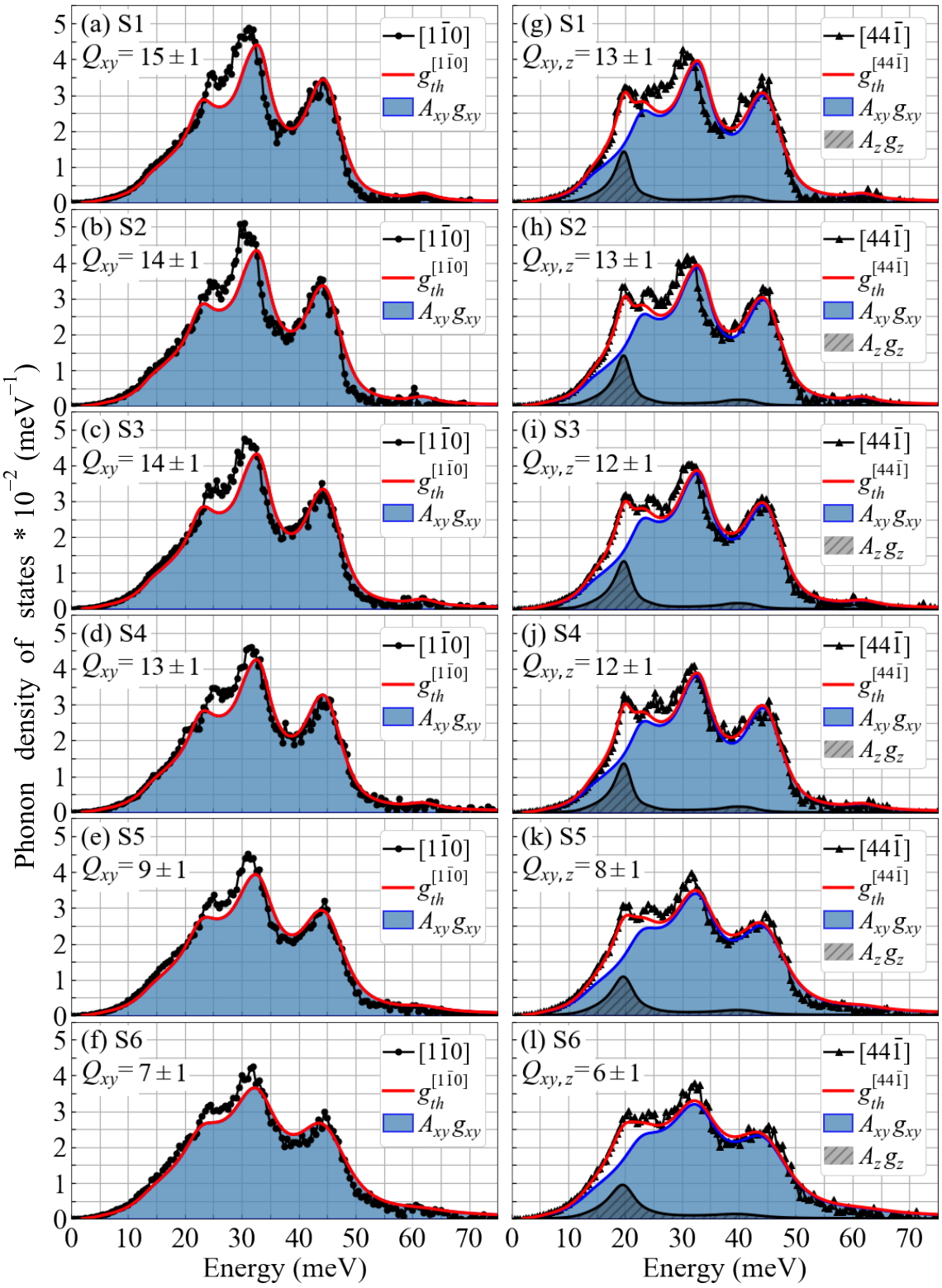

Figure 6.7: Fe-partial PDOS of the indicated samples measured (a) - (f) along α-$FeSi_2[1\bar{1}0]$ and (g) - (l) along α-$FeSi_2[44\bar{1}]$. The experimental data (symbols) is compared with the results of the least squares fit (solid red line), decomposed into its weighted *xy* ($A_{xy}\,g_{xy}$) and *z* ($A_z\,g_z$) contributions (for details see text). The corresponding quality factors Q_{xy} and $Q_{xy,z}$ are given as well.

and $c = 5.14\,\text{Å}$. For the measurement along α-$FeSi_2[44\bar{1}]$ the following applies:

$$\boldsymbol{\kappa}_{[44\bar{1}]} = \frac{1}{\sqrt{32a^2 + c^2}}(4a, 4a, c), \tag{6.1}$$

and the relative contributions of x-, y-, and z-polarized phonons are given by:

$$\begin{aligned} A_x^{[44\bar{1}]} &= (\kappa_{[44\bar{1}]}^x)^2 = \frac{(4a)^2}{32a^2 + c^2} = 0.449, \\ A_y^{[44\bar{1}]} &= (\kappa_{[44\bar{1}]}^y)^2 = \frac{(4a)^2}{32a^2 + c^2} = 0.449, \\ A_z^{[44\bar{1}]} &= (\kappa_{[44\bar{1}]}^z)^2 = \frac{c^2}{32a^2 + c^2} = 0.102. \end{aligned} \tag{6.2}$$

For the tetragonal α-$FeSi_2$ the PDOS of x- and y-polarized vibrations are equal $[g_x(E) = g_y(E)]$ and the relative weights of xy- and z-polarized vibrations are given by $A_{xy}^{[44\bar{1}]} = 0.9$ and $A_z^{[44\bar{1}]} = 0.1$. Application of the same procedure to the spectra obtained along α-$FeSi_2[1\bar{1}0]$ leads to $A_x^{[1\bar{1}0]} = A_y^{[1\bar{1}0]} = 0.5$ and $A_z^{[1\bar{1}0]} = 0$. Therefore, the observed vibrational anisotropy can be explained by the specific orientation of the α-$FeSi_2$ unit cell on the Si(110) surface, which excludes z-polarized vibrations along the nanowires, whereas across the nanowires a 10 % contribution of the z-polarized vibrations to the overall PDOS is present.

The second prominent effect observed in Figure 6.7 is a damping of the PDOS features as the average nanowire width $\bar{w}$ is reduced from 24 nm in S1 to 3 nm in S6. This effect can be described by convolution of the *ab initio* calculated PDOS with the DHO function. By modeling the experimental PDOS with this approach, the strength of the damping is quantified by the quality factor Q. The $g_{xy}(E)$ and $g_z(E)$ used for the modeling were calculated under consideration of the experimental resolution each sample was measured with, as described in Section 5.2. The PDOS obtained along α-$FeSi_2[1\bar{1}0]$, i.e. along the nanowire orientation, consists of xy-polarized vibrations only and the experimental data can be described by:

$$g_{th}^{[1\bar{1}0]} = g_{xy}(E, Q_{xy}), \tag{6.3}$$

with $g_{xy}(E, Q_{xy})$ being the *ab initio* calculated xy-polarized Fe-partial PDOS convoluted with the DHO function characterized by a quality factor Q_{xy}. The comparison of the experimental data with $g_{th}^{[1\bar{1}0]}$ in Figure 6.7(a) - 6.7(f) shows a very good agreement. The damping is clearly reflected in the Q_{xy} values, which continuously decrease from S1 - S6. The high-energy part of the PDOS is very well reproduced by the theory, while the minor peak around 25 meV is shifted by 1.5 meV to lower energy and the peak around 33 meV is shifted by about 1 meV to higher energy in the *ab initio* calculated PDOS. The different epitaxial strain along and across the nanowires and the tilting of the unit cell with respect to the Si(110) surface most likely result in a complex deformation of the α-$FeSi_2$ unit cell, which is not fully accounted for in the *ab initio* calculations performed for an isotropically strained crystal. Therefore, the observed differences are attributed to a more complex strain distribution in the nanowires than the assumed isotropic 0.5 % tensile strain.

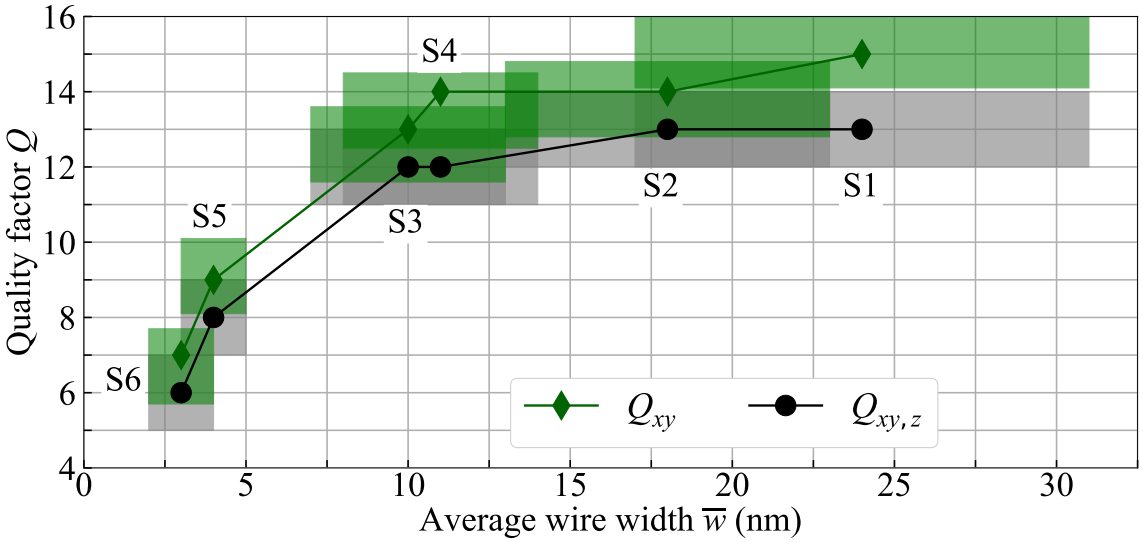

Figure 6.8: Quality factors Q_{xy} and $Q_{xy,z}$ (Fig. 6.7) as a function of average nanowire width $\bar{w}$ (Table 6.1). The shaded boxes denote the errors of Q_{xy}, $Q_{xy,z}$, and $\bar{w}$.

Across the nanowires, contributions of xy- and z-polarized vibrations are present and the PDOS obtained along α-$FeSi_2[44\bar{1}]$ has to be modeled by the weighted sum of the *ab initio* calculated xy- and z-polarized PDOS, convoluted with the DHO function with a quality factor $Q_{xy,z}$:

$$g_{th}^{[44\bar{1}]} = A_{xy}^{[44\bar{1}]} g_{xy}(E, Q_{xy,z}) + A_z^{[44\bar{1}]} g_z(E, Q_{xy,z}). \tag{6.4}$$

In Figure 6.7(g) - 6.7(l) $g_{th}^{[44\bar{1}]}$ is plotted together with the respective xy- ($A_{xy}g_{xy}$) and z- ($A_z g_z$) contributions, as well as the corresponding $Q_{xy,z}$ values obtained from the fit. The contribution of the z-polarized vibrations around 20 meV is well reproduced by the *ab initio* calculations. For the xy-polarized vibrations a very good agreement is achieved for the high-energy part of the PDOS, while the peaks at 25 and 33 meV exhibit small shifts between theory and experiment, which are also present in the measurements along α-$FeSi_2[1\bar{1}0]$ and are attributed to a complex strain distribution. Furthermore, the $Q_{xy,z}$ values continuously decrease as the average nanowire width is reduced from S1 - S6. The $Q_{xy,z}$ values are reduced by 10 %, on average, compared to the Q_{xy} values obtained for the PDOS along the nanowires. The reason for the slightly stronger damping of the phonons propagating across the nanowires could be the smaller size of the α-$FeSi_2$ crystal along this direction. The experimental data was additionally modeled with A_{xy} and A_z being free parameters in the least squares optimization. The quality factors obtained with this approach coincide within the uncertainty with the values given in Figure 6.7, A_{xy} and A_z deviate at most by 2 % from the calculated values of A_{xy}=0.9 and A_z=0.1.

The quality factors obtained from the least squares fits for S1 - S6 by $g_{th}^{[1\bar{1}0]}$ and $g_{th}^{[44\bar{1}]}$ are plotted as a function of the average nanowire width $\bar{w}$ in Figure 6.8. The Q_{xy} and $Q_{xy,z}$ values only show a slight decrease in the $\bar{w}$ range from 24 nm to 10 nm, whereas upon reduction of $\bar{w}$ below 10 nm Q_{xy} and $Q_{xy,z}$ are significantly reduced. This trend can be understood by consideration of the interface-to-volume ratio of the

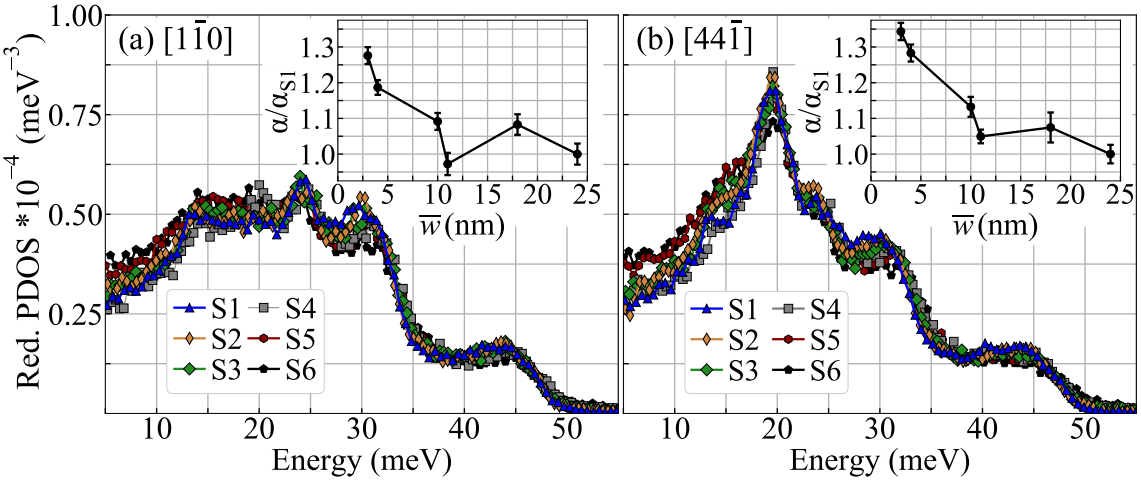

Figure 6.9: Fe-partial reduced PDOS $[g(E)/E^2]$ of the indicated samples obtained along (a) α-$FeSi_2$[1$\bar{1}$0] and (b) α-$FeSi_2$[44$\bar{1}$]. The insets show the coefficient α obtained from $g(E) = \alpha E^2$ in the range of 5 - 10 meV as a function of average island height, normalized to the value of α_{S1}.

nanowires. In the volume part, i.e. the core of the nanowires, the atoms are located in a bulk-like environment with a high degree of crystalline order. At the interfaces towards the substrate and the capping layer, on the other hand, an intrinsic degree of disorder is present and thus the scattering of phonons at defects is enhanced. A reduction of the average nanowire width below 10 nm leads to a significant increase of the interface-to-volume ratio, and consequently, a distinct reduction of Q_{xy} and $Q_{xy,z}$ is observed in Figure 6.8.

The investigation of α-$FeSi_2$ nanostructures on Si(111) revealed a polarization-dependence of the phonon damping, i.e. below an average island height of 10 nm a stronger damping of z-polarized phonons is present. To examine if this effect is also present in the nanowires, the PDOS obtained along α-$FeSi_2$[44$\bar{1}$] were fitted by the weighted sum of the *ab initio* calculated xy- and z-polarized PDOS convoluted with DHO functions with independent quality factors Q_{xy} and Q_z. Although the results indicate that a polarization dependence might also be present in S5 and S6, the low intensity of the peak of the z-polarized phonons at 20 meV does not allow for a definite conclusion.

In Figure 6.9 the reduced PDOS $[g(E)/E^2]$ of S1 - S6 obtained along α-$FeSi_2$[1$\bar{1}$0] and α-$FeSi_2$[44$\bar{1}$] is presented. Along both directions no systematic increase of low-energy states is observed with reduction of $\bar{w}$ from 24 nm (S1) to 10 nm (S3), while the further reduction of $\bar{w}$ in S5 and S6 leads to a distinct increase. This is emphasized in the insets in Figure 6.9, which show the α values obtained from $g(E) = \alpha E^2$ in the range of 5 - 10 meV as a function of $\bar{w}$, normalized to the value obtained for S1. The low-energy enhancement can be attributed to interface-specific vibrational modes, which are more pronounced in the smaller nanowires of S5 and S6. Compared to the results discussed in Chapter 4 and Chapter 5, the increase of the number of low-energy states is relatively small. This can be explained by the lower interface-to-volume ratio of the nanowires compared to the 2D nanostructures, which results in a lower relative contribution of atoms located at interfaces and surfaces.

A comparison of the PDOS and reduced PDOS of the capped and uncapped nanowires of S3 and S4 shows only minor deviations and a significant influence of the capping layer on the lattice vibrations can be excluded. This is attributed to the endotaxial growth, which results in a large interface/volume ratio compared to the surface/volume ratio of the nanowires and a negligible contribution of surface-specific vibrational modes.

6.3. Thermodynamic and elastic properties

The thermodynamic and elastic properties obtained from the direction-projected *ab initio* calculated PDOS and experimentally determined PDOS of S1 - S6 are given in Table 6.3. The theoretical results show that the contribution of low-energy z-polarized phonons along α-$FeSi_2[44\bar{1}]$ leads to a reduction of the mean force constant F and a significant increase of the vibrational entropy S_V compared to α-$FeSi_2[1\bar{1}0]$. Except for the F values of S1, this trend is also reflected in the experimental values. The *ab initio* calculations, performed for a bulk crystal, predict an isotropic mean square displacement $\langle x^2 \rangle$, whereas the experimental results show a systematic increase of $\langle x^2 \rangle$ along $[44\bar{1}]$ due to the smaller size of the α-$FeSi_2$ crystal across the nanowires. The experimental $\langle x^2 \rangle$ values are increased by 8 %, on average, compared

Table 6.3: Fe-partial mean force constant F, mean square displacement $\langle x^2 \rangle$, vibrational entropy S_V, and lattice heat capacity C_V, calculated from the *ab initio* PDOS projected along α-$FeSi_2[1\bar{1}0]$ and α-$FeSi_2[44\bar{1}]$ and the experimental PDOS of S1 - S6 measured along α-$FeSi_2[1\bar{1}0]$ and α-$FeSi_2[44\bar{1}]$. The coefficient α derived from the low-energy part of the PDOS [$g(E) = \alpha E^2$] and the sound velocity v_S are also given.

	F (N/m)	$\langle x^2 \rangle$ (10^{-2}Å^2)	S_V $(k_B/at.)$	C_V $(k_B/at.)$	α $(10^{-5} meV^{-3})$	v_S (m/s)
theo. $[1\bar{1}0]$	254(5)	0.96(2)	2.62(2)	2.60(2)	-	4988
theo. $[44\bar{1}]$	245(5)	0.96(2)	2.68(2)	2.61(2)	-	-
S1 $[1\bar{1}0]$	249(5)	1.00(2)	2.69(2)	2.61(2)	3.20(4)	4700(50)
S1 $[44\bar{1}]$	245(5)	1.04(2)	2.74(2)	2.62(2)	3.03(7)	4780(100)
S2 $[1\bar{1}0]$	250(5)	1.01(2)	2.67(2)	2.60(2)	3.51(7)	4550(100)
S2 $[44\bar{1}]$	245(5)	1.05(2)	2.73(2)	2.61(2)	3.24(8)	4670(120)
S3 $[1\bar{1}0]$	248(5)	1.01(2)	2.67(2)	2.60(2)	3.38(6)	4600 (80)
S3 $[44\bar{1}]$	247(5)	1.05(2)	2.72(2)	2.61(2)	3.37(7)	4610(100)
S4 $[1\bar{1}0]$	256(5)	0.96(2)	2.64(2)	2.59(2)	3.01(9)	4780(140)
S4 $[44\bar{1}]$	251(5)	1.02(2)	2.69(2)	2.59(2)	3.13(4)	4730(60)
S5 $[1\bar{1}0]$	259(5)	1.04(2)	2.66(2)	2.59(2)	3.69(4)	4480(50)
S5 $[44\bar{1}]$	250(5)	1.10(2)	2.74(2)	2.60(2)	3.82(5)	4420(60)
S6 $[1\bar{1}0]$	255(5)	1.05(2)	2.68(2)	2.59(2)	3.96(5)	4370(60)
S6 $[44\bar{1}]$	255(5)	1.10(2)	2.71(2)	2.60(2)	4.00(5)	4360(60)

to the theoretical values. This is attributed to the increased amplitude of atomic vibrations at interfaces, which are not considered in the first-principles calculations. The values of the lattice heat capacity C_V coincide within the uncertainty for S1 - S6 with the theory along both directions. The reduction of $\bar{w}$ from S1 - S6 leads to an increase of $\langle x^2 \rangle$ by 5 % along $[1\bar{1}0]$ and by 5.8 % along $[44\bar{1}]$. This is in accordance with the trend observed in the σ^2 values obtained for the Fe-Si scattering path by modeling the EXAFS data (see Table 6.2). Also F is slightly increased from S1 to S6, most likely due to the additional high-energy states above the cutoff energy, which are induced by the broadening of the peak at 45 meV.

Furthermore, the absolute values of the coefficient α obtained from $g(E) = \alpha E^2$ are given, together with the corresponding sound velocity v_S. For comparison, the theoretical value for $[1\bar{1}0]$, determined from the slopes of the three acoustic branches in the phonon dispersion relations along Γ-M direction, is also given. The experimental values are clearly reduced compared to the theoretical value. Reason for these differences is that a perfect crystal is assumed for the *ab initio* calculations, whereas in the nanowires the propagation of sound waves is decelerated by scattering at defects, which are primarily present at interfaces. Since the interface-to-volume ratio is increased when the nanowires dimensions are reduced, v_S is also reduced by 9 % from S1 - S6.

6.4. Conclusions

Endotaxial $FeSi_2$ nanowires were grown on the Si(110) surface by reactive deposition epitaxy. A systematic RHEED study revealed the formation of single-crystalline, uniaxially aligned nanowires. The nanowire dimensions were determined by AFM, the average width ranges from 24 nm to 3 nm, the length from several µm to about 100 nm. The local crystal structure of the nanowires was investigated by a combined experimental and theoretical EXAFS study. The results unveil the formation of α-$FeSi_2$ and resolve the controversy about the crystal phase of $FeSi_2$ nanowires grown on Si(110). In conjunction with previous reports on the epitaxial relation between Si(111) and Si(001) surfaces and α-$FeSi_2$, these results enabled the determination of the epitaxial relation between the Si(110) surface and the α-$FeSi_2$ unit cell of the nanowires.

The Fe-partial PDOS of lattice vibrations along and across the nanowires was obtained by NIS experiments. A pronounced vibrational anisotropy was observed, which is comprehensively understood by consideration of the specific orientation of the tetragonal α-$FeSi_2$ unit cell on the Si(110) surface. Furthermore, a broadening of the PDOS features was evidenced upon reduction of the average nanowire width from 24 nm to 3 nm. The strength of the damping was quantified by modeling of the experimental data with first-principles calculations. The good accordance between theory and experiments allowed to attribute the damping to phonon scattering at the nanowire/substrate interface, which is particularly strong in the smallest nanowires characterized with the highest interface-to-volume ratio. Furthermore, the reduction of the average nanowire width from 24 nm to 3 nm leads to an increase of the mean square displacement by 5 % and a reduction of the sound velocity by 9 %. A

slightly stronger damping of vibrations across the nanowires results from the smaller size of the α-$FeSi_2$ crystal along this direction. A polarization-dependence of the observed damping effects is indicated in the smallest nanowires, but the low contribution of z-polarized phonons to the overall PDOS does not allow for a definite conclusion. Comparison of the PDOS of samples with identical average nanowire sizes, measured with and without a capping layer, demonstrated that the influence of surface-specific vibrational modes is negligible due to the endotaxial character of the nanowires.

Previous reports on endotaxial nanowires grown with different silicide compounds revealed close macroscopic structural similarities. Therefore, the results obtained here for the lattice dynamics and thermoelastic properties of α-$FeSi_2$ nanowires are expected to be generally valid for the technologically important class of endotaxial silicide nanowires.

7. Lattice dynamics of β-phase $FeSi_2$ nanorods

The variety of proposed applications of β-phase $FeSi_2$, e.g. in optoelectronics [41], photovoltaics [44, 45], and thermoelectrics [46, 214], also initiated the investigation of the lattice dynamics of this compound by theoretical [157, 159] and combined NIS and *ab initio* [160] studies. Due to the challenges imposed by the inherently small scattering volume of nanostructures, however, the effect of nanostructurization on the lattice dynamics of β-$FeSi_2$ has not been investigated hitherto.

For many of the foreseen device applications, the direct implementation of self-assembled β-$FeSi_2$ nanostructures on silicon surfaces is advantageous. The growth of high-aspect-ratio nanowires has thoroughly been investigated for α-$FeSi_2$ on Si(110) (see Chapter 6), while the formation of similar one-dimensional nanostructures of β-$FeSi_2$ is opposed by fundamental obstacles. It was shown that the growth of β-$FeSi_2$ on silicon substrates is closely related to the surface orientation and that the growth rate is the lowest on the Si(110) surface [215]. Furthermore, the large lattice mismatch between β-$FeSi_2$ and Si(110) results in the formation of metastable, lattice matched phases at low growth temperatures, e.g. *s*-, γ-, and α-$FeSi_2$. The transformation of these precursor phases to β-$FeSi_2$ can be achieved by solid phase epitaxy, i.e. annealing at elevated temperatures for a certain amount of time [151, 155]. The inherently large surface/interface-to-volume ratio of one-dimensional nanostructures, however, results in a reduction of the surface and interface energy by fragmentation of the nanostructures at elevated temperatures [216–218]. The theoretical basis for the description of this effect was given in 1878 by Lord Rayleigh, who observed the formation of droplets after inducing disturbances on a liquid jet [219]. At high growth temperatures the supplied energy is large enough to directly form large-lattice-mismatch β-phase $FeSi_2$ nanostructures, but the increased surface mobility leads to the formation of compact nanostructures with low surface-to-volume ratios. Therefore, the investigation of the lattice dynamics of β-$FeSi_2$ nanostructures presented in the following chapter is focused on low-aspect-ratio nanorods.

The growth and characterization of a bulk-like β-$FeSi_2$ film and β-$FeSi_2$ nanorods are presented, followed by a discussion of the lattice dynamics of these structures. The chapter is concluded with the thermodynamic and elastic properties of the investigated β-$FeSi_2$ nanostructures.

7.1. Sample preparation and characterization

The samples were grown in the UHV-Analysis lab at KIT in the MBE system shown in Figure 2.4. The Si(111) and Si(110) substrates were degassed in UHV at 650 °C

Table 7.1: Overview of the investigated samples. θ_{Fe} stands for the deposited amount of ^{57}Fe, T_G for the growth temperature, T_A for the annealing temperature and t_A for the annealing time. The last column denotes if the sample was capped with Si or measured *in situ* during the NIS experiment.

Sample	Substrate	θ_{Fe} [Å]	θ_{Fe} [ML]	T_G [°C]	T_A [°C]	t_A [min]	NIS exp.
S1	Si(111)	50 (5)	130(13)	100(10)	700(10)	10	Si cap
S2	Si(110)	1.7(2)	3.0(3)	600(10)	750(10)	120	*in situ*
S3	Si(110)	0.6(1)	1.1(1)	600(10)	750(10)	180	Si cap
S4	Si(110)	1.7(2)	3.0(3)	600(10)	750(10)	240	Si cap

for 4 h, followed by the removal of the native SiO_2 layer by heating two times to 1250 °C for 30 seconds. The growth of the investigated nanostructures was conducted in two stages. Precursor structures were grown by deposition of a certain amount θ_{Fe} of high purity iron, enriched to 96 % in the Mössbauer-active isotope ^{57}Fe, onto the substrate surface, stabilized at the growth temperature T_G. The coverage was controlled by a quartz oscillator with an accuracy of 10 % and is given in Å and monolayer (ML) units. The given θ_{Fe} in Å corresponds to the thickness of an imaginary continuous Fe layer on the Si surface, whereas 1 ML $\hat{=}$ one Fe atom per 1×1 Si(111)/Si(110) surface mesh [153]. Subsequently, the precursor structures were annealed at the temperature T_A for the time t_A. This process is known as *solid phase epitaxy* and is commonly applied for the growth of bulk β-$FeSi_2$ layers on Si(111) (e.g. [220, 221]) and has also been reported for the growth of β-$FeSi_2$ nanostructures on Si(110) [151, 155]. The growth and annealing were conducted under UHV conditions with $P < 1\times10^{-8}$ Pa. Details of the growth and experimental conditions used for the investigated samples, hereinafter referred to as S1 - S4, are summarized in Table 7.1. After the structural characterization with RHEED and AFM, S1, S3, and S4 were capped with 4 nm of amorphous Si deposited following the conditions described in Chapter 5. All measurements described within this chapter were conducted at room temperature.

In Figure 7.1 the results of the RHEED study, obtained before growth, after growth of the precursor structure, and after the annealing process, are shown. For S1 a 7×7 reconstructed Si(111) surface is confirmed after removal of the native oxide layer [Fig. 7.1(a)]. The diffraction pattern obtained after deposition of 50 Å Fe at a relatively low temperature of $T_G = 100°$ C [Fig. 7.1(e)] corresponds to a crystalline Fe(111) surface [168, 222, 223]. The semicircles observed after the annealing [Fig. 7.1(i)] indicate a polycrystalline film, while the faint streaks are very similar to the Si(111) surface reflections and indicate the formation of an intermittent film. For S2 - S4 a 16×2 reconstructed Si(110) surface is observed [207] prior to growth of the precursor structures. The images obtained for S3 and S4 are blurred to a certain degree due to technical problems with the RHEED device. From the results presented in Chapter 6, the formation of uniaxially aligned, epitaxial α-$FeSi_2$ nanowires is expected for the growth conditions used for S2 - S4. This is confirmed by the RHEED images shown in Figure 7.1(f) - 7.1(h), which exhibit strait streaks

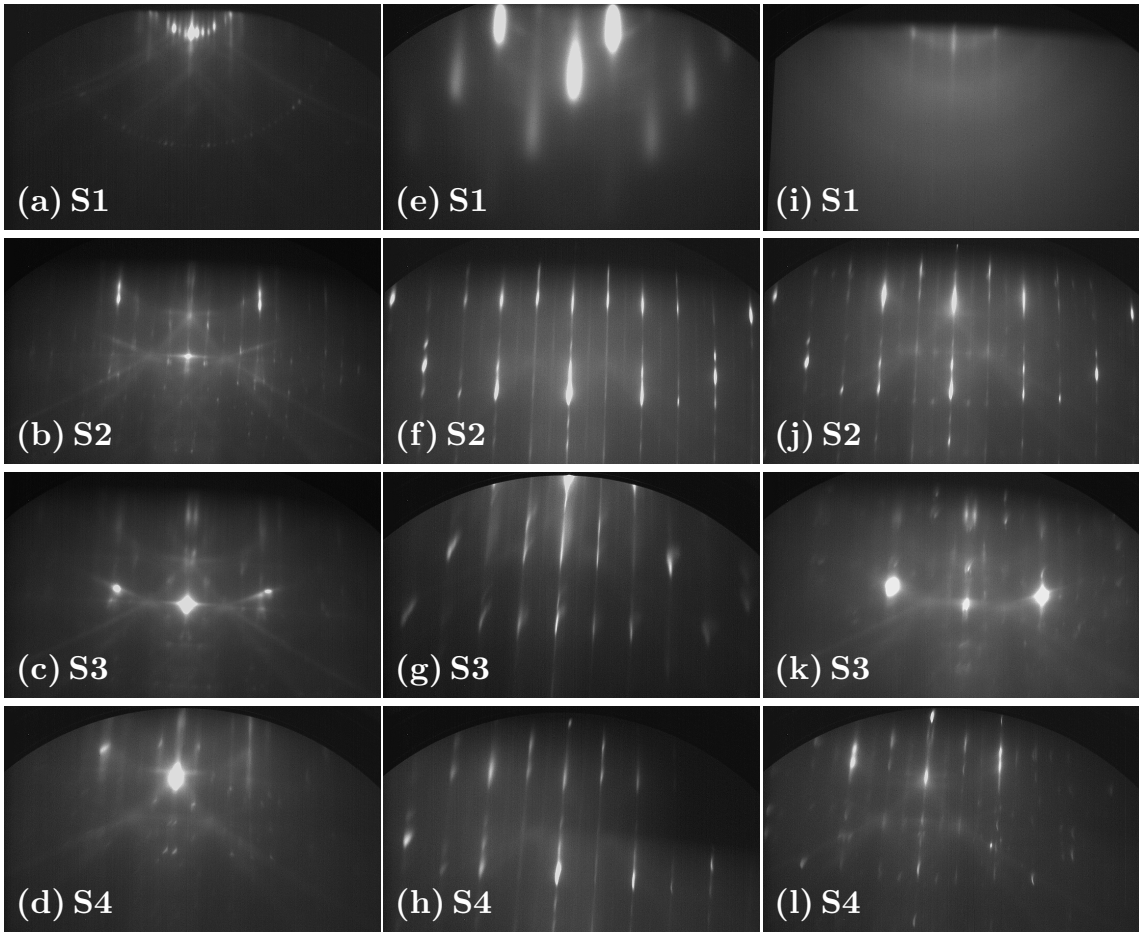

Figure 7.1: RHEED patterns of the indicated samples obtained with E = 28 keV (a) - (d) before growth, (e) - (h) after growth, and (i) - (l) after annealing. The images were measured along the Si$\langle\bar{1}10\rangle$ direction of the Si(111) surface for S1 and along the Si$\langle001\rangle$ direction of the Si(110) surface for S2 - S4.

with superimposed diffraction spots, i.e. the typical diffraction pattern of densely packed α-$FeSi_2$ nanowires (compare with Fig. 6.2). After the annealing of S2, the diffraction spots observed after growth reoccur together with new reflections, while the intensity of the streaks is reduced. For S3, the diffraction pattern obtained after the annealing is very similar to the Si(110) surface before growth, indicating the formation of well separated nanostructures. Also in case of S4 the diffraction pattern of the Si(110) surface reoccurs, however, additional spots at similar positions as observed for S2 are present.

The crystal structure of the bulk sample S1 was investigated after deposition of the Si capping layer by x-ray diffraction (XRD) with a Rigaku Smart-Lab instrument with a rotating Cu anode x-ray generator. The θ-2θ overview scan presented in Figure 7.2 shows the Si(111) and Si(222) substrate reflections together with various β-$FeSi_2$ reflections, as previously reported for the growth of polycrystalline films on Si(111) (e.g. [160, 220, 224]). The very similar lattice parameters b and c of the orthorhombic β-$FeSi_2$ unit cell imply that a reflection with Miller indices (hkl)

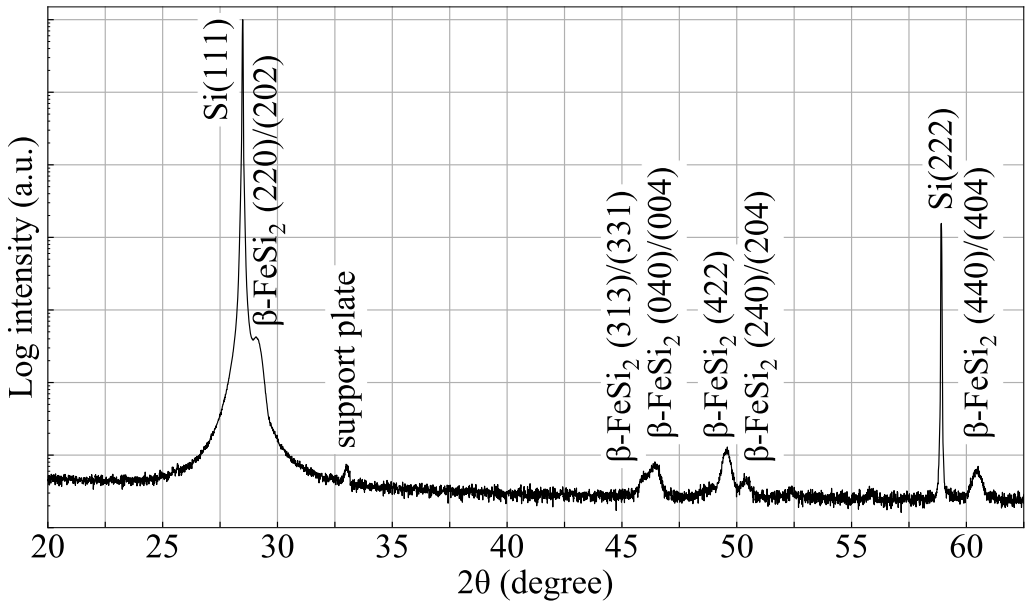

Figure 7.2: Wide range θ-2θ XRD scan of S1, measured with Cu K_α radiation.

occurs at approximately the same angular position as a (*hlk*) reflection, i.e. the β-$FeSi_2$(220) reflection for instance cannot be distinguished from the β-$FeSi_2$(202) reflection in the θ-2θ scan. A scan without a sample revealed that the additional peak at 33 ° originates from the support plate installed in the instrument.

The crystal structure of S3 and S4 was determined by a comparative x-ray absorption spectroscopy study, using S1 as a β-$FeSi_2$ reference sample. The experiments were conducted *ex situ*, i.e. after capping of the samples with 4 nm of amorphous Si, at the SUL-X beamline of the synchrotron radiation source KARA at KIT. In Figure 7.3 the corresponding XAFS spectra (taken at the Fe *K*-edge at 7112 eV), EXAFS spectra and EXAFS Fourier transforms are presented. The XAFS and EXAFS spectra of S3 and S4 are compared with the bulk β-$FeSi_2$ film of S1 (blue dotted line), the respective EXAFS Fourier transforms are additionally compared to a typical result obtained for α-$FeSi_2$ nanostructures (red dotted line). The comparison shows that the positions of the XAFS and EXAFS oscillations as well as the EXAFS Fourier transforms are in very good accordance for S1, S3, and S4. On the contrary, the Fourier transform obtained for α-$FeSi_2$ nanostructures exhibits clear deviations. The theoretically predicted interatomic distances of the first and second coordination sphere of β-$FeSi_2$ are 2.36 Å for the Fe-Si and 2.97 Å for the Fe-Fe scattering path. For α-$FeSi_2$ the corresponding values are 2.36 Å for the Fe-Si and 2.70 Å for the Fe-Fe scattering path. In the Fourier transforms depicted in Figure 7.3(g) - 7.3(i) the intense peak at a radial distance of about 2 Å can be assigned to the Fe-Si scattering path, whereas the peak between 2.5 - 3 Å can be assigned to the Fe-Fe scattering path. Comparison of the Fourier transforms of S3 and S4 with the result obtained for α-$FeSi_2$ nanostructures shows that the larger interatomic distance in the Fe-Fe scattering path of β-$FeSi_2$ is clearly reflected in S3 and S4 and a complete transformation of the α-$FeSi_2$ precursor structures into β-$FeSi_2$ is confirmed.

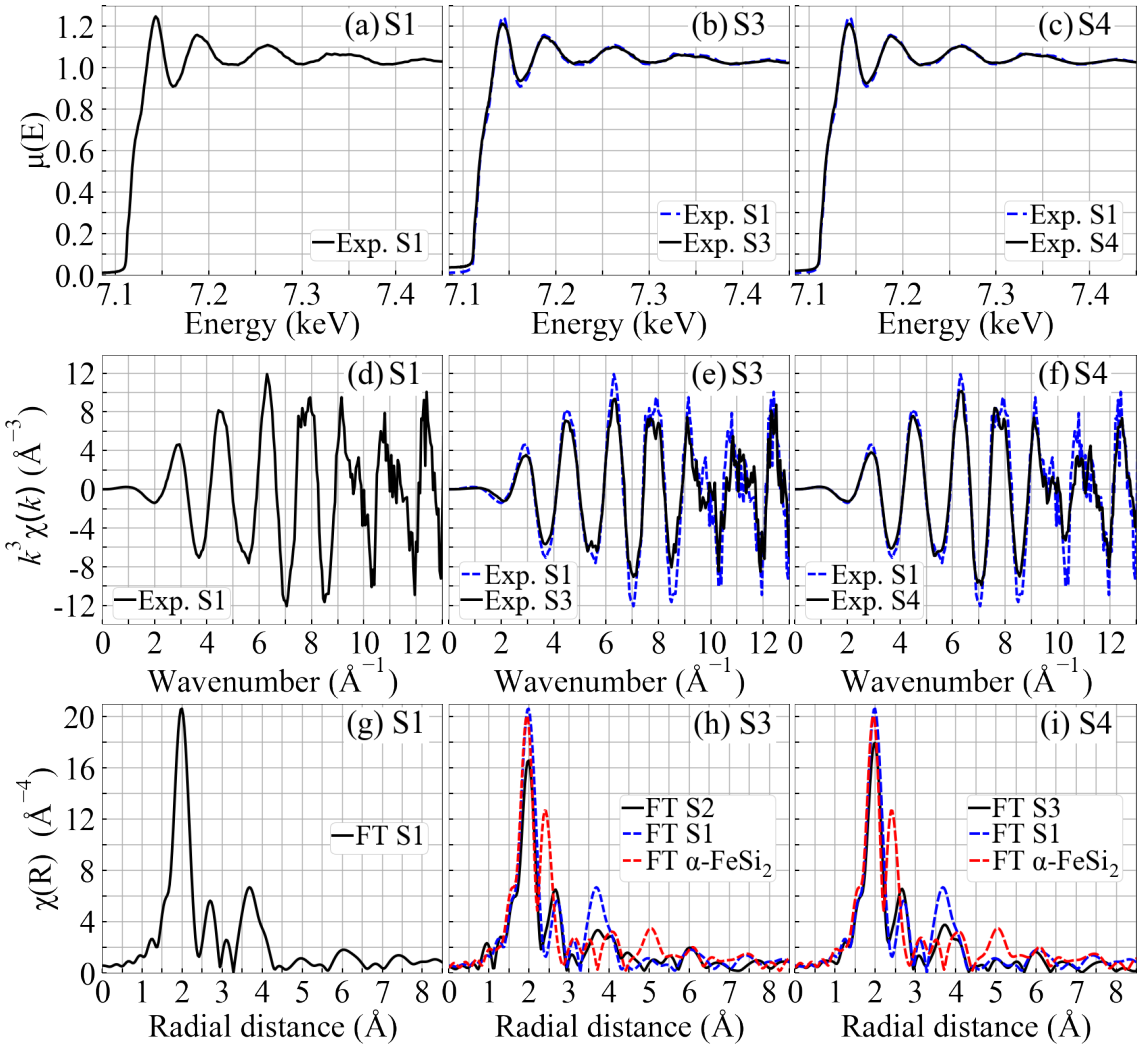

Figure 7.3: (a) - (c) Normalized Fe K-edge XAFS spectra of S1, S3, and S4. (d) - (f) Fe K-edge EXAFS spectra of S1, S3, and S4. The spectra are weighted with k^3 for amplification of the oscillations at higher k values. (g) - (i) Fourier transforms (FT) of the EXAFS spectra shown in (d) - (f). Samples S3 and S4 are compared with the respective results obtained for α-$FeSi_2$ nanostructures (red dashed line).

The epitaxial relation between the β-$FeSi_2$ crystal and the Si(111) and Si(110) surfaces is determined by the minimization of the epitaxial strain at the interface. The approximately equal lattice parameters b and c of the orthorhombic β-$FeSi_2$ unit cell result in two crystallographic planes with similarly small deviations from the lattice parameters of the Si(111) surface unit cell, viz. β-$FeSi_2$(101) and β-$FeSi_2$(110). This leads to two possible epitaxial relations [115, 225]: (i) β-$FeSi_2$(101)||Si(111) with β-$FeSi_2$[010]||Si[1$\bar{1}$0] and (ii) β-$FeSi_2$(110)||Si(111) with β-$FeSi_2$[001]||Si[1$\bar{1}$0]. Configuration (i) and (ii) are depicted in Figure 7.4(a) and 7.4(b). The lattice mismatch, defined as $(a_{Si} - a_{FeSi_2})/a_{Si}$, amounts to -1.4 %/-2.6 % along Si[1$\bar{1}$0] and +5.0 %/+5.6 % along Si[$\bar{1}\bar{1}$2] for configuration (i)/(ii), respectively. Due to the threefold symmetry of the Si(111) surface, each configuration can be rotated by 120°, leading to an equivalent epitaxial relation [146]. Thus, a total of six domain

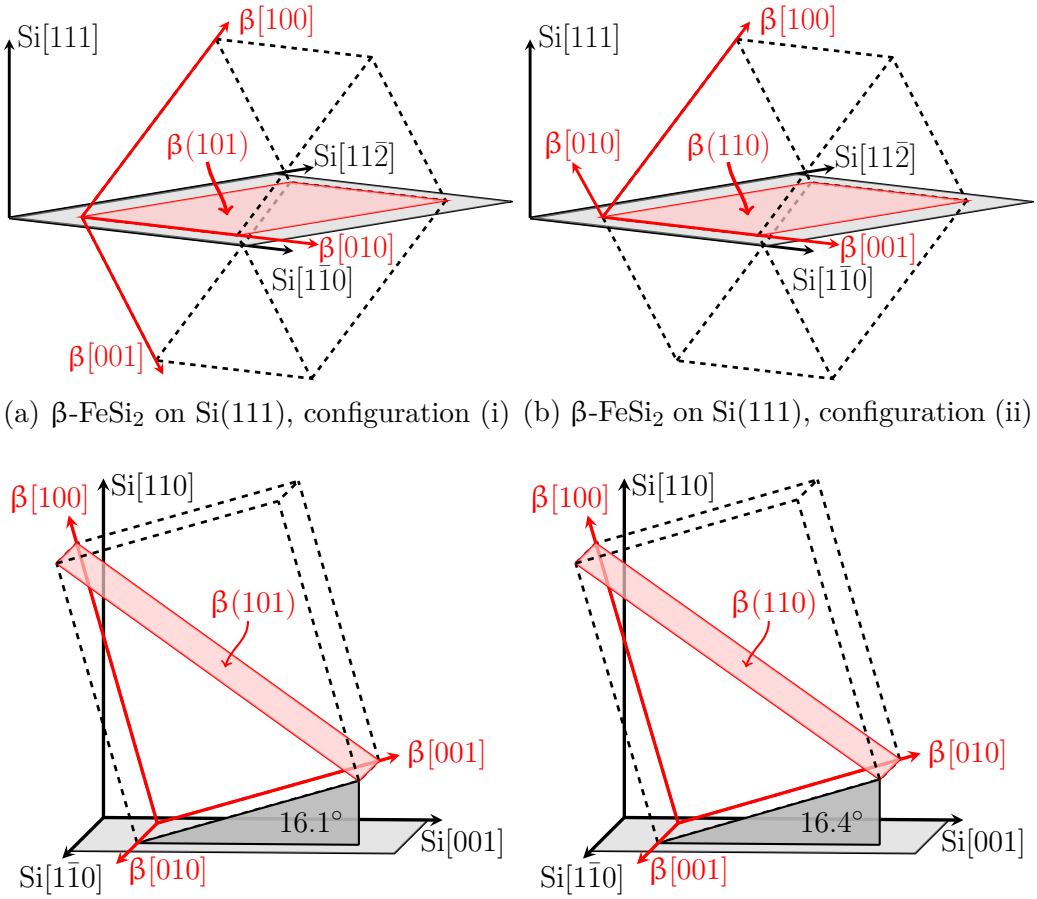

(a) β-$FeSi_2$ on Si(111), configuration (i) (b) β-$FeSi_2$ on Si(111), configuration (ii)

(c) β-$FeSi_2$ on Si(110), configuration (i) (d) β-$FeSi_2$ on Si(110), configuration (ii)

Figure 7.4: Orientation of the β-$FeSi_2$ unit cell on the Si(111) and Si(110) surfaces following the epitaxial relations discussed in the text. The Si (β-$FeSi_2$) directions/planes are given in black/grey (red/light red).

orientations of the β-$FeSi_2$ unit cell on the Si(111) surface are possible. In Figure 7.4(c) and 7.4(d) the orientation of β-$FeSi_2$ unit cell on the Si(110) surface, obtained by translation of the above discussed epitaxial relation, is shown. Due to the lower symmetry of the Si(110) surface the number of possible domain orientations is reduced to the two depicted. The tilt angle between Si[110] and β-$FeSi_2$[100] amounts to 16.1 ° and 16.4 ° for configuration (i) and (ii), respectively. Along Si[1$\bar{1}$0] the lattice mismatch amounts to -1.4 % for configuration (i) and -2.6 % for configuration (ii). Along Si[001], the lattice mismatch is calculated as $(3 \cdot a_{Si} - 2 \cdot a_{FeSi_2})/(3 \cdot a_{Si})$ and amounts to +7.1 % and +8.3 % for configuration (i) and (ii), respectively.

In Figure 7.5 the AFM images obtained for S1 - S4 before capping with the amorphous Si layer are shown. For S1 the formation of an intermittent β-$FeSi_2$ film is evidenced. The average film thickness, measured at different positions as the step height between the uncovered parts of the Si(111) surface and the film surface, amounts to 16.2 nm. This is in good accordance with the theoretically expected thickness of 16.4 nm, which is calculated from the number of deposited Fe atoms per

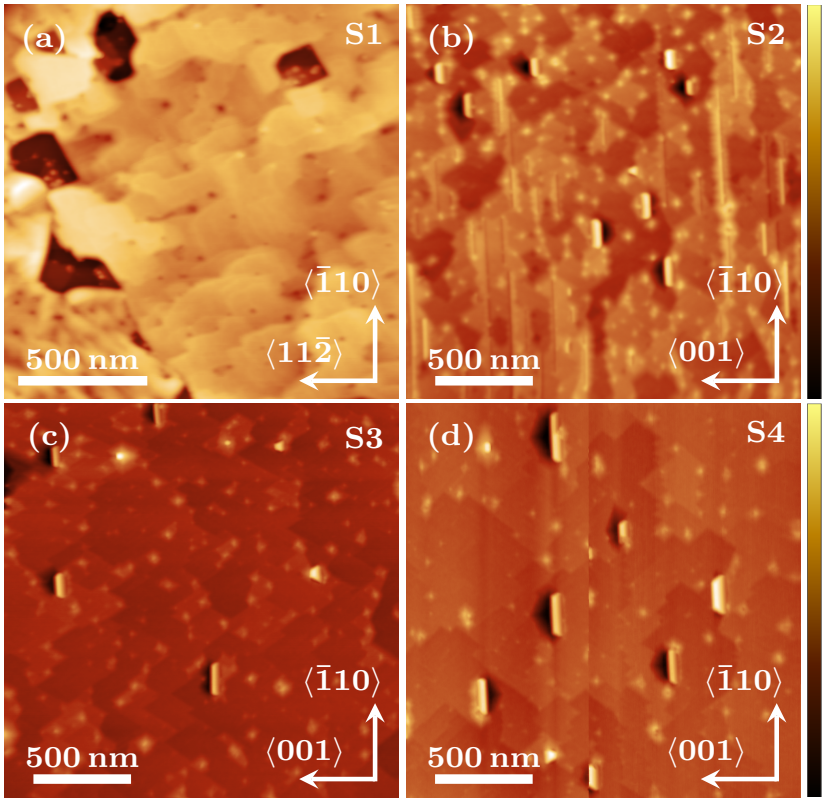

Figure 7.5: AFM images of the indicated samples with height scale (a) 0 - 47 nm, (b) 0 - 26 nm, (c) 0 - 28 nm, and (d) 0 - 29 nm. The color scales depicted on the right apply for all images.

area and the volume of the β-$FeSi_2$ unit cell. In case of S2 a mixture of faint high-aspect-ratio nanowires and shorter and wider nanorods with the same orientation is observed. The transformation of the nanowires to nanorods is accompanied by the formation of a deep trench on one side of the nanorods. The longer annealing time t_A applied for S3 and S4 results in a complete transformation of the nanowires into nanorods. The comparison of S2 and S4 shows that the transformation process takes more than two hours at the chosen annealing temperature of $T_A = 750°$ C. The small pyramidal nanodots, which are scattered over the surfaces and are already present after the nanowire growth (see Fig. 6.5), are still visible after complete transformation of the nanowires into nanorods. The average dimensions of the nanords are given in Table 7.2.

Table 7.2: Overview of the structural properties of the investigated samples.

Sample	substrate	Structure	$\bar{w}$ (nm)	$\bar{h}$ (nm)	$\bar{l}$ (nm)
S1	Si(111)	bulk film	-	16.2	-
S2	Si(110)	rods/wires	46	10	117
S3	Si(110)	nanorods	40	9.5	129
S4	Si(110)	nanorods	52	12	162

7.2. Lattice dynamics

The Fe-partial phonon density of states (PDOS) of S1 - S4 was obtained from nuclear inelastic scattering experiments performed at the Nuclear Resonance Beamline ID18 at the ESRF [91] and the Dynamics Beamline P01 at PETRA III [92]. At both beamlines, the measurements were performed at grazing-incidence geometry with an incidence angle $< 0.2°$ and an x-ray beam with dimensions of 1.5 mm $\times$ 0.01 mm (h $\times$ v, FWHM). The energy resolution at the ^{57}Fe resonance at 14.413 keV was 0.7 meV for S1, S3, and S4 (ID18), and 1.0 meV for S2 (P01). Sample S2 was measured *in situ*, i.e. after growth and characterization with RHEED and AFM it was transported and investigated under UHV conditions in a dedicated UHV chamber [177].

In Figure 7.6 the Fe-partial PDOS of S1, obtained along the orthogonal directions Si$\langle\bar{1}10\rangle$ and Si$\langle11\bar{2}\rangle$ of the Si(111) surface, is shown. Both vibrational spectra are characterized by a pronounced peak at about 36 meV, minor peaks between 40 - 45 meV, and a plateau between 24 - 28 meV. The cutoff energy, above which the number of states goes to zero, is located at 60 meV. The isotropic vibrational behavior can be explained by the results of the RHEED and XRD studies, which revealed a polycrystalline β-$FeSi_2$ film. Thus, the contributions of x-, y-, and z-polarized phonons are on average equal and the obtained PDOS is independent on the wave vector orientation of the x-ray beam with respect to the crystallographic directions. The *ab initio* calculated PDOS of bulk β-$FeSi_2$ is plotted as a red line in Figure 7.6. It is calculated from the absorption probability density of β-$FeSi_2$, convoluted with a Voigt function with FWHM = 0.7 meV, which is equal to the experimental resolution the PDOS of S1 was obtained with. The energy scale of the *ab initio*

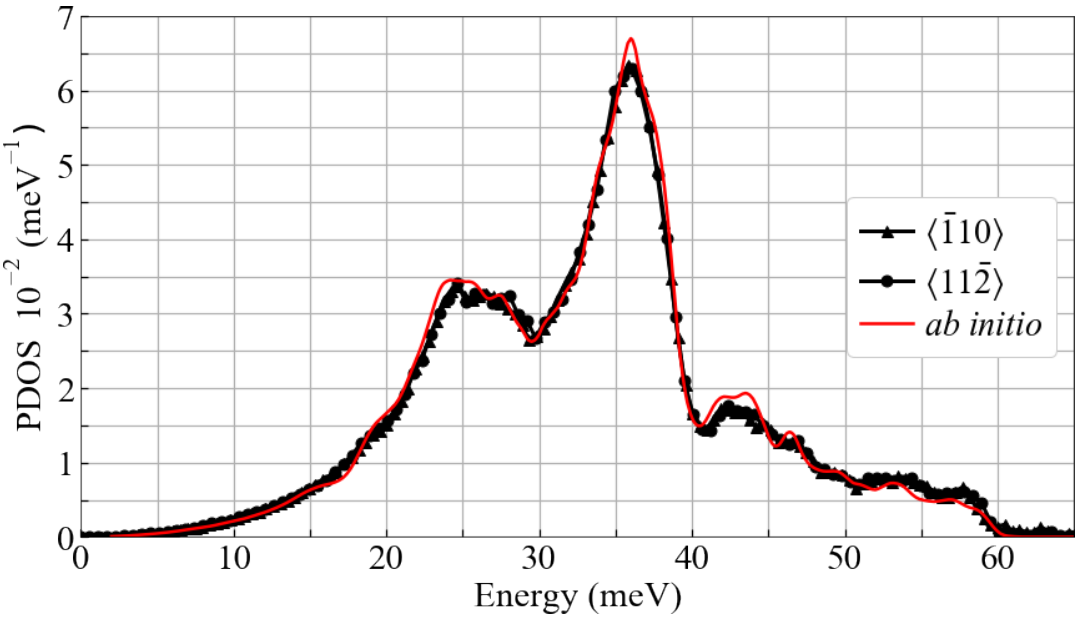

Figure 7.6: Fe-partial phonon density of states of S1 obtained along Si$\langle\bar{1}10\rangle$ and Si$\langle11\bar{2}\rangle$. The red solid line indicates the *ab initio* calculated PDOS of bulk β-$FeSi_2$.

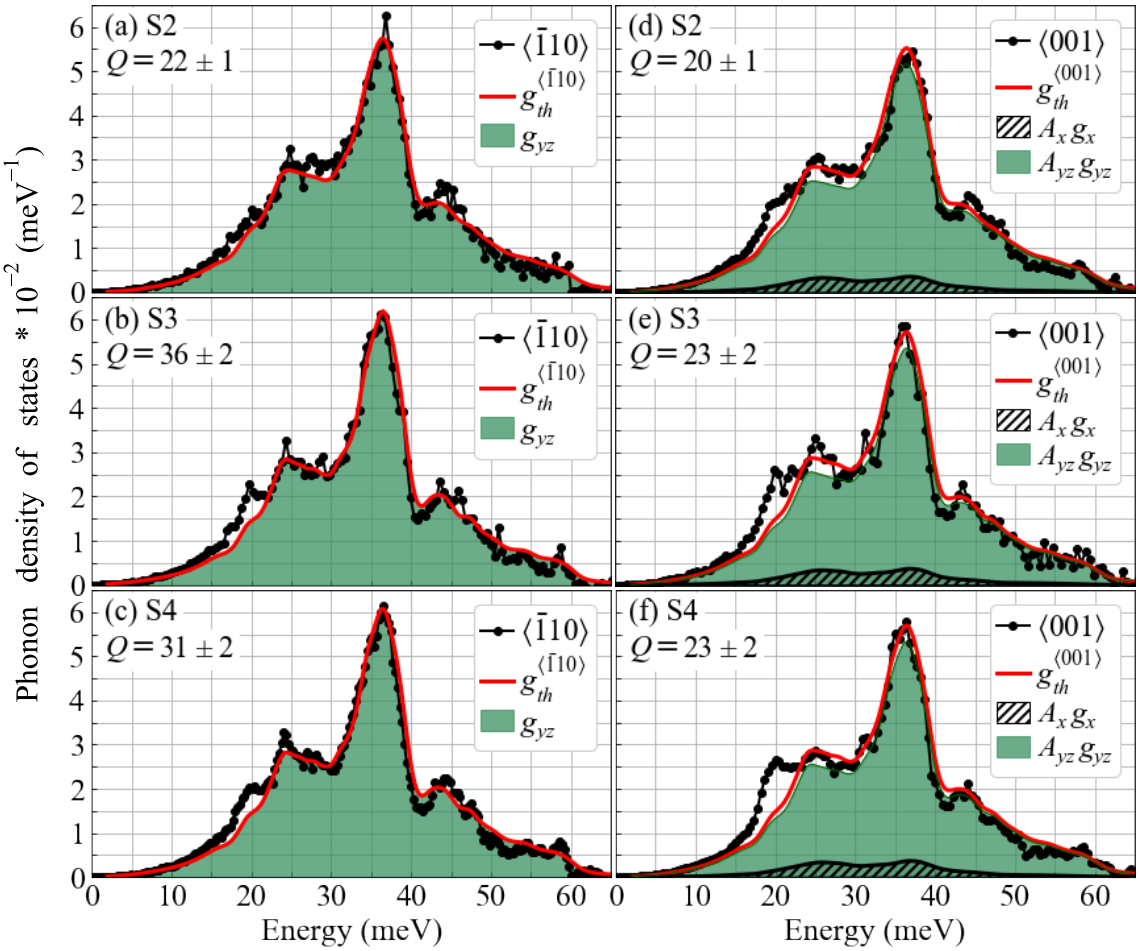

Figure 7.7: Fe-partial PDOS of the indicated samples measured (a) - (c) along Si⟨1̄10⟩ and (d) - (f) along Si⟨001⟩. The experimental data (symbols) is compared with the results of the least squares fit (solid red line), decomposed into its weighted xy ($A_{yz}\, g_{yz}$) and z ($A_x\, g_x$) contributions (for details see text). The resulting quality factors Q are given as well.

PDOS is scaled by a factor of 0.96 to account for the tensile epitaxial strain discussed above. A similar shift between experiment and theory was observed in a polycrystalline, 300 nm thick β-$FeSi_2$ film grown on the Si(001) surface [160]. Including this correction, an outstanding agreement between the *ab initio* calculations and the experiment is observed.

The Fe-partial PDOS of S2 - S4, obtained along Si⟨1̄10⟩ and Si⟨001⟩, is presented in Figure 7.7. All samples reproduce the main features of the bulk β-$FeSi_2$ PDOS, i.e. the main peak at 36 meV, the minor peaks between 40 - 45 meV, as well as the plateau between 24 - 28 meV. The cutoff energies are located at 60 meV. For S2 no detectable contribution of the remaining α-$FeSi_2$ nanowires is present, which would be indicated by an additional peak at 31 meV (compare Fig 6.7).

As discussed in Chapter 5 and Chapter 6, the PDOS obtained along Si⟨1̄10⟩ and Si⟨001⟩ are composed of a specific combination of x-, y-, and z-polarized phonons.

Due to the very similar PDOS of the y- and z-polarization, these contributions are merged and in the following the PDOS is decomposed into x- and yz-polarized phonons. As depicted in Figure 7.4, two different orientations of the β-$FeSi_2$ unit cell are possible on the Si(110) surface. For measurements along Si$\langle\bar{1}10\rangle$, either β-$FeSi_2$[010] or β-$FeSi_2$[001] is parallel to the wave vector of the x-ray beam and thus the corresponding PDOS is expected to be solely composed of yz-polarized phonons. For the measurement along Si$\langle001\rangle$, on the other hand, a contribution of x-polarized phonons is present due to the tilt of the β-$FeSi_2$ unit cell with respect to the Si(110) surface. The contributions for configuration (i) and (ii) can be calculated from the angle between β-$FeSi_2$[100] and Si[001] as $A_x^{(i)} = \cos^2(90° - 16.1°) = 0.077$ and $A_x^{(ii)} = \cos^2(90° - 16.4°) = 0.080$. Thus, the relative weights of the x- and yz-polarized phonons used for the modeling of the PDOS obtained along Si$\langle001\rangle$ are $A_x = 0.08$ and $A_{yz} = 0.92$.

Similarly to the analysis of the α-$FeSi_2$ nanostructures discussed in Chapter 5 and Chapter 6, the effect of enhanced phonon scattering in nanostructures was taken into account by convolution of the *ab initio* calculated PDOS with the DHO function. The experimental spectra obtained along the wires were modeled with the function $g_{th}^{\langle\bar{1}10\rangle}(E, Q)$, which denotes the *ab initio* calculated yz-polarized PDOS of β-$FeSi_2$, convoluted with a DHO function characterized by the quality factor Q. In the same way, the spectra obtained across the nanorods were modeled by $g_{th}^{\langle001\rangle}(E, Q)$, which is a linear combination of x- and yz-polarized phonons weighted by $A_x = 0.08$ and $A_{yz} = 0.92$. The strength of the damping is quantified by Q, which is the only fit parameter in the applied least-squares optimization. The *ab initio* calculated x- and yz-polarized PDOS of β-$FeSi_2$ used for the modeling were obtained under consideration of the experimental resolution each sample was measured with, as described in section 5.2. The tensile epitaxial strain between the Si(110) surface and the β-$FeSi_2$ crystal discussed above was taken into account by scaling the energy of the PDOS by a factor of 0.98. The $g_{th}^{\langle\bar{1}10\rangle}(E, Q)$ and $g_{th}^{\langle001\rangle}(E, Q)$ obtained for the respective samples are presented together with the corresponding Q values in Figure 7.7.

The broadening of the main peak at 36 meV is well reproduced and the obtained Q values are a good parameter for comparison of the strength of the damping along different directions in the investigated samples. The Q values obtained for S2 are significantly lower compared to S3 and S4. This can be explained by the incomplete transformation of the α-$FeSi_2$ nanowires into β-$FeSi_2$ nanorods evidenced by the RHEED and AFM studies in case of S2, which very likely results in a higher degree of disorder in the nanorods of S2 compared to the fully transformed nanorods of S3 and S4. Furthermore, the spectra obtained across the rods exhibit lower Q values, i.e. the phonon scattering is enhanced compared to vibrations along the nanorods. This can be explained by the smaller size of the β-$FeSi_2$ crystal along this direction, although the aspect ratio of the nanorods is relatively small. Another reason for the lower Q values is a shift of phonon states from the main peak to a new vibrational mode emerging at 20 meV, which is significantly more intense in the vibrational spectra across than along the nanorods. For the α-$FeSi_2$ nanowires discussed in Chapter 6 a similar anisotropy was observed. However, the effect observed here is less pronounced in S2, which still contains a certain amount of α-$FeSi_2$

nanowires, than it is in S4 where a complete transformation to β-$FeSi_2$ nanorods is observed. Therefore, residual α-$FeSi_2$ nanowires can be excluded as the origin of the additional mode at 20 meV. From the results obtained for the Fe_3Si/GaAs interface discussed in Chapter 4, it is known that novel, low-energy vibrational modes emerge at interfaces. Similar effects are reported for surface-specific vibrations. Thus, the observed deviations of the nanorod PDOS from its bulk-counterpart could originate from surface and/or interface specific vibrational modes. However, the dimensions of the nanorods determined from the AFM study do not indicate an increase of the interface-to-volume ratio from S2 - S4, whereas the intensity of the peak at 20 meV is significantly increased. In addition, a possible surface contribution would be expected to be the largest in the uncapped rods of S2. An alternative explanation for the additional states at 20 meV is the formation of an iron-rich phase at the interface between the nanorods and the substrate upon prolonged annealing. A similar behavior has been reported for β-$FeSi_2$ nanostructures grown on Si(111) [226], where the formation of a 3 - 7 nm thick disordered, ferromagnetic Fe-rich interstitial layer was reported.

7.3. Thermodynamic and elastic properties

The thermodynamic and elastic properties calculated from the PDOS obtained along Si$\langle\bar{1}10\rangle$ and Si$\langle11\bar{2}\rangle$ for S1 and along Si$\langle\bar{1}10\rangle$ and Si$\langle001\rangle$ for S2 - S4 are given in Table 7.3. The mean force constants F agree within the uncertainty for both directions for all samples and no systematic trend is observed. The mean square displacement $\langle x^2\rangle$ values also agree within the uncertainty for both directions, whereby the values obtained for S2 - S4 are larger along Si$\langle001\rangle$ compared to Si$\langle\bar{1}10\rangle$ and slightly increased compared to the bulk-like film of S1. The vibrational entropy S_V and the lattice heat capacity C_V do not show any systematic trend.

The value of the coefficient α obtained for S1 - S4 from $g(E) = \alpha E^2$ in the range 5 - 12 meV is also given in Table 7.3, together with the corresponding sound velocity v_S. The theoretical v_S values, obtained for bulk β-$FeSi_2$ from the slopes of the three acoustic branches in the dispersion relations, amount to $v_S = 5350\,m/s$ for sound waves propagating along the a - axis, $v_S = 5915\,m/s$ for sound waves propagating along the b - axis, and $v_S = 5832\,m/s$ for sound waves propagating along the c - axis of the β-$FeSi_2$ unit cell. The reduction of the experimental v_S values compared to the theoretical values originates from deceleration of sound waves by scattering at defects in the real crystals. Furthermore, the average v_S is slightly reduced in the nanorods of S2 - S4 compared to the bulk-like film of S1. However, due to the polycrystalline character of the film, which implies the presence of grain boundaries, and the relatively large dimensions of the nanorods the reduction is quite small, compared e.g. to the α-$FeSi_2$ nanowires discussed in Chapter 6.

7.4. Conclusions

Within this study, two types of β-$FeSi_2$ nanostructures were investigated. A β-$FeSi_2$ film was grown on Si(111) by solid phase epitaxy as a bulk-like reference sample.

Table 7.3: Fe-partial mean force constant F, mean square displacement $\langle x^2 \rangle$, vibrational entropy S_V, and lattice heat capacity C_V, calculated from the experimental PDOS of S1 - S4 obtained along the indicated directions. The coefficient α derived from the low-energy part of the PDOS [$g(E) = \alpha E^2$] and the sound velocity v_S are also given.

	F (N/m)	$\langle x^2 \rangle$ (10^{-2}Å^2)	S_V $(k_B/at.)$	C_V $(k_B/at.)$	α $(10^{-5} meV^{-3})$	v_S (m/s)
S1 $\langle \bar{1}10 \rangle$	268(5)	0.88(2)	2.57(2)	2.58(2)	2.44(3)	5135(66)
S1 $\langle 11\bar{2} \rangle$	269(5)	0.87(2)	2.54(2)	2.57(2)	2.45(3)	5132(51)
S2 $\langle \bar{1}10 \rangle$	272(5)	0.88(2)	2.52(2)	2.57(2)	2.54(4)	5069(88)
S2 $\langle 001 \rangle$	272(5)	0.89(2)	2.54(2)	2.57(2)	2.57(3)	5051(56)
S3 $\langle \bar{1}10 \rangle$	265(5)	0.89(2)	2.55(2)	2.58(2)	2.69(7)	4973(129)
S3 $\langle 001 \rangle$	272(5)	0.90(2)	2.55(2)	2.57(2)	2.62(8)	5017(155)
S4 $\langle \bar{1}10 \rangle$	270(5)	0.88(2)	2.54(2)	2.57(2)	2.43(6)	5143(127)
S4 $\langle 001 \rangle$	261(5)	0.91(2)	2.59(2)	2.58(2)	2.60(5)	5032(96)

RHEED and XRD measurements showed that the film is polycrystalline. By AFM the thickness of the intermittent film could be determined as 16.2 nm, which is very close to the theoretically expected film thickness of 16.4 nm. Furthermore, $FeSi_2$ nanorods were grown on Si(110) via transformation of α-$FeSi_2$ nanowires by prolonged annealing at 750 °C. An AFM study showed that after 2 h still residuals of high-aspect-ratio nanowires are observed at the chosen annealing temperature, whereas the transformation process is complete after annealing for 3 h. The nanorods exhibit width/length ratios of about 1/3 and their formation is accompanied by the emergence of trenches on one side of the nanorods. By a comparative Fe K-edge EXAFS study the crystal structure of the nanorods was determined to be β-$FeSi_2$. The epitaxial relation between the Si(110) surface and the β-$FeSi_2$ unit cell of the nanorods was determined by consideration of previous reports on the epitaxial relation between β-$FeSi_2$ and Si(111).

The Fe-partial PDOS of the film and the nanorods was obtained along two orthogonal directions by NIS experiments. The PDOS of the film exhibits an excellent agreement with the *ab initio* calculated PDOS of bulk β-$FeSi_2$. The observed vibrational isotropy is explained by the polycrystallinity of the film. Furthermore, the Fe-partial PDOS of the nanorods was obtained along and across their orientation. In addition to the main features of bulk β-$FeSi_2$, the emergence of a low-energy vibrational mode is observed. The intensity of this mode in the PDOS is increasing with increasing annealing time. Its origin could not unambiguously be determined, but the formation of an interstitial layer of an Fe-rich phase is a probable explanation for the observed behavior. Due to the relatively low surface/interface-to-volume ratio, the thermoelastic properties of the nanorods do not show significant deviations from the bulk-like film.

8. Summary and conclusions

This work presents a comprehensive study of the correlation between structure and size of iron-silicide nanostructures and their lattice dynamics and thermodynamic and elastic properties. Single-crystalline nanostructures of Fe_3Si, α-$FeSi_2$, and β-$FeSi_2$ were grown via molecular-beam epitaxy and analyzed with complementary structural characterization methods. The Fe-partial phonon density of states (PDOS) of the nanostructures was obtained by nuclear inelastic scattering experiments. Comparison with first-principles calculations, which were performed by a collaboration partner, and bulk reference samples revealed distinct vibrational anomalies upon reduction of the crystal size to the nanometer scale. As a general trend, the increase of the interface/surface-to-volume ratio results in a larger influence of interface- and surface-specific vibrational modes on the overall PDOS. Moreover, the higher concentration of defects at interfaces and surfaces leads to an enhanced scattering of phonons and a reduction of their lifetime, which manifests itself in a broadening of the PDOS features. The determination of the thermodynamic and elastic properties showed a softening of the lattice upon reduction of the crystal dimensions, which is evidenced by an increase of the mean square displacement and a reduction of the velocity of sound.

The Fe_3Si/GaAs heterostructure offered the possibility to specifically investigate the effect of the broken translational symmetry at interfaces on the lattice dynamics. For that purpose, epitaxial and strain-free Fe_3Si films were grown on the GaAs(001) surface and comprehensively characterized. The determination of the Fe-partial PDOS revealed an up to twofold enhancement of low-energy states and a strong phonon damping in the thinnest layers compared to a bulk-like film. By modeling of the experimental results with *ab initio* calculations, the observed low-energy enhancement of the PDOS could fully be explained by interface-specific vibrational states, while the damping was attributed to phonon scattering at crystallographic defects. Furthermore, the thermodynamic and elastic properties showed a significant softening of the Fe_3Si crystal in the thinnest layers compared to the bulk-like film, which is inter alia evidenced by a 36 % increase of the mean square displacement. This combined experimental and theoretical study constitutes the first experimental observation of the theoretically predicted interface-specific PDOS in epitaxial, strain-free interfaces.

The challenges connected to the determination of the lattice dynamics of the high-temperature phase α-$FeSi_2$ were tackled by the growth of metastable nanostructures on the Si(111) surface. Despite the strong vibrational anisotropy in the tetragonal α-$FeSi_2$ unit cell predicted by *ab initio* calculations, the Fe-partial PDOS obtained along orthogonal directions showed an isotropic vibrational behavior. This was explained by the epitaxial relation between the α-$FeSi_2$ unit cell and the Si(111) surface and the coexistence of three different domain orientations. The pronounced

damping of PDOS features observed upon reduction of the average structure height below 10 nm was modeled by convolution of the *ab initio* PDOS with the damped harmonic oscillator function and explained by the higher interface-to-volume ratio of the smaller nanostructures. Furthermore, the modeling revealed an anomalously strong damping of low-energy acoustic phonons in nanostructures with average heights below 10 nm. The results constitute the first determination of the lattice dynamics and corresponding thermodynamic and elastic properties of α-$FeSi_2$. The observed anomalously strong damping of acoustic phonons in the tetragonal α-$FeSi_2$ is expected to generally occur in nanostructures of single-crystalline materials with non-cubic unit cells.

Further insight on the influence of the macroscopic shape and surrounding of nanostructures on the lattice dynamics was gained by the investigation of endotaxial, i.e. partially embedded, single-crystalline α-$FeSi_2$ nanowires grown on the Si(110) surface. A combined experimental and theoretical EXAFS study demonstrated that the nanowires exhibited the metastable, surface-stabilized α-$FeSi_2$ crystal structure and thereby resolved the controversy about the crystal phase of $FeSi_2$ nanowires on Si(110). The Fe-partial PDOS along and across the nanowires revealed a vibrational anisotropy, which originates from the specific orientation of the tetragonal α-$FeSi_2$ unit cell on the Si(110) surface. Furthermore, a pronounced broadening of the PDOS features is observed upon reduction of the average nanowire width from 24 nm to 3 nm. Modeling of the experimental data with first-principles calculations demonstrated that the damping can be attributed to phonon scattering at the nanowire/substrate interface, which is particularly strong in the smallest nanowires characterized with the highest interface-to-volume ratio. A slightly stronger damping of lattice vibrations across the nanowires was explained by the smaller size of the α-$FeSi_2$ crystal along this direction. In general, the effect of the size reduction on the lattice dynamics is less pronounced compared to the two-dimensional nanostructures grown on Si(111), which can be attributed to the endotaxial nature of the nanowires and the lower interface/surface-to-volume ratio. The results presented for the lattice dynamics and thermoelastic properties of $FeSi_2$ nanowires are expected to be generally valid for the technologically important class of endotaxial silicide nanowires.

The lattice dynamics of β-$FeSi_2$ was investigated in a polycrystalline, bulk-like film and uniaxially aligned nanorods. While the Fe-partial PDOS of the film was very well reproduced by the *ab initio* calculated PDOS of bulk β-$FeSi_2$, the emergence of a novel, low-energy vibrational mode was observed in case of the nanorods. This new vibrational mode was attributed to the formation of an interstitial Fe-rich layer between the Si(110) surface and the β-$FeSi_2$ nanorods.

The novel vibrational phenomena disclosed in the framework of this thesis are not restricted to the chosen Fe-Si material system. In particular, the interface-specific PDOS in strain-free heterostructures and the anomalously strong damping of acoustic phonons in nanostructures of non-cubic crystals are expected to be general properties of the respective crystallographic systems. These findings offer an approach for the specific manipulation of the lattice dynamics and constitute an important step forward in the design of nanostructures with tailored vibrational properties.

Bibliography

1. M. A. Stroscio, M. Dutta, *Phonons in nanostructures* (Cambridge University Press, 2001).
2. E. Pop, S. Sinha, K. E. Goodson, *Proceedings of the IEEE* **94**, 1587 (2006).
3. A. L. Moore, L. Shi, *Materials Today* **17**, 163 (2014).
4. M. M. Waldrop, *Nature News* **530**, 144 (2016).
5. M. Dresselhaus, G. Chen, M. Tang, R. Yang, H. Lee, D. Wang, Z. Ren, J.-P. Fleurial, P. Gogna, *Advanced Materials* **19**, 1043 (2007).
6. B. Poudel, Q. Hao, Y. Ma, Y. Lan, A. Minnich, B. Yu, X. Yan, D. Wang, A. Muto, D. Vashaee, X. Chen, J. Liu, M. S. Dresselhaus, G. Chen, Z. Ren, *Science* **320**, 634 (2008).
7. H. Alam, S. Ramakrishna, *Nano Energy* **2**, 190 (2013).
8. M. B. Zanjani, J. R. Lukes, *The Journal of Physical Chemistry C* **119**, 16889 (2015).
9. M. Maldovan, *Nature Materials* **14**, 667 (2015).
10. J. Hone, B. Batlogg, Z. Benes, A. T. Johnson, J. E. Fischer, *Science* **289**, 1730 (2000).
11. S. P. Hepplestone, G. P. Srivastava, *Nanotechnology* **17**, 3288 (2006).
12. E. P. Pokatilov, D. L. Nika, A. A. Balandin, *Journal of Applied Physics* **95**, 5626 (2004).
13. V. A. Fonoberov, A. A. Balandin, *Nano Letters* **6**, 2442 (2006).
14. D. L. Nika, E. P. Pokatilov, A. A. Balandin, *Applied Physics Letters* **93**, 173111 (2008).
15. S. Uno, J. Hattori, K. Nakazato, N. Mori, *Journal of Computational Electronics* **10**, 104 (2011).
16. D. Bozyigit, N. Yazdani, M. Yarema, O. Yarema, W. M. M. Lin, S. Volk, K. Vuttivorakulchai, M. Luisier, F. Juranyi, V. Wood, *Nature* **531**, 618 (2016).
17. I. A. Shojaei, S. Linser, G. Jnawali, N. Wickramasuriya, H. E. Jackson, L. M. Smith, F. Kargar, A. A. Balandin, X. Yuan, P. Caroff, H. H. Tan, C. Jagadish, *Nano Letters* **19**, 5062 (2019).
18. R. Pradip, P. Piekarz, D. G. Merkel, J. Kalt, O. Waller, A. I. Chumakov, R. Rüffer, A. M. Oleś, K. Parlinski, T. Baumbach, S. Stankov, *Nanoscale* **11**, 10968 (2019).
19. A. A. Balandin, *Journal of Nanoscience and Nanotechnology* **5**, 1015 (2005).

20. A. A. Balandin, D. L. Nika, *Materials Today* **15**, 266 (2012).
21. M. Maldovan, *Nature* **503**, 209 (2013).
22. B. Li, L. Wang, G. Casati, *Physical Review Letters* **93**, 184301 (2004).
23. C. W. Chang, D. Okawa, A. Majumdar, A. Zettl, *Science* **314**, 1121 (2006).
24. L. Wang, B. Li, *Physical Review Letters* **99**, 177208 (2007).
25. M. J. Martínez-Pérez, A. Fornieri, F. Giazotto, *Nature Nanotechnology* **10**, 303 (2015).
26. S. Volz, J. Ordonez-Miranda, A. Shchepetov, M. Prunnila, J. Ahopelto, T. Pezeril, G. Vaudel, V. Gusev, P. Ruello, E. M. Weig, M. Schubert, M. Hettich, M. Grossman, T. Dekorsy, F. Alzina, B. Graczykowski, E. Chavez-Angel, J. Sebastian Reparaz, M. R. Wagner, C. M. Sotomayor-Torres, S. Xiong, S. Neogi, D. Donadio, *The European Physical Journal B* **89**, 15 (2016).
27. M. Seto, Y. Yoda, S. Kikuta, X. Zhang, M. Ando, *Physical Review Letters* **74**, 3828 (1995).
28. W. Sturhahn, T. S. Toellner, E. E. Alp, X. Zhang, M. Ando, Y. Yoda, S. Kikuta, M. Seto, C. W. Kimball, B. Dabrowski, *Physical Review Letters* **74**, 3832 (1995).
29. S. Stankov, R. Röhlsberger, T. Slezak, M. Sladecek, B. Sepiol, G. Vogl, A. I. Chumakov, R. Rüffer, N. Spiridis, J. Lazewski, K. Parlinski, J. Korecki, *Physical Review Letters* **99**, 185501 (2007).
30. R. Rüffer, A. I. Chumakov, *Hyperfine Interactions* **128**, 255 (2000).
31. T. Slezak, J. Lazewski, S. Stankov, K. Parlinski, R. Reitinger, M. Rennhofer, R. Rüffer, B. Sepiol, M. Slezak, N. Spiridis, M. Zajac, A. I. Chumakov, J. Korecki, *Physical Review Letters* **99**, 066103 (2007).
32. S. P. Murarka, *Intermetallics* **3**, 173 (1995).
33. L. J. Chen, *JOM* **57**, 24 (2005).
34. Y.-C. Lin, Y. Chen, Y. Huang, *Nanoscale* **4**, 1412 (2012).
35. A. Nozariasbmarz, A. Agarwal, Z. A. Coutant, M. J. Hall, J. Liu, R. Liu, A. Malhotra, P. Norouzzadeh, M. C. Öztürk, V. P. Ramesh, Y. Sargolzaeiaval, F. Suarez, D. Vashaee, *Japanese Journal of Applied Physics* **56**, 05DA04 (2017).
36. S. Liang, R. Islam, D. J. Smith, P. A. Bennett, J. R. O'Brien, B. Taylor, *Applied Physics Letters* **88**, 113111 (2006).
37. M. Hilse, J. Herfort, B. Jenichen, A. Trampert, M. Hanke, P. Schaaf, L. Geelhaar, H. Riechert, *Nano Letters* **13**, 6203 (2013).
38. J. Herfort, H.-P. Schönherr, A. Kawaharazuka, M. Ramsteiner, K. H. Ploog, *Journal of Crystal Growth* **278**, 666 (2005).
39. M. Kawano, K. Santo, M. Ikawa, S. Yamada, T. Kanashima, K. Hamaya, *Applied Physics Letters* **109**, 022406 (2016).
40. Y. Ando, K. Hamaya, K. Kasahara, Y. Kishi, K. Ueda, K. Sawano, T. Sadoh, M. Miyao, *Applied Physics Letters* **94**, 182105 (2009).

41. D. Leong, M. Harry, K. Reeson, K. Homewood, *Nature* **387**, 686 (1997).

42. M. C. Bost, J. E. Mahan, *Journal of Applied Physics* **58**, 2696 (1985).

43. Q. Wan, T. H. Wang, C. L. Lin, *Applied Physics Letters* **82**, 3224 (2003).

44. Y. Okuhara, D. Yokoe, T. Kato, S. Suda, M. Takata, K. Noritake, A. Sato, *Solar Energy Materials and Solar Cells* **161**, 240 (2017).

45. Y. Okuhara, T. Kuroyama, D. Yokoe, T. Kato, M. Takata, T. Tsutsui, K. Noritake, *Solar Energy Materials and Solar Cells* **174**, 351 (2018).

46. M. I. Fedorov, G. N. Isachenko, *Japanese Journal of Applied Physics* **54**, 07JA05 (2015).

47. A. T. Burkov, *Physica Status Solidi (a)* **215**, 1800105 (2018).

48. B.-X. Xu, Y. Zhang, H.-S. Zhu, D.-Z. Shen, J.-L. Wu, *Materials Letters* **59**, 833 (2005).

49. G. P. Srivastava, *The physics of phonons* (Hilger, Bristol, 1990).

50. M. T. Dove, *Collection SFN* **12**, 123 (2011).

51. Y. Chen, D. Yang, *Mössbauer effect in lattice dynamics: experimental techniques and applications* (John Wiley & Sons, 2007).

52. C. de Tomas, A. Cantarero, A. F. Lopeandia, F. X. Alvarez, *Proceedings of the Royal Society A: Mathematical, Physical and Engineering Sciences* **470**, 20140371 (2014).

53. B. Fultz, *Progress in Materials Science* **55**, 247 (2010).

54. A. Einstein, *Annalen der Physik* **327**, 180 (1907).

55. P. Debye, *Annalen der Physik* **344**, 789 (1912).

56. V. Sharma, *Mössbauer spectroscopy: Applications in chemistry, biology, and nanotechnology* (Wiley, Hoboken, New Jersey, 2013).

57. B. Fåk, B. Dorner, *Institute Laue Langevin, Technical Report No. 92FA008S* (1992).

58. B. Fåk, B. Dorner, *Physica B: Condensed Matter* **234**, 1107 (1997).

59. R. Röhlsberger, W. Sturhahn, T. S. Toellner, K. W. Quast, P. Hession, M. Hu, J. Sutter, E. E. Alp, *Journal of Applied Physics* **86**, 584 (1999).

60. K. Houben, S. Couet, M. Trekels, E. Menendez, T. Peissker, J. W. Seo, M. Y. Hu, J. Y. Zhao, E. E. Alp, S. Roelants, B. Partoens, M. V. Milosevic, F. M. Peeters, D. Bessas, S. A. Brown, A. Vantomme, K. Temst, M. J. Van Bael, *Physical Review B* **95**, 155413 (2017).

61. M. A. Herman, H. Sitter, *Molecular Beam Epitaxy - Fundamentals and Current Status* (Springer Berlin/Heidelberg, 1996).

62. B. Krause, S. Darma, M. Kaufholz, H.-H. Gräfe, S. Ulrich, M. Mantilla, R. Weigel, S. Rembold, T. Baumbach, *Journal of Synchrotron Radiation* **19**, 216 (2012).

63. A. Ichimiya, P. I. Cohen, *Reflection high-energy electron diffraction* (Cambridge University Press, 2004).
64. P. Dobson, J. Neave, B. Joyce, *Surface Science* **119**, L339 (1982).
65. P. Delescluse, A. Masson, *Surface Science* **100**, 423 (1980).
66. G. Wang, S. K. Lok, S. K. Chan, C. Wang, G. K. L. Wong, I. K. Sou, *Nanotechnology* **20**, 215607 (2009).
67. P. Eaton, P. West, *Atomic Force Micrsocopy* (Oxford University Press, New York, 2010).
68. G. Bunker, *Introduction to XAFS: a practical guide to x-ray absorption fine structure spectroscopy* (Cambridge University Press, New York, 2010).
69. S. Pascarelli, *Fundamentals of X-ray Absorption Fine Structure*, Lecture, HERCULES School: Neutrons and Synchrotron Radiation for Science, 2017.
70. B. Ravel, M. Newville, *Journal of Synchrotron Radiation* **12**, 537 (2005).
71. R. Mößbauer, *Zeitschrift für Physik* **151**, 124 (1958).
72. R. Mößbauer, *Naturwissenschaften* **45**, 538 (1958).
73. R. Mößbauer, W. Wiedemann, *Zeitschrift für Physik* **159**, 33 (1960).
74. W. J. Lamb, *Physical Review* **55**, 190 (1939).
75. D. Barb, *Grundlagen und Anwendungen der Mössbauerspektroskopie* (Editura Academiei Bucuresti and Akademie-Verlag Berlin, 1980).
76. W. M. Visscher, *Annals of Physics* **9**, 194 (1960).
77. H. Weiss, H. Langhoff, *Physics Letters A* **69**, 448 (1979).
78. S. L. Ruby, *Le Journal de Physique Colloques* **35**, 209 (1974).
79. R. L. Cohen, G. L. Miller, K. W. West, *Physical Review Letters* **41**, 381 (1978).
80. E. Gerdau, R. Rüffer, H. Winkler, W. Tolksdorf, C. Klages, J. Hannon, *Physical Review Letters* **54**, 835 (1985).
81. W. Sturhahn, *Journal of Physics: Condensed Matter* **16**, S497 (2004).
82. E. E. Alp, W. Sturhahn, T. Toellner, *Hyperfine Interactions* **135**, 295 (2001).
83. M. Y. Hu, W. Sturhahn, T. S. Toellner, P. M. Hession, J. P. Sutter, E. E. Alp, *Nuclear Instruments and Methods in Physics Research Section A: Accelerators, Spectrometers, Detectors and Associated Equipment* **428**, 551 (1999).
84. V. G. Kohn, A. I. Chumakov, R. Rüffer, *Physical Review B* **58**, 8437 (1998).
85. K. S. Singwi, A. Sjölander, *Physical Review* **120**, 1093 (1960).
86. L. Van Hove, *Physical Review* **95**, 249 (1954).
87. A. I. Chumakov, R. Rüffer, A. Q. R. Baron, H. Grünsteudel, H. F. Grünsteudel, V. G. Kohn, *Physical Review B* **56**, 10758 (1997).
88. H. J. Lipkin, *Annals of Physics* **9**, 332 (1960).
89. H. J. Lipkin, *Physical Review B* **52**, 10073 (1995).

90. M. Y. Hu, W. Sturhahn, T. S. Toellner, P. D. Mannheim, D. E. Brown, J. Zhao, E. E. Alp, *Physical Review B* **67**, 094304 (2003).
91. R. Rüffer, A. I. Chumakov, *Hyperfine Interactions* **97-98**, 589 (1996).
92. H.-C. Wille, H. Franz, R. Röhlsberger, W. A. Caliebe, F.-U. Dill, *Journal of Physics: Conference Series* **217**, 012008 (2010).
93. G. Mülhaupt, R. Rüffer, *Hyperfine Interactions* **123**, 13 (1999).
94. T. S. Toellner, *Hyperfine Interactions* **125**, 3 (2000).
95. A. Q. R. Baron, *Hyperfine Interactions* **125**, 29 (2000).
96. S. Baroni, S. de Gironcoli, A. Dal Corso, P. Giannozzi, *Reviews of Modern Physics* **73**, 515 (2001).
97. P. Pavone, *Journal of Physics: Condensed Matter* **13**, 7593 (2001).
98. P. Hohenberg, W. Kohn, *Phys. Rev.* **136**, B864 (1964).
99. W. Kohn, L. J. Sham, *Phys. Rev.* **140**, A1133 (1965).
100. K. Parlinski, Z. Q. Li, Y. Kawazoe, *Physical Review Letters* **78**, 4063 (1997).
101. J. Kalt, M. Sternik, B. Krause, I. Sergueev, M. Mikolasek, D. Bessas, O. Sikora, T. Vitova, J. Göttlicher, R. Steininger, P. T. Jochym, A. Ptok, O. Leupold, H.-C. Wille, A. I. Chumakov, P. Piekarz, K. Parlinski, T. Baumbach, S. Stankov, *Physical Review B* **101**, 165406 (2020).
102. G. Kresse, J. Furthmüller, *Physical Review B* **54**, 11169 (1996).
103. G. Kresse, J. Furthmüller, *Computational Materials Science* **6**, 15 (1996).
104. J. P. Perdew, K. Burke, M. Ernzerhof, *Physical Review Letters* **77**, 3865 (1996).
105. J. P. Perdew, K. Burke, M. Ernzerhof, *Physical Review Letters* **78**, 1396 (1997).
106. P. E. Blöchl, *Physical Review B* **50**, 17953 (1994).
107. G. Kresse, D. Joubert, *Physical Review B* **59**, 1758 (1999).
108. K. Parlinski, *Software PHONON, version 6.15, Cracow, Poland*, 2015.
109. O. Kubaschewski, *Iron - Binary Phase Diagrams* (Springer Berlin/Heidelberg and Verlag Stahleisen GmbH, Düsseldorf, 1982).
110. U. Starke, W. Weiss, M. Kutschera, R. Bandorf, K. Heinz, *Journal of Applied Physics* **91**, 6154 (2002).
111. A. Ionescu, C. A. F. Vaz, T. Trypiniotis, C. M. Gürtler, H. García-Miquel, J. A. C. Bland, M. E. Vickers, R. M. Dalgliesh, S. Langridge, Y. Bugoslavsky, Y. Miyoshi, L. F. Cohen, K. R. A. Ziebeck, *Physical Review B* **71**, 094401 (2005).
112. M. Hansen, *Constitution of Binary Alloys* (McGraw-Hill, New York, 1958).
113. J. Herfort, H.-P. Schönherr, K. H. Ploog, *Applied Physics Letters* **83**, 3912 (2003).

114. W. Hines, A. Menotti, J. Budnick, T. Burch, T. Litrenta, V. Niculescu, K. Raj, *Physical Review B* **13**, 4060 (1976).

115. I. Berbezier, J. Chevrier, J. Derrien, *Surface Science* **315**, 27 (1994).

116. N. E. Christensen, *Physical Review B* **42**, 7148 (1990).

117. T. Hunt, K. Reeson, K. Homewood, S. Teon, R. Gwilliam, B. Sealy, *Nuclear Instruments and Methods in Physics Research Section B: Beam Interactions with Materials and Atoms* **84**, 168 (1994).

118. C. Giannini, S. Lagomarsino, F. Scarinci, P. Castrucci, *Physical Review B* **45**, 8822 (1992).

119. K. Takarabe, R. Teranishi, J. Oinuma, Y. Mori, T. Suemasu, S. Chichibu, F. Hasegawa, *Physical Review B* **65**, 165215 (2002).

120. I. Sandalov, N. Zamkova, V. Zhandun, I. Tarasov, S. Varnakov, I. Yakovlev, L. Solovyov, S. Ovchinnikov, *Physical Review B* **92**, 205129 (2015).

121. J. Chevrier, P. Stocker, V. L. Thanh, J. M. Gay, J. Derrien, *Europhysics Letters* **22**, 449 (1993).

122. J. K. Tripathi, M. Garbrecht, W. D. Kaplan, G. Markovich, I. Goldfarb, *Nanotechnology* **23**, 495603 (2012).

123. J. K. Tripathi, G. Markovich, I. Goldfarb, *Applied Physics Letters* **102**, 251604 (2013).

124. G. Cao, D. J. Singh, X.-G. Zhang, G. Samolyuk, L. Qiao, C. Parish, K. Jin, Y. Zhang, H. Guo, S. Tang, W. Wang, J. Yi, C. Cantoni, W. Siemons, E. A. Payzant, M. Biegalski, T. Z. Ward, D. Mandrus, G. M. Stocks, Z. Gai, *Physical Review Letters* **114**, 147202 (2015).

125. V. S. Zhandun, N. G. Zamkova, S. G. Ovchinnikov, I. S. Sandalov, *Physical Review B* **95**, 054429 (2017).

126. T. Sadoh, M. Kumano, R. Kizuka, K. Ueda, A. Kenjo, M. Miyao, *Applied Physics Letters* **89**, 182511 (2006).

127. M. Miyao, K. Ueda, Y. I. Ando, M. Kumano, T. Sadoh, K. Narumi, Y. Maeda, *Thin Solid Films* **517**, 181 (2008).

128. S. Yamada, K. Tanikawa, M. Miyao, K. Hamaya, *Crystal Growth and Design* **12**, 4703 (2012).

129. K. Hamaya, T. Murakami, S. Yamada, K. Mibu, M. Miyao, *Physical Review B* **83**, 144411 (2011).

130. K. Hamaya, K. Ueda, Y. Kishi, Y. Ando, T. Sadoh, M. Miyao, *Applied Physics Letters* **93**, 132117 (2008).

131. M. Kawano, S. Yamada, K. Tanikawa, K. Sawano, M. Miyao, K. Hamaya, *Applied Physics Letters* **102**, 121908 (2013).

132. Y. C. Liu, Y. W. Chen, S. C. Tseng, M. T. Chang, S. C. Lo, Y. H. Lin, C. K. Cheng, H. Y. Hung, C. H. Hsu, J. Kwo, M. Hong, *Applied Physics Letters* **107**, 122402 (2015).

133. V. M. Kaganer, B. Jenichen, R. Shayduk, W. Braun, *Physical Review B* **77**, 125325 (2008).

134. B. Jenichen, Z. Cheng, M. Hanke, J. Herfort, A. Trampert, *Semiconductor Science and Technology* **34**, 124002 (2019).

135. J. Herfort, H.-P. Schönherr, K.-J. Friedland, K. H. Ploog, *Journal of Vacuum Science & Technology B: Microelectronics and Nanometer Structures Processing, Measurement, and Phenomena* **22**, 2073 (2004).

136. B. Jenichen, V. M. Kaganer, J. Herfort, D. K. Satapathy, H.-P. Schönherr, W. Braun, K. H. Ploog, *Physical Review B* **72**, 075329 (2005).

137. B. Jenichen, V. Kaganer, W. Braun, J. Herfort, R. Shayduk, K. H. Ploog, *Thin Solid Films* **515**, 5611 (2007).

138. B. Jenichen, V. Kaganer, W. Braun, R. Shayduk, B. Tinkham, J. Herfort, *Journal of Materials Science: Materials in Electronics* **19**, 199 (2008).

139. J. Herfort, B. Jenichen, V. Kaganer, A. Trampert, H.-P. Schönherr, K. H. Ploog, *Physica E: Low-dimensional Systems and Nanostructures* **32**, 371 (2006).

140. B. Jenichen, J. Herfort, U. Jahn, A. Trampert, H. Riechert, *Thin Solid Films* **556**, 120 (2014).

141. J. Hafner, D. Spisak, *Physical Review B* **75**, 195411 (2007).

142. V. M. Kaganer, B. Jenichen, R. Shayduk, W. Braun, H. Riechert, *Physical Review Letters* **102**, 016103 (2009).

143. S. Tobler, P. Bennett, *Journal of Applied Physics* **118**, 125305 (2015).

144. D. Das, J. C. Mahato, B. Bisi, B. Satpati, B. N. Dev, *Applied Physics Letters* **105**, 191606 (2014).

145. J. Alvarez, J. J. Hinarejos, E. G. Michel, R. Miranda, *Surface Science* **287-288**, 490 (1993).

146. K. Kataoka, K. Hattori, Y. Miyatake, H. Daimon, *Physical Review B* **74**, 155406 (2006).

147. H. von Känel, N. Onda, H. Sirringhaus, E. Müller-Gubler, S. Goncalves-Conto, C. Schwarz, *Applied Surface Science* **70-71**, 559 (1993).

148. H. Nakano, K. Maetani, K. Hattori, H. Daimon, *Surface Science* **601**, 5088 (2007).

149. J. Chrost, J. J. Hinarejos, P. Segovia, E. G. Michel, R. Miranda, *Surface Science* **371**, 297 (1997).

150. J. Wu, S. Shimizu, *Journal of Applied Physics* **80**, 559 (1996).

151. S. Liang, R. Islam, D. J. Smith, P. Bennett, *Journal of Crystal Growth* **295**, 166 (2006).

152. S. Y. Chen, H. C. Chen, L. J. Chen, *Applied Physics Letters* **88**, 193114 (2006).

153. Z. He, D. J. Smith, P. A. Bennett, *Physical Review Letters* **93**, 256102 (2004).

154. P. A. Bennett, Z. He, D. J. Smith, F. M. Ross, *Thin Solid Films* **519**, 8434 (2011).

155. Z.-Q. Zou, X. Li, X.-Y. Liu, K.-J. Shi, X.-Q. Guo, *Applied Surface Science* **399**, 200 (2017).

156. S. Dennler, J. Hafner, *Physical Review B* **73**, 174303 (2006).

157. Y. F. Liang, S. Shang, J. Wang, Y. Wang, F. Ye, J. Lin, G. L. Chen, Z. K. Liu, *Intermetallics* **19**, 1374 (2011).

158. O. G. Randl, G. Vogl, W. Petry, B. Hennion, B. Sepiol, K. Nembach, *Journal of Physics: Condensed Matter* **7**, 5983 (1995).

159. J.-I. Tani, M. Takahashi, H. Kido, *Physica B: Condensed Matter* **405**, 2200 (2010).

160. M. Walterfang, W. Keune, E. Schuster, A. T. Zayak, P. Entel, W. Sturhahn, T. S. Toellner, E. E. Alp, P. T. Jochym, K. Parlinski, *Physical Review B* **71**, 035309 (2005).

161. H. Kroemer, *Reviews of Modern Physics* **73**, 783 (2001).

162. S. Gaucher, B. Jenichen, J. Kalt, U. Jahn, A. Trampert, J. Herfort, *Applied Physics Letters* **110**, 102103 (2017).

163. M. Björck, G. Andersson, *Journal of Applied Crystallography* **40**, 1174 (2007).

164. B. Roldan Cuenya, L. K. Ono, J. R. Croy, K. Paredis, A. Kara, H. Heinrich, J. Zhao, E. E. Alp, A. T. DelaRiva, A. Datye, E. A. Stach, W. Keune, *Physical Review B* **86**, 165406 (2012).

165. A. Kara, T. S. Rahman, *Physical Review Letters.* **81**, 1453 (1998).

166. J. Acker, K. Bohmhammel, G. van den Berg, J. van Miltenburg, C. Kloc, *The Journal of Chemical Thermodynamics* **31**, 1523 (1999).

167. H. von Känel, K. A. Mäder, E. Müller, N. Onda, H. Sirringhaus, *Physical Review B* **45**, 13807 (1992).

168. J. Chevrier, V. Le Thanh, S. Nitsche, J. Derrien, *Applied Surface Science* **56-58**, 438 (1992).

169. N. Onda, H. Sirringhaus, S. Goncalves-Conto, C. Schwarz, S. Zehnder, H. von Känel, *Applied Surface Science* **73**, 124 (1993).

170. A. L. V. de Parga, J. de la Figuera, C. Ocal, R. Miranda, *Ultramicroscopy* **42-44**, 845 (1992).

171. N. Jedrecy, A. Waldhauer, M. Sauvage-Simkin, R. Pinchaux, Y. Zheng, *Physical Review B* **49**, 4725 (1994).

172. M. Sauvage-Simkin, N. Jedrecy, A. Waldhauer, R. Pinchaux, *Physica B: Condensed Matter* **198**, 48 (1994).

173. P. Stocker, J.-M. Gay, J.-Y. Natoli, *Physica B: Condensed Matter* **198**, 240 (1994).

174. F. Sirotti, M. DeSantis, X. Jin, G. Rossi, *Physical Review B* **49**, 11134 (1994).

175. N. Minami, D. Makino, T. Matsumura, C. Egawa, T. Sato, K. Ota, S. Ino, *Surface Science* **514**, 211 (2002).

176. P. Bennett, S. Parikh, M. Lee, D. G. Cahill, *Surface Science* **312**, 377 (1994).

177. S. Ibrahimkutty, A. Seiler, T. Prüßmann, T. Vitova, R. Pradip, O. Bauder, P. Wochner, A. Plech, T. Baumbach, S. Stankov, *Journal of Synchrotron Radiation* **22**, 91 (2015).

178. S. Couet, M. Sternik, B. Laenens, A. Siegel, K. Parlinski, N. Planckaert, F. Gröstlinger, A. I. Chumakov, R. Rüffer, B. Sepiol, K. Temst, A. Vantomme, *Physical Review B* **82**, 094109 (2010).

179. B. Klobes, M. Herlitschke, K. Z. Rushchanskii, H.-C. Wille, T. T. A. Lummen, P. H. M. van Loosdrecht, A. A. Nugroho, R. P. Hermann, *Physical Review B* **92**, 014304 (2015).

180. Y. Ohira, T. Tanji, M. Yoshimura, K. Ueda, *Japanese Journal of Applied Physics* **47**, 6138 (2008).

181. S. Liang, B. A. Ashcroft, *Journal of Materials Research* **25**, 213 (2010).

182. T. Kim, J. P. Bird, *Applied Physics Letters* **97**, 263111 (2010).

183. P. Zu-Lin, S. Liang, *Chinese Physics Letters* **25**, 4113 (2008).

184. S. Y. Chen, H. C. Chen, L. J. Chen, *Applied Physics Letters* **88**, 193114 (2006).

185. S. Hara, M. Yoshimura, K. Ueda, *Japanese Journal of Applied Physics* **48**, 08JB10 (2009).

186. O. M. Mukdadi, S. K. Datta, M. L. Dunn, *Journal of Applied Physics* **97**, 074313 (2005).

187. P. B. Allen, *Nano Letters* **7**, 11 (2007).

188. S. Mizuno, N. Nishiguchi, *Journal of Physics: Condensed Matter* **21**, 195303 (2009).

189. D. Martínez-Gutiérrez, V. R. Velasco, *Surface Science* **605**, 24 (2011).

190. L. Saviot, *Physical Review B* **97**, 155420 (2018).

191. J. Zou, A. Balandin, *Journal of Applied Physics* **89**, 2932 (2001).

192. B. A. Glavin, *Physical Review Letters* **86**, 4318 (2001).

193. B. Qiu, L. Sun, X. Ruan, *Physical Review B* **83**, 035312 (2011).

194. H. Karamitaheri, N. Neophytou, H. Kosina, *Journal of Applied Physics* **115**, 024302 (2014).

195. Y. Zhou, X. Zhang, M. Hu, *Nano Letters* **17**, 1269 (2017).

196. Z. Rashid, L. Zhu, W. Li, *Physical Review B* **97**, 075441 (2018).

197. B. Li, D. Yu, S.-L. Zhang, *Physical Review B* **59**, 1645 (1999).

198. R. Wang, G. Zhou, Y. Liu, S. Pan, H. Zhang, D. Yu, Z. Zhang, *Physical Review B* **61**, 16827 (2000).

199. S. Piscanec, M. Cantoro, A. C. Ferrari, J. A. Zapien, Y. Lifshitz, S. T. Lee, S. Hofmann, J. Robertson, *Physical Review B* **68**, 241312 (2003).

200. K. W. Adu, H. R. Gutiérrez, U. J. Kim, G. U. Sumanasekera, P. C. Eklund, *Nano Letters* **5**, 409 (2005).

201. A. Patsha, S. Dhara, *Nano Letters* **18**, 7181 (2018).

202. S. O. Mariager, D. Khakhulin, H. T. Lemke, K. S. Kjær, L. Guerin, L. Nuccio, C. B. Sørensen, M. M. Nielsen, R. Feidenhans'l, *Nano Letters* **10**, 2461 (2010).

203. F. Kargar, B. Debnath, J.-P. Kakko, A. Säynätjoki, H. Lipsanen, D. L. Nika, R. K. Lake, A. A. Balandin, *Nature Communications* **7**, 13400 (2016).

204. M. De Luca, C. Fasolato, M. A. Verheijen, Y. Ren, M. Y. Swinkels, S. Kölling, E. P. A. M. Bakkers, R. Rurali, X. Cartoixà, I. Zardo, *Nano Letters* **19**, 4702 (2019).

205. D. Bessas, W. Töllner, Z. Aabdin, N. Peranio, I. Sergueev, H.-C. Wille, O. Eibl, K. Nielsch, R. P. Hermann, *Nanoscale* **5**, 10629 (2013).

206. D. P. Lozano, S. Couet, C. Petermann, G. Hamoir, J. K. Jochum, T. Picot, E. Menendez, K. Houben, V. Joly, V. A. Antohe, M. Y. Hu, B. M. Leu, A. Alatas, A. H. Said, S. Roelants, B. Partoens, M. V. Milosevic, F. M. Peeters, L. Piraux, J. Van de Vondel, A. Vantomme, K. Temst, M. J. Van Bael, *Physical Review B* **99**, 064512 (2019).

207. Y. Yamamoto, *Surface Science* **313**, 155 (1994).

208. B. A. Joyce, J. H. Neave, P. J. Dobson, P. K. Larsen, *Physical Review B* **29**, 814 (1984).

209. T. Kawamura, M. Hasebe, P. J. Dobson, *Journal of the Physical Society of Japan* **54**, 3675 (1985).

210. E. Rakova, *Surface Science* **307-309**, 1172 (1994).

211. J. H. Won, K. Sato, M. Ishimaru, Y. Hirotsu, *Journal of Applied Physics* **100**, 014307 (2006).

212. J. Tersoff, R. M. Tromp, *Physical Review Letters* **70**, 2782 (1993).

213. R. Batabyal, S. Patra, A. Roy, B. Dev, *Applied Surface Science* **257**, 3248 (2011).

214. H. Lange, *Physica Status Solidi (b)* **201**, 3 (1997).

215. Y. Murakami, A. Kenjo, T. Sadoh, T. Yoshitake, M. Miyao, *Thin Solid Films* **461**, 68 (2004).

216. M. E. Toimil Molares, A. G. Balogh, T. W. Cornelius, R. Neumann, C. Trautmann, *Applied Physics Letters* **85**, 5337 (2004).

217. S. Karim, M. E. Toimil-Molares, W. Ensinger, A. G. Balogh, T. W. Cornelius, E. U. Khan, R. Neumann, *Journal of Physics D: Applied Physics* **40**, 3767 (2007).

218. H. Li, J. M. Biser, J. T. Perkins, S. Dutta, R. P. Vinci, H. M. Chan, *Journal of Applied Physics* **103**, 024315 (2008).

219. J. W. Strutt, L. Rayleigh, *Proceedings of the London Mathematical Society* **10**, 4 (1878).

220. F. Scarinci, S. Lagomarsino, C. Giannini, G. Savelli, P. Castrucci, A. Rodia, L. Scopa, *Applied Surface Science* **56-58**, 444 (1992).

221. D. Miquita, R. Paniago, W. Rodrigues, M. Moreira, H.-D. Pfannes, A. de Oliveira, *Thin Solid Films* **493**, 30 (2005).

222. A. N. Hattori, K. Hattori, H. Daimon, *Journal of Physics: Conference Series* **61**, 404 (2007).

223. S. Oyarzún, A. K. Nandy, F. Rortais, J.-C. Rojas-Sánchez, M.-T. Dau, P. Noël, P. Laczkowski, S. Pouget, H. Okuno, L. Vila, C. Vergnaud, C. Beigné, A. Marty, J.-P. Attané, S. Gambarelli, J.-M. George, H. Jaffrès, S. Blügel, M. Jamet, *Nature Communications* **7**, 13857 (2016).

224. W. Lianwei, S. Qinwo, C. Xiangdong, L. Xian, L. Chenglu, Z. Shichang, *Chinese Physics Letters* **12**, 301 (1995).

225. W. Raunau, H. Niehus, T. Schilling, G. Comsa, *Surface Science* **286**, 203 (1993).

226. A. N. Hattori, K. Hattori, K. Kodama, N. Hosoito, H. Daimon, *Applied Physics Letters* **91**, 201916 (2007).

List of Figures

2.1. Phonon dispersion relations and phonon density of states of silicon. . 7
2.2. Damped harmonic oscillator function plotted for different quality factors and convoluted *ab initio* phonon density of states. 9
2.3. UHV-Cluster at the UHV Analysis lab at the KIT. 10
2.4. UHV growth chambers. 11
2.5. RHEED geometry and patterns observed for different surface topographies. 13
2.6. Schematic AFM line profile measured with a sharp and a dull tip. . . 14
2.7. Schematic layout of a synchrotron based x-ray absorption fine structure spectroscopy station. 15
2.8. Exemplary x-ray absorption fine structure spectroscopy results. . . . 16
2.9. Simplified scheme of the deexcitation channels of the ^{57}Fe nuclear resonance at 14.413 keV. 19
2.10. Normalized probability of nuclear inelastic absorption and phonon density of states of α-$FeSi_2$. 20
2.11. Schematic layout of a nuclear resonant scattering beamline. 23

3.1. Schematic representation of the unit cells of the investigated iron silicides. 28
3.2. Transmission electron microscope images of endotaxial $FeSi_2$ nanowires. 30
3.3. *Ab initio* calculated phonon dispersion relations and phonon density of states of Fe_3Si, β-$FeSi_2$ and α-$FeSi_2$. 32

4.1. RHEED patterns measured along the GaAs/Fe_3Si [010] and [110] azimuth. 36
4.2. AFM images of the investigated samples. 37
4.3. X-ray diffraction and x-ray reflectivity results of S1 - S4. 38
4.4. High resolution TEM images of S1, S3, and S4. 40
4.5. Magnified high resolution TEM images of S3 and S4. 41
4.6. Fe-partial phonon density of states of S1 - S4, compared with the respective results for $g_{theo}(E)$. 42
4.7. Reduced PDOS of S1 - S4. 43
4.8. *Ab initio* calculated layer-specific Fe-, Si-, As-, and Ga-partial PDOS projected along and across the interface, compared with the corresponding spectra in bulk material. 45
4.9. Atomic configuration of the $Fe_3Si(001)$/GaAs(001) supercell used to calculate the interface lattice dynamics presented in Figure 4.8 46

5.1. Unit cell of α-$FeSi_2$ with the α-$FeSi_2(112)$ plane and parallel directions. 52

5.2. Epitaxial relation between α-$FeSi_2$ and the Si(111) surface. 53
5.3. RHEED patterns of the Si(111) substrate and the investigated samples. 54
5.4. AFM images of the investigated samples. 56
5.5. Width and height distribution of the investigated nanostructures. . . 57
5.6. XAFS, EXAFS, and EXAFS Fourier transform of S1 and S6. 58
5.7. Fe-partial phonon density of states of the investigated samples. 60
5.8. Fe-partial reduced PDOS of the investigated samples and normalized α values. 61
5.9. Comparison of the experimental PDOS with fit results. 64
5.10. Quality factors Q and Q_{xy}, Q_z as a function of the nanostructure height. 65

6.1. RHEED patterns obtained along different azimuths of the Si(110) surface. 73
6.2. RHEED patterns of the investigated samples. 74
6.3. XAFS, EXAFS, and EXAFS Fourier transform of S7, S2 and S6. . . . 75
6.4. Orientation of the α-$FeSi_2$ unit cell on the Si(110) surface. 77
6.5. AFM images of the investigated samples. 78
6.6. Illustration of the procedure used for determination of the nanowire dimensions. 79
6.7. Fe-partial phonon density of states of the investigated samples. 81
6.8. Quality factors Q_{xy} and $Q_{xy,z}$ plotted as a function of average nanowire width. 83
6.9. Fe-partial reduced PDOS of the investigated samples. 84

7.1. RHEED patterns of the investigated samples obtained before growth, after growth, and after annealing. 91
7.2. Wide range θ-2θ XRD scan of S1. 92
7.3. XAFS, EXAFS, and EXAFS Fourier transforms of S1, S3, and S4. . . 93
7.4. Orientation of the β-$FeSi_2$ unit cell on the Si(111) and Si(110) surfaces. 94
7.5. AFM images of the investigated samples. 95
7.6. Fe-partial phonon density of states of S1. 96
7.7. Fe-partial PDOS of S2, S3, and S4. 97

List of Tables

4.1. Thickness and R_{rms} values of the Fe_3Si and Ge layers of S1 - S4. . . . 37
4.2. Thermodynamic and elastic properties of the investigated samples. . . 48

5.1. Overview of the growth and experimental conditions of the investigated samples. 52
5.2. Interatomic distances, coordination numbers and mean square displacement obtained from modeling of the experimental EXAFS spectra and theoretical values for the expected $FeSi_2$ phases. 59
5.3. Thermodynamic and elastic properties of the investigated samples. . . 67

6.1. Overview of the growth and experimental conditions of the investigated samples. 72
6.2. Interatomic distances, coordination numbers and mean square displacement obtained from modeling of the experimental EXAFS spectra and theoretical values for the expected $FeSi_2$ phases. 76
6.3. Thermodynamic and elastic properties of the investigated samples. . . 85

7.1. Overview of the growth and experimental conditions of the investigated samples. 90
7.2. Overview of the structural properties of the investigated samples. . . 95
7.3. Thermodynamic and elastic properties of the investigated samples. . . 100

A. Publications

A.1. Publications related to the thesis

Lattice dynamics of endotaxial silicide nanowires
J. Kalt, M. Sternik, B. Krause, I. Sergueev, M. Mikolasek, D. Merkel, D. Bessas, O. Sikora, T. Vitova, J. Göttlicher, R. Steininger, P. T. Jochym, A. Ptok, O. Leupold, H.-C. Wille, A. I. Chumakov, P. Piekarz, K. Parlinski, T. Baumbach, and S. Stankov
Physical Review B 102, 195414 (2020)

Lattice dynamics and polarization-dependent phonon damping in α-phase $FeSi_2$ nanostructures
J. Kalt, M. Sternik, B. Krause, I. Sergueev, M. Mikolasek, D. Bessas, O. Sikora, T. Vitova, J. Göttlicher, R. Steininger, P. T. Jochym, A. Ptok, O. Leupold, H.-C. Wille, A. I. Chumakov, P. Piekarz, K. Parlinski, T. Baumbach and S. Stankov
Physical Review B 101, 165406 (2020)

Ab initio and nuclear inelastic scattering studies of Fe_3Si/GaAs heterostructures
O. Sikora, **J. Kalt**, M. Sternik, A. Ptok, P. T. Jochym, J. Łażewski, P. Piekarz, K. Parlinski, I. Sergueev, H.-C. Wille, J. Herfort, B. Jenichen, T. Baumbach, and S. Stankov
Physical Review B 99, 134303 (2019)

Lattice dynamics of epitaxial strain-free interfaces
J. Kalt, M. Sternik, I. Sergueev, J. Herfort, B. Jenichen, H.-C. Wille, O. Sikora, P. Piekarz, K. Parlinski, T. Baumbach and S. Stankov
Physical Review B Rapid Communications 98, 121409(R) (2018)

A.2. Other publications

Phonon confinement and spin-phonon coupling in tensile-strained thin EuO films
R. Pradip, P. Piekarz, D. G. Merkel, **J. Kalt**, O. Waller, A. I. Chumakov, R. Rüffer, A. M. Oleś, K. Parlinski, T. Baumbach and S. Stankov
Nanoscale 11 10968 (2019)

Growth of Fe_3Si/Ge/Fe_3Si trilayers on GaAs(001) using solid-phase epitaxy
S. Gaucher, B. Jenichen, **J. Kalt**, U. Jahn, A. Trampert and J. Herfort
Applied Physics Letters 110, 102103 (2017)

A.3. Conference contributions

- *Lattice dynamics of endotaxial silicide nanowires*
  Invited talk, German Mössbauer Workshop 2020, Jena
- *Lattice dynamics and polarization-dependent phonon damping in α-phase $FeSi_2$ nanostructures*
  Talk, 5th Workshop on ab initio Phonon Calculations 2019, Krakow, Poland
- *Lattice Dynamics of Epitaxial Strain-Free Interfaces*
  Poster, German Conference for Research with Synchrotron Radiation, Neutrons and Ion Beams at Large Facilities (SNI) 2018, Munich
- *Confined lattice dynamics in ultrathin $Ge/Fe_3Si/GaAs$ heterostructures*
  Talk, DPG Spring Meeting, Berlin
- *Lattice dynamics in ultrathin $Ge/Fe_3Si/GaAs$ heterostructures*
  Talk, International Conference on the Application of the Mössbauer Effect (ICAME) 2017, St. Petersburg, Russia
- *Confined lattice dynamics in ultrathin $Ge/Fe_3Si/GaAs$ heterostructures*
  Talk, DyProSo XXXVI Conference 2017, Krakow, Poland

B. Python script

The script fits a experimental PDOS curve using the least squares fitting routine `scipy.optimize.curve_fit` with two *ab initio* calculated components. Both *ab initio* calculated components are convoluted with a damped harmonic oscillator function. The relative ratio between the two components 'A' and the quality factor 'Q' are fit parameters.

```
import matplotlib.pyplot as plt
import numpy as np
from scipy import integrate
from scipy.optimize import curve_fit

pi = 3.14159265359
e=2.71828182846
x_dho  = np.arange(2,80,0.1)

#################################################################
# First, some basic functions are defined

# funcion for spectrum normation
def norm_int(x,y):
    n = integrate.trapz(y, x, 0.01)
    y = [l/n for l in y]
    return y

# here the damped harmonic oscillator function function is defined
# as a array of size len(x_dos) times len(x_dho)

def dho(x_dho,x_dos,Q):
 """ damped harmonic oscillator """
 dho  = []
 count = 0
 arr =np.zeros((len(x_dos),len(x_dho)))
 for i in x_dos:
    for k in x_dho:
        d = 1/(pi*Q*i)*1/((i/k-k/i)**2+1/Q**2)
        dho.append(d)
    arr[count,:]=dho
```

```
    dho  = []
    count  = count+1
 return arr


def sum_col(arr,l):
 """sum of columns of dho"""
 sum = []
 for k in range(0,len(l)):
     s = arr[:,k].sum()
     sum.append(s)
 return sum


#################################################################
# function for convolution of a curve with the damped harmonic oscillator
# function defined above

def conv_arr(x_dho,y,Q):
    """convoltion"""
    x_dos  = x_dho
    y_dho = dho_test(x_dho,x_dos,Q)
    j=1
    conv_arr_test=np.zeros((len(x_dos),len(x_dho)),dtype=object)
    for j in range(0,len(x_dho)):
        c  = np.convolve(y[j],y_dho[j,:],mode='full')
        conv_arr_test[j,:]=c
    summe  = []
    for k in range(0,len(x_dho)):
        s  = np.sum(conv_arr_test[:,k])
        summe.append(s)
    conv  = summe
    #normalization
    conv  = norm_int(x_dho,conv)
    return conv


# In the following the special case of experimental curve fitted with
# two ab initio components is treated

def subspec_2comp_Afix(abinitio_1,abinitio_2,A,Q):
    conv_1  = conv_arr_test(x_dho,abinitio_1,Q)
    conv_2  = conv_arr_test(x_dho,abinitio_2,Q)
    dos  = [conv_1[i]*A + conv_2[i]*(1-A) for i in range(len(x_dho))]
    sub_1  = [i*A for i in conv_1]
    sub_2  = [i*(1-A) for i in conv_2]
```

```
    n  = integrate.trapz(dos, x_dho, 0.01)
    dos  = [l/n for l in dos]
    sub_1  = [l/n for l in sub_1]
    sub_2  = [l/n for l in sub_2]
    return dos, sub_1, sub_2

def fit_func_2comp_Afix(x,y1,y2,A,Q):
 """ convolution of damped harmonic oscillator (array) with y DOS (list) """
 conv1  = conv_arr_test(x,abinitio_1,Q)
 conv2  = conv_arr_test(x,abinitio_2,Q)
 dos  = [conv1[i]*A + conv2[i]*(1-A) for i in range(len(x))]
 dos  = norm_int(x,dos)
 return dos

def curve_fit_2comp_Afix(y_exp, abinitio_1,abinitio_2,A):
    def fit_2comp(x_dho,Q):
        return fit_func_2comp_Afix(x_dho,abinitio_1,abinitio_2,A,Q)
    popt, pcov = curve_fit(fit_2comp, x_dho, y_exp,p0=(5),bounds=((1),(100)))
    sigma = np.sqrt(np.diag(pcov))
    result  =list(popt)
    y_sim,y_sub1,y_sub2 =subspec_2comp_Afix(abinitio_1,abinitio_2,A,result[0])

    return  y_sim,y_sub1,y_sub2, result

fit_sample = curve_fit_2comp_Afix(y_sample1,alpha_FeSi2_xy,alpha_FeSi2_z,0.69)
```

Acknowledgement

I want to thank Prof. Tilo Baumbach for his support and the opportunity to work at the IPS.

I would also like to thank Prof. Matthieu Le Tacon for his efforts to read and evaluate my PhD thesis.

I am very grateful to Dr. Svetoslav Stankov who gave me the opportunity of working as a PHD student in this exciting field of research. His immense enthusiasm, experience, and knowledge were essential for this project. He showed me what is achievable with the right the amount of determination, persistence, and patience. We experienced great adventures during our beamtimes and travels. I also thank him for his efforts to improve this thesis.

I also want to thank Dr. habil. Przemysław Piekarz, Dr. Małgorzata Sternik, and Dr. Olga Sikora, for performing the ab initio calculations. The theoretical input was crucial to reach the conclusions presented in the thesis.

Many thanks to Aleksandr Chumakov, Dimitrios Bessas, and Mirko Mikolasek from ID18 as well as Ilya Sergueev, Hans-Christian Wille, and Olaf Leuphold from P01. Your tireless efforts during the beamtimes were impressive and it was always a pleasure to work with you.

I also want to thank Jörg Göttlicher and Ralph Steininger for their support at the SUL-X beamline and Tonya Vitova for her valuable contribution for understanding the EXAFS results.

I would like to thank Bärbel Krause for her efforts in keeping the UHV laboratory and its instrumentation running and sharing her vast experience in surface characterization. Annette Weißhardt I thank for preparing the AFM tips and her general contribution to the UHV laboratory.

In general, I'd like to thank my former and current colleagues at the IPS, the scattering group, and the Nanodynamics group. Many thanks go to Julian Jakob and Anton Plech for their corrections on this thesis.

Abschließend möchte ich allen Menschen danken, die mich ein Stück weit auf diesem Weg begleitet haben, im Besonderen meiner Familie.